



LUND UNIVERSITY

Optical and laser diagnostics

The versatility of Imaging

Matamis, Alexios

2021

[Link to publication](#)

Citation for published version (APA):

Matamis, A. (2021). *Optical and laser diagnostics: The versatility of Imaging*. Department of Physics, Lund University.

Total number of authors:

1

General rights

Unless other specific re-use rights are stated the following general rights apply:

Copyright and moral rights for the publications made accessible in the public portal are retained by the authors and/or other copyright owners and it is a condition of accessing publications that users recognise and abide by the legal requirements associated with these rights.

- Users may download and print one copy of any publication from the public portal for the purpose of private study or research.
- You may not further distribute the material or use it for any profit-making activity or commercial gain
- You may freely distribute the URL identifying the publication in the public portal

Read more about Creative commons licenses: <https://creativecommons.org/licenses/>

Take down policy

If you believe that this document breaches copyright please contact us providing details, and we will remove access to the work immediately and investigate your claim.

LUND UNIVERSITY

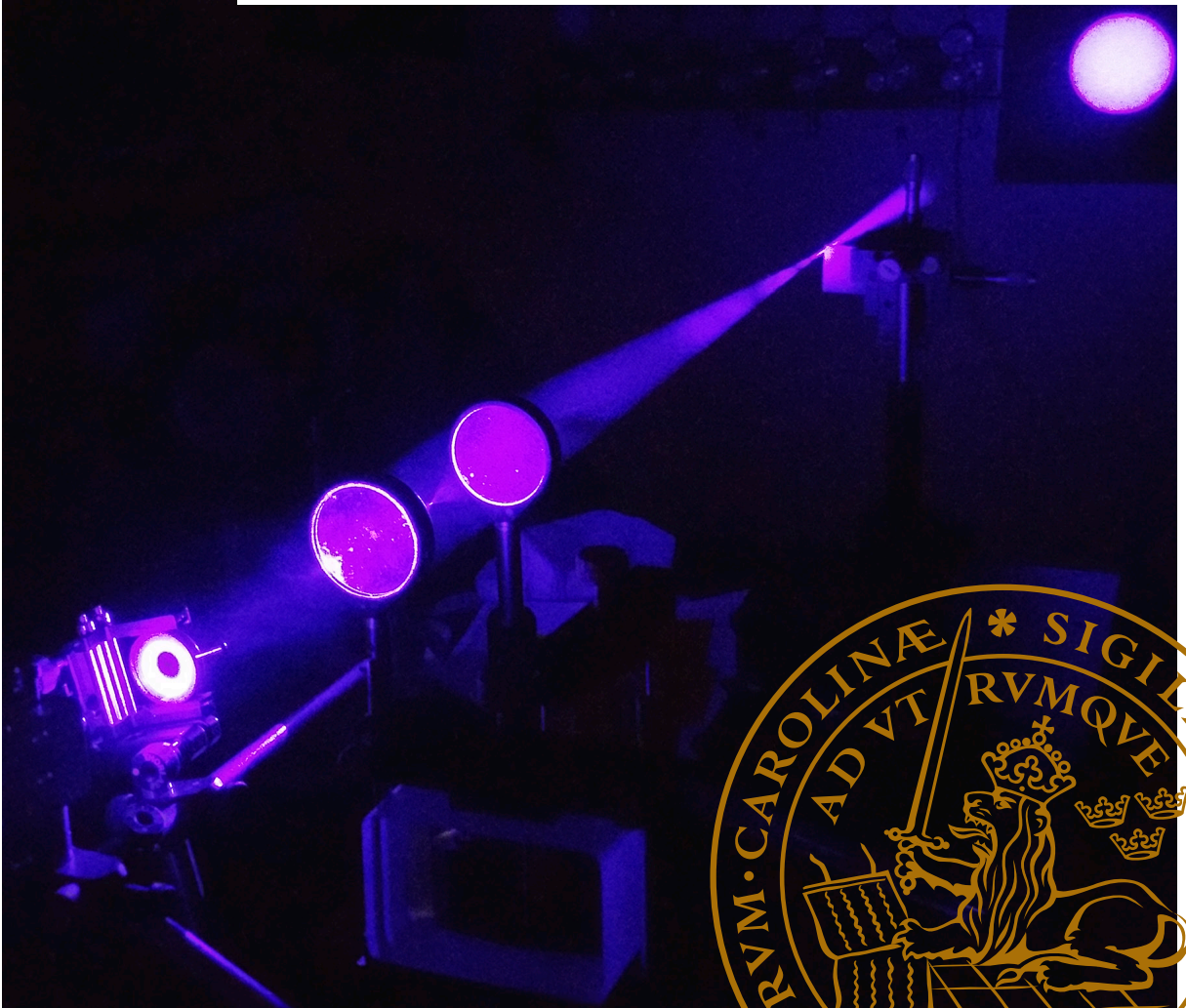
PO Box 117
221 00 Lund
+46 46-222 00 00

Optical and laser diagnostics

The versatility of Imaging

ALEXIOS MATAMIS

DEPARTMENT OF PHYSICS | FACULTY OF ENGINEERING | LUND UNIVERSITY





Faculty of Engineering
Department of Physics
Division of Combustion Physics

Lund Reports on Combustion Physics: LRCP-232
ISRN LUTFD2/TFCP-232-SE
ISBN 978-91-7895-879-5
ISSN 1102-8718



Optical and laser diagnostics

The versatility of Imaging

Alexios Matamis



LUND
UNIVERSITY

DOCTORAL DISSERTATION

by due permission of the Faculty of Engineering LTH, Lund University, Sweden.

To be defended at Rydbergsalen, Fysicum, Professorgatan 1.

May 28, 2021 at 09:00.

Faculty opponent

José Vicente Pastor, CMT-Motores Térmicos,
Universitat Politècnica de València, Spain

Organization: LUND UNIVERSITY Division of Combustion Physics, Department of Physics, P.O. Box 118, SE-211 00, Lund, Sweden		Document name: DOCTORAL DISSERTATION
		Date of issue: 2021-05-28
Author: Alexios Matamis		Sponsoring organization:
Title and subtitle: Optical and Laser diagnostics: The versatility of Imaging		
<p>Abstract</p> <p>Optical and laser diagnostics is a field where optical techniques are developed that offer remote, non-intrusive measurements in order to characterise a system. Imaging is a big part of this field and the versatility it offers makes it a great tool in the hands of researchers and in practical applications. In this thesis, multiple applications of imaging are presented, together with possible data processing routines that are used to obtain qualitative and quantitative information. Intuitive ways of presenting big datasets along with trends and variations in them are shown, for both, time-resolved and single-shot measurements. Efforts to enhance the efficiency of internal combustion engines are discussed and a study on the interaction of spray jets and prevailing combustion in light-duty diesel engines is shown. A thorough optical investigation of methanol combustion in compression ignition engines is presented, along with a characterisation of the injection process and fuel distribution for methanol inside a heavy-duty optical engine. The potential of methanol as a renewable fuel and energy carrier is discussed in a wider perspective, together with demonstrating the benefits of such a propulsion system. In addition, a study of exhaled respiratory particles is presented, in an attempt to characterise the potential for transmission of diseases through the respiratory tract. This consisted of an evaluation of everyday tasks such as talking and singing, which is not commonly found in the literature as most studies are focused on sneezing and coughing. Finally, a novel approach on Background Oriented Schlieren, known as Laser Speckle-based BOS, is presented together with some preliminary results. There is great potential for this technique to be used in combustion engine diagnostics, as it requires minimal optical access to create the pattern and the sensitivity of the setup relies less on the distance of the subject to the background pattern.</p>		
Key words: Methanol, Combustion, Diesel, Schlieren, Spray, Imaging, Pilot-injection, High-speed imaging		
Classification system and/or index terms (if any)		
Supplementary bibliographical information		Language: English
ISSN and key title: 1102-8718 ISRN LUTFD2/TFCP-232-SE		ISBN: 978-91-7895-879-5 (print) 978-91-7895-880-1 (pdf)
Recipient's notes	Number of pages 202	Price
	Security classification	

I, the undersigned, being the copyright owner of the abstract of the above-mentioned dissertation, hereby grant to all reference sources permission to publish and disseminate the abstract of the above-mentioned dissertation.

Signature



Date 2021-04-20

Optical and laser diagnostics

The versatility of Imaging

Alexios Matamis



LUND
UNIVERSITY

Coverphoto by Alexios Matamis

Copyright pp 1-110 Alexios Matamis

Paper 1 © 2020 The Authors, Published by Am. Assoc. for Aerosol Research

Paper 2 © 2020 The Authors, Published by Elsevier Inc.

Paper 3 © 2020 SAE International

Paper 4 © 2019 SAE International

Paper 5 © 2019 SAE International

Paper 6 © 2017 SAE International

Faculty of Engineering

Department of Physics

Lund University

ISBN (print) 978-91-7895-879-5

ISBN (pdf) 978-91-7895-880-1

ISRN LUTFD2/TFCP-232-SE

ISSN 1102-8718

Printed in Sweden by Media-Tryck, Lund University, Lund 2021



Media-Tryck is a Nordic Swan Ecolabel
certified provider of printed material.
Read more about our environmental
work at www.mediatryck.lu.se

MADE IN SWEDEN 

*In loving memory of my grandfather,
who couldn't afford to study*

Table of Contents

Table of Contents.....	7
Abstract	9
Popular Science Summary.....	11
List of papers.....	13
Related work	14
1. Introduction	15
2. Optical Techniques.....	25
2.1. Natural Luminosity.....	25
2.2. Elastic light scattering	27
2.3. Laser-Induced Fluorescence	28
2.4. Shadowgraphy and Schlieren photography	29
3. Equipment.....	35
3.1. Signal Filtering	35
3.2. Detectors.....	37
3.3. Light sources	39
3.4. Optical engines	41
4. Image processing and analysis	43
4.1. Image processing	43
4.1.1. Noise and Background	43
4.1.2. Image Undistortion.....	46
4.1.3. Image Segmentation	49
4.1.4. Image Registration.....	50
4.2. Image analysis	53
4.2.1. Individual or single-shot images.....	53
4.2.2. Image sequences	58
5. Results	61
5.1. Exhaled respiratory particles	61
5.2. Optical study of methanol.....	66

5.2.1. Combustion Characterisation	68
5.2.2. Injection Characterisation.....	75
5.3. Diesel multiple-injection characterization.....	81
5.4. Laser speckle Background Oriented Schlieren.....	89
6. Conclusions and Outlook.....	93
Acknowledgements	95
References	99
Summary of papers	107
Appended Articles	111

Abstract

Optical and laser diagnostics is a field where optical techniques are developed that offer remote, non-intrusive measurements in order to characterise a system. Imaging is a big part of this field and the versatility it offers makes it a great tool in the hands of researchers and in practical applications. In this thesis, multiple applications of imaging are presented, together with possible data processing routines that are used to obtain qualitative and quantitative information. Intuitive ways of presenting big datasets along with trends and variations in them are shown, for both, time-resolved and single-shot measurements. Efforts to enhance the efficiency of internal combustion engines are discussed and a study on the interaction of spray jets and prevailing combustion in light-duty diesel engines is shown. A thorough optical investigation of methanol combustion in compression ignition engines is presented, along with a characterisation of the injection process and fuel distribution for methanol inside a heavy-duty optical engine. The potential of methanol as a renewable fuel and energy carrier is discussed in a wider perspective, together with demonstrating the benefits of such a propulsion system. In addition, a study of exhaled respiratory particles is presented, in an attempt to characterise the potential for transmission of diseases through the respiratory tract. This consisted of an evaluation of everyday tasks such as talking and singing, which is not commonly found in the literature as most studies are focused on sneezing and coughing. Finally, a novel approach on Background Oriented Schlieren, known as Laser Speckle-based BOS, is presented together with some preliminary results. There is great potential for this technique to be used in combustion engine diagnostics, as it requires minimal optical access to create the pattern and the sensitivity of the setup relies less on the distance of the subject to the background pattern.

Popular Science Summary

How do you show a video on paper? How do you describe a beautifully complicated physical phenomenon with words? Surely the reader is going to miss out on the intricate details of these dynamic systems that we analyse. These are some thoughts that pass through any researcher's head, as they are worried if they are doing their own data justice. People commonly say that "a picture is worth 1000 words". While this may stand true when trying to relay a beautiful view or an experience to other people, in science the picture is often not that clear. This inherent difficulty in relaying information in science can be likened by artwork, where maybe only few people can understand the message that the artist is trying to convey.

In this thesis, multiple applications of optical and laser-based diagnostics in practical applications are presented. The goal is to capture what effects are taking place and characterise the system by analysing this compressed representation of the real world that we obtain with imaging. Predominantly, the work relies on high-speed imaging, where the temporal variation of the effect we study is resolved with the use of a high-speed camera. Considering temporal variations are not easy to convey in written form, we present several different ways where this information can be communicated intuitively.

A lot of research began on studying disease spread after the onset of Covid-19. Since spreading happens via airborne particles, this is an area where our diagnostic tools were able to make a difference. We optically investigated the number and speed of exhaled respiratory droplets in a variety of real-world conditions, such as talking at different volumes to represent everyday life of people interactions, along with singing at different tonality and volume to see if choir singing could pose an activity with increased risk of disease transmission. Previous efforts had mostly focused on coughing and sneezing and were only capturing maximum distance and the average path of particles. Our high-speed analysis resolved the particle number, path, and speed, in real time, in a large area around the mouth. The representation of the data obtained from this study is striking, as it is direct, intuitive and succeeds in conveying the number of particles emitted and what is the path that they follow.

The greatest part of the thesis, however, covers material that ultimately focuses on increasing the efficiency of internal combustion engines to reduce both, global and local emissions, in an attempt to combat global warming and air quality. In a holistic approach, replacing fossil with renewable fuels can dramatically reduce the carbon

footprint of the transportation and energy sector which are the main contributors to CO₂ emissions and this shift can happen far quicker than any other alternative. Electric vehicles are a promising solution for personal transportation since they are great at reducing local emissions in congested cities. However, assessing both propulsion systems on a life-cycle basis including the carbon intensity of battery production and that of oil production, the difference in CO₂ emissions is not as impressive as the zero-emission claim and they only cover a fraction of the greater picture of a sustainable energy system.

Meanwhile, methanol is an extremely versatile biofuel that could serve many existing energy platforms. It can be used as a fuel itself or as a building block to create other fuels for existing combustion concepts. Additionally, methanol can be used as an electricity carrier in fuel cell applications, or as an electro-fuel to store renewably sourced electricity, with high energy density and without the carbon intensity or cycle life limitation of batteries. Our findings show that methanol combusts significantly different compared to other fuels, particularly in diesel-like combustion. Mixing with air is also much faster and the oxygen content in methanol's molecule inhibits particulate formation. Thus, low injection pressures can be used, reducing engine losses and strain on the injection system with no adverse effects. As such, in an energy scheme based on methanol, a highly efficient and low emission propulsion system can be obtained with diesel-like combustion of bio-derived methanol.

List of papers

- I. Alsved, M., **Matamis, A.**, Bohlin, R., Richter, M., Bengtsson, P. E., Fraenkel, C. J., Medstrand, P., & Löndahl, J. (2020). *Exhaled respiratory particles during singing and talking*. *Aerosol Science and Technology*, 54(11), 1245-1248.
- II. **Matamis, A.**, Lonn, S., Luise, L., Vaglieco, B. M., Tuner, M., Andersson, O., Alden, M., & Richter, M. (2020). *Optical characterization of methanol compression-ignition combustion in a heavy-duty engine*. Proceedings of the Combustion Institute.
- III. **Matamis, A.**, Lonn, S., Tuner, M., Andersson, O., & Richter, M. (2020). *Optical Characterization of Methanol Sprays and Mixture Formation in a Compression-Ignition Heavy-Duty Engine*. In *SAE Powertrains, Fuels & Lubricants Meeting (2020 ed.)*. [2020-01-2109] (SAE Technical Papers). Society of Automotive Engineers.
- IV. Denny, M., **Matamis, A.**, Wang, Z., Persson, H., Tunestal, P., Richter, M., & Andersson, A. I. (2019). *Optical Investigation on the Combustion Process Differences between Double-Pilot and Closely-Coupled Triple-Pilot Injection Strategies in a LD Diesel Engine*. In *International Powertrains, Fuels & Lubricants Meeting (Vol. 2019-January)*. (SAE Technical Papers).
- V. Denny, M., **Matamis, A.**, Persson, H., Richter, M., & Andersson, Ö. (2019). *Interaction between Fuel Jets and Prevailing Combustion During Closely-Coupled Injections in an Optical LD Diesel Engine*. In *SAE Technical Paper: Automotive [2019-01-0551]* (SAE Technical Papers). Society of Automotive Engineers.
- VI. Wang, Z., Lönn, S., **Matamis, A.**, Andersson, O., Tuner, M., Alden, M., & Richter, M. (2017). *Transition from HCCI to PPC: Investigation of Fuel Distribution by Planar Laser Induced Fluorescence (PLIF)*. *SAE International Journal of Engines*, 10(4).

Related work

- I. Hult, J., **Matamis, A.**, Baudoin, E., Mayer, S., & Richter, M. (2020). *Optical Characterization of the Combustion Process inside a Large-Bore Dual-Fuel Two-Stroke Marine Engine by Using Multiple High-Speed Cameras*. In WCX SAE World Congress Experience (Vol. 2020-April). [2020-01-0788] (SAE Technical Papers). Society of Automotive Engineers.
- II. Hult, J., **Matamis, A.**, Baudoin, E., Mayer, S., & Richter, M. (2020). *Spatiotemporal flame mapping in a large-bore marine diesel engine using multiple high-speed cameras*. International Journal of Engine Research, 21(4), 622-631.
- III. Binder, C., **Matamis, A.**, Richter, M., & Norling, D. (2019). *Study on heat losses during flame impingement in a diesel engine using phosphor thermometry surface temperature measurements*. In Technical Paper - WCX SAE World Congress Experience (Vol. 2019). [2019-01-0556] (SAE Technical Papers). Society of Automotive Engineers.
- IV. Binder, C., **Matamis, A.**, Richter, M., & Norling, D. (2019). *Comparison of heat losses at the impingement point and in between two impingement points in a diesel engine using phosphor thermometry*. In 2019 JSAE/SAE Powertrains, Fuels and Lubricants (December ed.). [2019-01-2185] (SAE Technical Papers). Society of Automotive Engineers.
- V. Lundgren, M., **Matamis, A.**, Wang, Z., Garcia Valladolid, P., Richter, M., Andersson, O., & Andersson, A. (2018). *Lift-Off Lengths in an Optical Heavy-Duty Engine Operated at High Load with Low and High-Octane Number Fuels*. SAE Technical Papers, 2018-April.
- VI. Lundgren, M. O., Wang, Z., **Matamis, A.**, Andersson, O., Richter, M., Tuner, M., Alden, M., & Andersson, A. (2017). *Effects of Post-Injections Strategies on UHC and CO at Gasoline PPC Conditions in a Heavy-Duty Optical Engine*. SAE Technical Papers, 2017(March), [2017-01-0753].
- VII. Lönn, S., **Matamis, A.**, Tuner, M., Richter, M., & Andersson, O. (2017). *Optical Study of Fuel Spray Penetration and Initial Combustion Location under PPC Conditions*. SAE Technical Papers, 2017-March (March).

1. Introduction

Nature is full of beautifully complicated processes that researchers try to explain and analyse in a variety of forms in order to provide knowledge and understanding that can be used for the greater good. Some with immediate outcomes, like earthquake and weather forecasting that can save lives by providing advanced warnings for upcoming catastrophic events. Others provide the seed to a whole new field of science that we as a human species never knew we needed, such as semiconductors or commercial and personal transportation vehicles.

Optical and laser diagnostics is a field where optical and spectroscopic properties of materials or media are used to measure certain parameters and analyse a system. Specifically, this could be measuring temperature at a certain location, detecting the presence of a molecule or a number of particles or determining the composition of a gas mixture. More broadly, remote measurement techniques are developed in order to study how a system is interacting with the environment, in a way that the measurement itself is insignificantly intrusive to the system. The measurements can span in various dimensions in space, such as at a point which we consider zero-dimensional (0D), along a line (1D), planar (2D), or in three-dimensional (3D) space. In some applications, the measurement is path-integrated, meaning that the measurement incorporates part or the whole volume containing the system under investigation, potentially in a multiple pass configuration, thus the measurement is not limited to a particular dimension but rather it expresses the property we want to measure with a representative unit. Additionally, since most systems in nature are dynamic and change over time, it might be necessary for the technique to have the ability to temporally resolve these changes in a meaningful way, depending on the rate of change of the system.

Looking through the history of mankind, the realization comes that the only way to communicate information to other people irrespective of time, is two dimensional. From the paintings of prehistoric man in caves, to texts and books of recent history, the famous “scripta manent” springs to mind. The best way humanity has developed to communicate through time has historically been two dimensional. The truth is, that while we perceive the world in four dimensions, three spatial dimensions and one temporal, a single picture summarises only a two-dimensional snapshot of it. Understandably, a lot of real-world information is missing from this two-dimensional representation. One single image can mean a million words to one observer and absolutely nothing to another. Even adding the temporal dimension,

when observing a transient phenomenon in a succession of images does not guarantee a successful communication of the process to all viewers. Simply capturing a physical process is not enough to convey a message and a universal understanding, but rather requires in depth analysis and explanation. Despite the aforementioned attributes, two-dimensional imaging is still the most information-dense representation of the real-world that we can obtain from experimental equipment. By combining multiple cameras and recording image sequences, we can possibly obtain a true to life representation of the system, however these techniques are yet highly computationally expensive and fundamentally, they still rely on data from two-dimensional imaging.

Historically, it has been hard to do time-resolved studies since the experimental equipment simply did not exist. High-speed light sources and high-speed cameras, capable of capturing rapid phenomena have become easily accessible only in the last 30 years approximately. Thus, the usual process has been to collect multiple samples at a certain timing of the studied effect in order to have a statistically significant sample size, and then proceed to sweep across the whole duration of the effect and repeat the sampling process. Obviously, while this method can still provide a good understanding of the studied phenomenon, it cannot resolve the process in real-time and thus a lot of the information is lost. Thus, we can tell what happened, but not necessarily how it happened and for this exact reason, great effort has been put in the past in developing setups and equipment that can resolve the temporal domain. Among the very first time-resolved studies on diesel sprays was conducted by Harold E. Miller and Edward G. Beardsley [1] in 1926, where 15 transparent capacitors were charged to 30.000Volt and were discharged sequentially, providing short light pulses for the 15 images. This system provided an estimated exposure of 5 μ sec in each frame, which was adequate to freeze the motion of the spray process. In contrast to modern days, the detector repetition rate was not the limiting factor since they used a film-camera, and the film speed could easily be increased. In the modern era, new light sources have been developed that provide exceptional temporal resolution and high-speed cameras that can record at very high frame rates. Thus, the ultra-fast and transient phenomena we want to analyse can be resolved, however, the bottle neck still exists on how to present and communicate this kind of data. In the past, conferences and presentations were the only way to reproduce videos, but nowadays video content is very easy to watch and share, and even academic journals support the upload of complimentary material to articles. Nevertheless, simply sharing a video of an effect does not include any analysis and some form of compressed representation is necessary to improve the understanding of the effect. In this thesis, we will discuss some ways of analysing and compressing the information from image sequences of dynamic phenomena that manage to relay and quantify the processes taking place rather intuitively. This is done with modal decomposition techniques where the prominent and recurring motions are characterised and can be summarised in pictures.

The majority of the work presented in this thesis revolves around resolving and analysing combustion phenomena inside Internal Combustion Engines (ICE's). By convention, internal combustion engine design is a balancing act between efficiency and emissions, particularly in compression-ignition engines. This balance is further perplexed due to the trade-off between local emissions and global emissions. A reduction in CO₂ emissions will cause an increase in other pollutants like CO, unburned hydrocarbon, particulate matter and nitrogen oxides (NO_x) depending on the combustion strategy used. On the contrary, an attempt to reduce local pollutants will cause loss in efficiency and result in increased CO₂ emissions. Partially Premixed Combustion (PPC) is considered a promising combustion concept when it comes to balancing efficiency and emissions, and its analysis and evaluation comprised a big part of the work here. The key parameter to achieve these characteristics is the fuel injection timing, where too early injection will lead to high amount of CO and unburned hydrocarbons due to fuel being delivered in crevice volumes inside the combustion chamber and thus poor combustion efficiency. Conversely, late injection timing results in little air and fuel mixing and as such, combustion will take place at fuel rich conditions resulting in formation of particulate matter commonly referred to as soot, depending however on the properties of the fuel. This can be seen in the right part of Figure 1.1 for diesel fuel, which is a figure of equivalence ratio vs temperature. The red line represents the adiabatic flame temperature of diesel fuel and it is observed that when diesel combusts at high equivalence ratios, meaning fuel-rich conditions, soot will be formed. Meanwhile, close to stoichiometric conditions, NO_x will be formed instead and very little soot, however, combustion efficiency increases in late injections as the fuel distribution inside the cylinder is contained well. The result is a narrow window for the PPC regime to operate in and balance both, efficiency and emissions. Nevertheless, the properties of the fuel used are pivotal to the outcome of this balancing act and can allow for some variability in the combustion strategy.

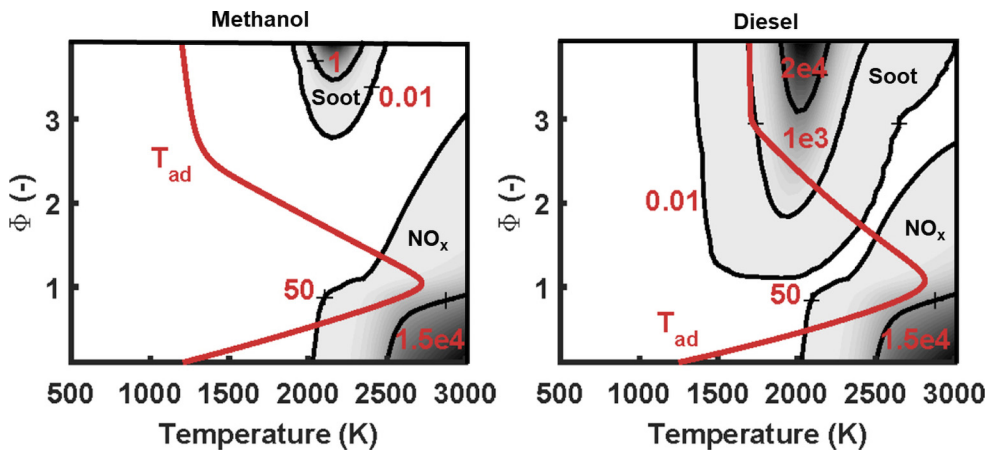


Figure 1.1. Φ -T diagrams for methanol (left) and diesel fuel (right). Adapted from [2]

According to the International Energy Agency (IEA), the transportation sector as a whole is responsible for 24% of direct CO₂ emissions from fuel combustion, with road-going vehicles accounting for approximately 75% of that, with the rest being the aviation and shipping industries [3]. During the SARS-CoV-2 virus outbreak in 2020 however, the total road transport reduced by 50-75% according to the same source. Nevertheless, the current figures are quickly rising to the pre-pandemic levels and the fight for global CO₂ emissions is raging stronger than ever before. When it comes to personal transport, for the last two decades approximately, the goal has been to reduce CO₂ emissions, something that pushed the development of light-duty diesel engines and their market share exceeded 50% over gasoline powered vehicles in some European markets. In 2015 however, in what is commonly referred to as the VW emissions scandal or diesel-gate, some diesel cars were found to far-exceed some of their emission claims in real-world driving. This was due to a software calibration that allowed the vehicle to know if it is being tested for emission purposes or if it is simply driven on the road. Of course, this was illegal and by all means reprehensible, nevertheless the motivation for the manufacturer to incorporate such a system is rather interesting. In diesel engine literature, the soot-NO_x trade-off is a well-documented mechanism, and some examples can be found in [4-8]. NO_x refers to NO and NO₂, and while NO is not toxic it quickly gets oxidised to NO₂, which in high concentrations is toxic and contributes to photochemical smog. High combustion temperatures promote NO_x formation and soot oxidation at the same time, so if NO_x formation needs to be avoided, low combustion temperatures should prevail. Low combustion temperature, however, will lead to poor oxidation of the soot late in the combustion cycle and thus higher soot tailpipe emissions. In addition, reducing the in-cylinder temperatures is done by delaying the peak heat release which will result in loss of engine efficiency as the expansion stroke is effectively shorter. Lower efficiency means higher brake specific fuel consumption (BSFC), or higher fuel consumption for the same engine performance. Thus, arguably the cheating-calibration of these engines resulted in lower fuel consumption and subsequently lower CO₂ emissions as they are directly proportional. Nevertheless, in the years after the emissions scandal, diesel engines were considered a heavily polluting technology and became “dirty” in the general public’s minds, despite the fact that they offer unrivalled BSFC and CO₂ emissions. Modern diesel engines make use of a selective catalyst reduction (SCR) aftertreatment to convert harmful NO_x, in addition to a particle filter which was already established, thus, combustion strategies have shifted to favour high engine efficiency and soot oxidation.

In recent years, the alternative of battery electric vehicles (BEV) has become a reasonable proposition for personal transportation. Electric motors are exceptionally efficient at greater than 95%, in converting electric to mechanical energy and electric vehicles can recover a significant amount of energy during deceleration, thus managing exceptional energy usage under transient operation like city driving. Nevertheless, since they do not have any associated tailpipe emissions or local

emissions, they are wrongfully considered zero-emission vehicles. The electricity they use has a certain carbon footprint and it is important to look into the carbon intensity of the energy production in order to understand if the overall emission reduction they can offer is worthwhile. The average electricity mix in the EU is among the lowest in the world, emitting 269 grams of CO₂ per kWh, while that number for the grid average in India is among the world's highest at 709 gCO₂/kWh, and the world average electricity mix is estimated at 475 gCO₂/kWh [9]. Furthermore, the production of the batteries is a carbon-intensive process, with recent studies reporting a CO₂ penalty of 60-120 kg of CO₂ per kWh of stored power [10, 11] and should be factored in the analysis. Let's devise a simple case to compare two similar cars with one battery-electric propulsion system and one with a diesel-powered ICE. Let's assume that they both drive on the motorway at a constant speed of 120 km/h, a rather efficient mid-size electric vehicle will consume 0,23 kWh/km and the diesel car will consume 5 litres per 100 km, which is also a realistic fuel consumption for an average size vehicle. The electric car is equipped with a 70-kWh battery which is an average capacity of battery packs for BEV's on the market today. If we assume that the vehicles life cycle will be 200.000 km and the emissions from battery production are 100 kg CO₂/kWh, that will lead to a toll of 35 gCO₂/km travelled. With the EU electricity mix of 269 g/kWh, the total CO₂ emissions are 97 g/km. With the world average mix that figure becomes 144 g/km and in India it jumps to 198 g/km. Meanwhile, the fossil fuelled car will emit 164 g/km if it is fuelled by 100% fossil diesel, with 25% of those emissions attributed to the production of the fuel (10.3 gCO₂eq/MJ, converted to 640g/l) according to some studies [12, 13]. To summarise, the BEV will offer a reduction of 40% of emissions with the EU mix, 14% with the world average, and an increase of 20% in emissions if it is driven in India. Thus, the emission reduction potential is heavily dependent on the source of the electricity at the individual country level and is nowhere near as impressive as the zero-emission claim. On the contrary, if the diesel car is fuelled with renewable HVO the emission reduction potential is significant. According to literature studies [14, 15], the carbon footprint of HVO can range from below 5 and up to 80 gCO₂/MJ depending on the feedstock and the energy used to produce it. If we use an average value of 40 gCO₂/MJ (1276 gCO₂/l), the resulting emission figure in our example is 69 gCO₂/km. Now if we invert the question to how clean the electricity grid needs to be to make an electric car a cleaner option than an ICE vehicle, we derive that to surpass a pure fossil diesel, the electric grid needs to emit less than 561 gCO₂/kWh and comparing to 100% HVO, the grid should emit less than 148 gCO₂/kWh (based on 40 gCO₂/MJ). In addition, many studies show that HVO drastically reduces soot emissions by up to 35% [16-21].

From this analysis, it is easy to understand that a diesel-hybrid vehicle running on HVO biodiesel will be a much cleaner overall option in most countries as it can offer low emissions on motorways and remain efficient in transient operation with energy recuperation. A much more thorough analysis that reaches the same conclusion can be found at [22]. Combustion engines also benefit from the fact that,

with hybridisation, they can be operated at their optimally efficient load/rpm range for the majority of the time, meaning that they can maintain a higher overall fuel efficiency. In Figure 1.2, the 2019 greenhouse gas emission of electricity generation is shown for many European countries according to [23], along with the break-even points mentioned previously. This figure illustrates that for the majority of countries within the EU, the best solution is biofuels and only few countries can benefit from the switch to BEV's. In some cases, BEV's are a worse alternative even compared to pure fossil diesel, which is rather controversial, considering the fact that people are incentivised to switch to these vehicles believing that they are less polluting. There is true merit to the use of biofuels as they offer a much quicker transition to low emission transportation without the associated inconveniences of long charging stops and higher buy-in cost of battery electric vehicles. Existing ICE vehicles can reduce their emissions without needing to be retired prematurely which would increase the life-cycle emissions of those vehicles, and the same benefits can be seen in heavy-duty vehicles, the shipping and aviation industry, where the energy density of batteries is simply not enough with current technologies. Thus, renewable fuels present an opportunity to rapidly transition, not only personal vehicles, but the whole transportation sector and potentially the energy sector as well. These “drop-in” fuels rely on existing infrastructure for distribution and use, instead of requiring big investments from people and regulatory authorities on an only conditionally cleaner technology. A common concern regarding biofuels is the use of arable land and competition with the food supply chain but modern biofuels like HVO and methanol rely on waste products and feedstocks that do not require new farmlands to be grown on [14, 15, 24-26]. Sadly, it has been more than 100 years since people have known that alternative fuels offer a sustainable future, with Rudolf Diesel himself demonstrating his engine running on peanut oil in the 1900 Paris World's-fair [27]. His ultimate goal was to make his engine readily available to people, not rely on the oil industry and eliminate the use of bulky and inefficient steam engines.

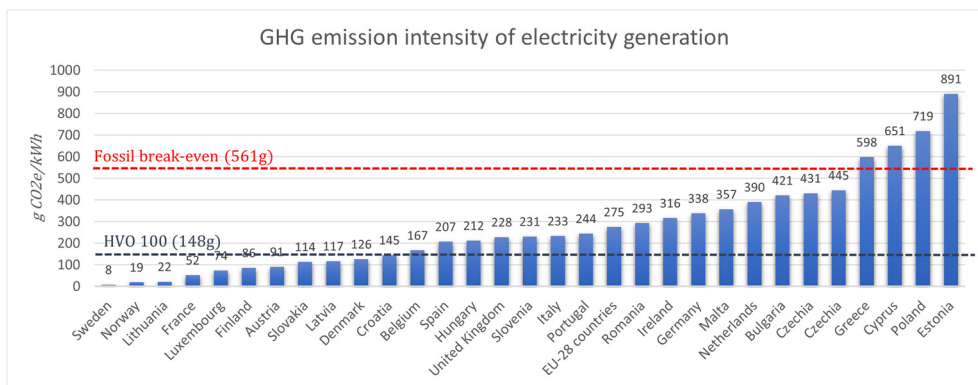


Figure 1.2. Greenhouse gas emission intensity of electricity generation in European countries. The red line indicates at below which point a BEV emits less than a diesel-powered vehicle in the given example, while the black line shows the break-even point if the diesel vehicle is fueled with 100% HVO. Data from [23]

Among the potential renewable fuels, methanol particularly stands out due to its versatility. Currently, methanol is mainly derived from natural gas, yet it can be produced renewably from a variety of feedstocks that have low cost and can be efficiently reformed to bio-methanol. Such feedstocks can be biomass from agricultural and municipal waste, forestry residues, unrecyclable plastic waste [24, 25, 28-35] and can even be used effectively to store electricity with high efficiency combined with CO₂ capturing [28, 36-38]. Methanol can also be used as a building block for synthetic fuels such as gasoline and diesel through the methanol-to-gasoline and Fischer-Tropsch methods [35, 39]. It is among the most widely traded chemicals and, being a simple molecule, it is commonly used as a building block in the synthesis of many plastics and other chemical products, thus production and distribution networks exist everywhere in the world. Given that methanol is a liquid, it offers easy storing and transportation, along with relatively high energy density in comparison to gaseous fuels that have been proposed as renewable fuels. If methanol were to be used directly as fuel, petrol stations could easily facilitate its sale as the storage and pumping demands are similar to the ones for ethanol, which are already present in many fuelling stations. Concerns are often raised over methanol's toxicity to humans but in reality, it is relatively benign, since the antidote (ethanol) is readily available, while conventional fuels and other commonly traded chemicals are far more toxic and harmful if consumed. It is important to note that while humans cannot metabolise methanol, the majority of other living species and mammals can. This would mean that in an event of spillage no significant or long-lasting harm is done to the environment and nearby flora and fauna. This presents unique retrofitting opportunities in the shipping sector since it would be safe to use the double hulls in ships as the fuel tanks for methanol, rather than requiring new separate fuel tanks.

In case the reader is wondering why this isn't the norm already with so many attributes, one reason would be that methanol is a fuel that is quite hard to ignite. Methanol has been introduced previously as an alternative fuel for slightly modified gasoline cars during the oil crisis in the 70's, but cold weather operation was problematic with the poor engine control systems available at the time. The reason for this is that methanol's ignition resistance is among the highest among all fuels and cold-starting engines fuelled with methanol in cold climates can be hard. This auto-ignition resistance makes the use of methanol in Diesel engines an even more absurd proposition, as these engines rely specifically on the ignitability of the fuel to operate. Nevertheless, multiple-injection strategies can make auto-ignition easier, as an early pilot-injection facilitates the longer ignition delay required when in-cylinder temperatures are lower. In addition, since higher cyclic variations are observed with methanol [40, 41], some alternative combustion control method can be utilised, such as glow-plug or sparkplug assisted combustion (SACI) to help control heat release and cold-starting performance. Nevertheless, a key factor in soot emissions from engines is the chemical composition of the fuel itself. Aromatic content in fuel is known to increase sooting tendency of an engine as aromatic

molecules essentially enable the formation of soot, acting as nucleation sites [16, 42-47]. This is an area where alcohols provide a unique opportunity, particularly methanol being the simplest molecule. Alcohols contain oxygen in their molecule, thus loosening the requirement for adequate mixing with air before combustion occurs, which is another key aspect of soot formation. For a given number of carbon atoms, methanol carries the most oxygen from its siblings, leading to a fuel that is practically impossible to form soot during combustion. This alone makes methanol a great candidate for diesel-like combustion, where high efficiency can be combined with extremely low soot emissions, which for conventional diesel combustion has traditionally been the Achilles-heel. Generally very little research has previously been performed on methanol injection, with most applied on injectors relevant to spark-ignited engines [48-51], some early research on injectors relevant to compression-ignition [52-54] and finally some on optically accessible engines [40, 55]. A big part of the work presented in this thesis came as a result of a project named MOT-2030 that aimed at demonstrating the potential of methanol as a renewable transportation fuel. In chapter 5.2, we will present an in-depth optical investigation of the combustion and injection processes of methanol relevant to compression-ignition engines operating under PPC and diesel-like combustion.

Another field where this thesis contributed was studying aspects of diesel combustion, since it remains the most efficient combustion process for internal combustion engines. Often the injection process in Diesel engines is split in multiple sections, in order to better control combustion rate, pollutant emissions and noise emissions. The interaction between these multiple injection events and the resulting combustion characteristics is not well understood and some misconceptions exist around the origin of perceived combustion noise in such a regime. Three different injection strategies were studied, and the resulting noise was found to originate in the magnitude and duration of undulations of the heat release from the combustion of these separate injection events. Small peaks and dips in the heat release resulted in less noise, despite combustion rate and peak cylinder pressure being higher. Pressure rise rate and peak cylinder pressures have commonly been used as predictors of high combustion noise. Additionally, we studied how each section of this split injection strategy behaves depending on the pre-existing conditions in the combustion chamber. The main factors affecting the strategy are, number of individual injections, the duration of each and the resulting separation between them. Based on these parameters results vary from instant ignition of the fuel jet by pre-existing combustion, to extinction of this already set combustion from an earlier injection until the newly admitted fuel is heated to the point of auto-ignition. This whole process was studied by probing both, the intermediate combustion species as well as the subsequent flame luminosity and resulted in one of the very few published studies to perform such measurements on an optical engine. Such studies are commonly performed in stationary combustion vessels with much easier optical access, while this study was performed in conditions as close to realistic as possible

and with a piston geometry typical of what can be found in production Diesel engines.

Moving away from combustion engines, another field where optical and laser-diagnostics have contributed greatly is medicine and pharmaceuticals. By offering remote and non-intrusive measurement methods, they can replace more invasive techniques commonly used in medicine. Applications range greatly from small scale measurements like estimating drug delivery, measuring oxygen saturation levels, aiding design of spray systems and inhalers, to large scale visual tools like PET and CT scans. In the turn of 2020, millions of lives were lost due to the SARS-CoV-2 virus pandemic. With travel restrictions, compulsory use of face mask, work furloughs, hobbies suspended, even outdoor curfews applied in some countries, the entire world is still in some form of lockdown, more than a year since the outbreak. Early on, the virus was identified to transmit through the respiratory system and the exhaled particles. Social distancing routines were first applied with a seemingly generic, 2-meter suggestion. In some areas, face masks were necessitated indoors soon after, again with little scientific evidence at the time [56]. This provided the motivation for our study on exhaled respiratory particles. High-speed imaging of scattered light was used to visualise the exhaled liquid droplets from a number of participants that were given tasks, like talking and singing at different volumes and tonalities. Singing was a key activity that hadn't been explored extensively previously [57] and choir singing was linked to an increased rate of transmission. The early results showed the number of particles emitted during these tasks and in upcoming publications will show their speed and trajectories.

2. Optical Techniques

In this section, all the optical techniques used for the research in this thesis will be introduced. The purpose, however, is to briefly introduce the field and how it is used within this work, be it spray and combustion applications or exhaled droplets.

2.1. Natural Luminosity

For a better understanding of the chemical processes on a molecular level, the imaging of the natural luminosity of the flame is of great interest. A set of examples of various sources of natural luminosity is shown in Figure 2.1, where in the left image, an early injection strategy is shown where combustion chemiluminescence is captured. In the middle image the delayed injection timing results in fuel-rich combustion and the addition of soot luminosity combined with chemiluminescence. On the right, as injection timing is delayed further, a diffusion flame is seen and as even less air and fuel mixing occurs, the soot emission dominates the image.

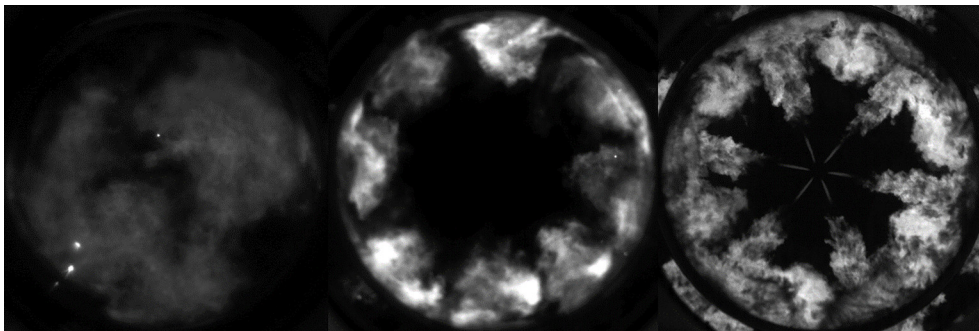


Figure 2.1. Example images of natural flame luminosity from an optical engine are shown, going from mainly chemiluminescence on the left image, to progressively increasing soot luminosity in the middle and the right where it dominates the emission spectrum.

There are many intermediate steps which occur through multiple chemical reactions in combustion and various radicals are formed in different stages of the combustion process. Chemiluminescence is the emission of electromagnetic radiation by excited

molecules, caused by these chemical reactions. The light emission by the excited molecules during the de-excitation process can be captured with the help of a detector and the acquired emission spectra is used to identify the molecules that are present. Each molecule emits a unique radiation footprint at certain frequencies and the intensity of the chemiluminescence depends highly on the flame temperature, the fuel-gas composition and the equivalence ratio.

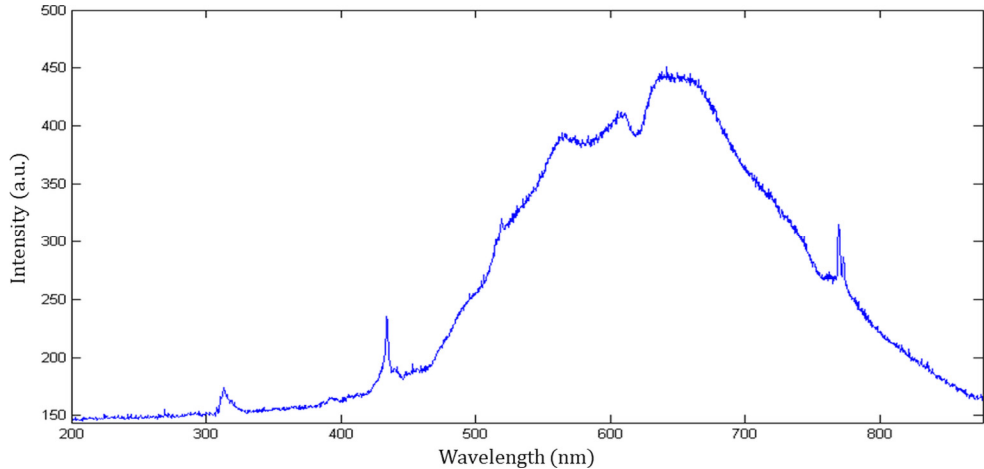


Figure 2.2. Spectrum of chemiluminescence imaging of a premixed methane-air flame in high equivalence ratio where the Planck radiation is dominant in wavelengths above 450 nm. Intensity peaks appear from emission of OH and CH at 308 and 430 nm, respectively.

An example of an emission spectrum from a fuel-rich, premixed methane-air flame is shown in Figure 2.2. Excited OH, CH, C₂ and other radicals are important indicators of the flame front and temperature and can be used to identify the different regions of the flame structure, such as the preheat zone, the reaction zone and the post flame or product zone. The preheat zone is the region where the reactants are heating up before they reach the reaction zone where the radicals are formed through various chemical reactions. The hot products of those reactions are present in the post flame zone; therefore, it can also be referred to as the product zone.

The emission peaks of excited OH and CH radicals occur at around 308 and 430 nm, respectively, as seen in Figure 2.2. The broad-band radiation which dominates in longer wavelengths is identified as Planck or black-body radiation which occurs in rich flames because of soot formation. Soot particles are agglomerates of small, spherical carbonaceous particles which emit black-body radiation when heated. The spectral distribution of the background luminosity increases rapidly at longer wavelengths as it follows the Planck distribution law:

$$I(\lambda) = \frac{2\pi hc^2}{\lambda^5} \frac{1}{e^{hc/\lambda KT} - 1} \quad (2.1)$$

where K is the Boltzmann constant and h the Planck's constant.

With the help of the Wien displacement law, we can also determine the temperature; as it increases, the highest spectral intensity corresponds to shorter wavelengths.

$$\lambda_{max}T = 2,898 \times 10^{-3} [K \cdot m] \quad (2.2)$$

Finally, the Stefan-Boltzmann law describes the dependence of the intensity to the flame temperature,

$$I = \sigma T^4 \quad (2.3)$$

where σ is Boltzmann's constant, $\sigma = 5,6703 \times 10^{-8}$ watt / m² K⁴.

2.2. Elastic light scattering

Elastic scattering occurs when light falls on particles and it is usually referred to as Mie scattering in honour of Gustov Mie who was the first to investigate this type of scattering in the early 1900s. It is worth mentioning that Mie scattering is not an independent physical phenomenon as is commonly believed, where people separate the Mie-regime and the Rayleigh-regime. Mie theory is a definite solution to the Maxwell's equations for the radiation from electric polarization of the molecules in the particles that scatter the incident electromagnetic wave. Rayleigh scattering only explain the regime of scattering when the wavelength of light is similar or smaller than the size of the particles, named after Lord Rayleigh, who first described this regime. Nevertheless, Mie theory also describes the Rayleigh regime. In the work relevant to this thesis such small particles cannot be detected, since their scattering is too weak to detect in low number densities.

The Mie solution shows that the scattering and extinction cross section, each normalized to the particle geometric cross section $\alpha = \pi d^2/4$, can be expressed as,

$$Q_s = \sigma/\alpha = \frac{2}{x^2} \sum (2n_p + 1) [|\alpha_n|^2 + |b_n|^2] \quad (2.4)$$

with $x = (2\pi/\lambda) \cdot (d/2)$, where d , the particle diameter and λ the incident wave wavelength. n_p is the order of the multipole expansion of the polarization from charge oscillation within the particle. The coefficients α_n and b_n , represent the contribution of the multipoles of order n_p . It is important to note that the absorption cross section is the difference of the extinction and scattering cross sections.

In case the size of the particles we need to probe is known, there are programs that can calculate the scattering properties of these particles. In such cases, we can iterate and try to find the optimal imaging and lighting setup specifically for the

application. One opensource program that is very easy to use and provides many illustrative results is Mieplot, where the graphs in Figure 2.3 were made. By changing the light wavelength and the size of the droplets, we can see the scattering properties of the setup. As an example, in the left graph of Figure 2.3, we can observe the polar diagram of particles with a size of $0.1\ \mu\text{m}$. If the light we are using for the experiment has parallel polarisation, we can observe that, at a detection angle of 90° , we wouldn't observe any signal. However, in the case of $1\ \mu\text{m}$ particles, the polarisation dependence is greatly reduced

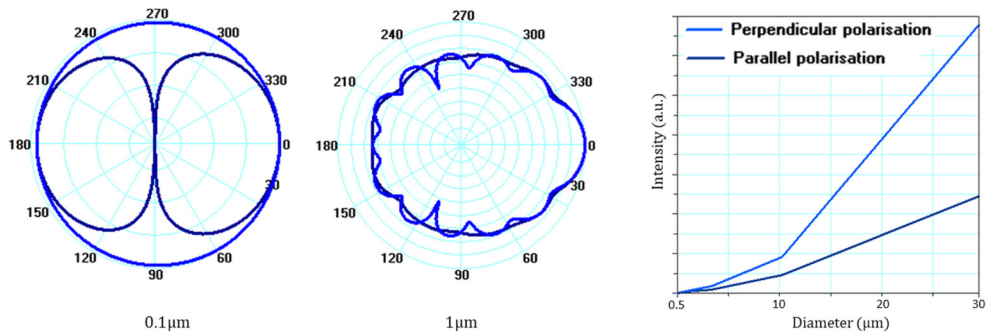


Figure 2.3. Polar diagrams of two different sizes of particles. The detection sensitivity is much reduced for small particles ($<1\ \mu\text{m}$) at a 90° detection angle and for light with parallel polarisation. On the right, a plot of intensity versus particle size is shown.

2.3. Laser-Induced Fluorescence

Laser-induced fluorescence (LIF) is a non-intrusive diagnostic technique that is commonly used to study combustion processes. A laser source is tuned to an allowed transition from a lower to an upper energetic state of the species under investigation and the detector captures the light emission during the decay in the ground state. This de-excitation will occur in a few nanoseconds and the emitted light will occur at a wavelength longer than the excitation wavelength. Radiation emitted by laser stimulation is well defined when it comes to its frequency, is in phase and coherent with the stimulating radiation, which makes it an important factor in spectroscopic measurements. A simple form of the involved processes in LIF are shown in Figure 2.4. The laser source stimulates a particle and excites it to a higher energetic state by the absorption of a photon with $h\nu_{12}$ energy. During the temporal decay of the particle from the excited to the ground state, two processes need to be considered, the stimulated and the spontaneous emission. The losses in the LIF mechanism such as the stimulated emission of photons that propagate in the direction of the incoming laser beam as well as the collisional quenching without a photon emission, should also be considered.

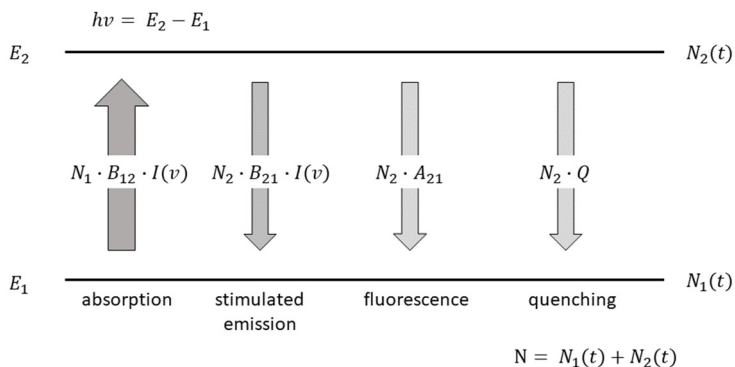


Figure 2.4. Illustration of the physical processes involved in laser induced fluorescence.

The applications in this thesis however focus on LIF of larger molecules such as acetone and formaldehyde which emit much wider than the atomic transitions and span a few tens to a few hundreds of nanometres. In addition, they have many possible excitation transitions and thus the laser source used can be selected based on the properties of the de-excitation occurring.

2.4. Shadowgraphy and Schlieren photography

Shadowgraph and Schlieren photography are two techniques that were devised to detect density gradients in media. Both techniques rely on the fact that the refractive index of media, will change depending on their density. These techniques date back to the early 1600's and Robert Hooke, who first described the visualisation of streaks on non-uniform glass and heat convection off a candle, among other observations. Since then, of course multiple iterations of essentially the same principle have been proposed. In the last century, these techniques have been pivotal to our understanding of aerodynamics, supersonic flight, flows and shockwaves.

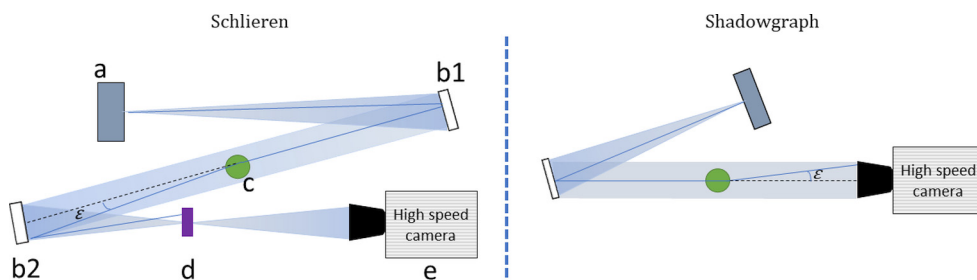


Figure 2.5. A typical Z-type Schlieren setup is shown on the left and an example of a shadowgraph setup is shown on the right. There are multiple variations of both setups and these are only shown for illustration purposes. The light source is highlighted as **a**, the two mirrors as **b1** and **b2**, the density variation as **c**, and finally the cut-off by **d**.

Both techniques use collimated light to illuminate a volume where the test subject is placed. Let's describe a typical Z-type Schlieren setup first in order to understand the physical processes involved. Such a setup can be seen in Figure 2.5, along with a typical Shadowgraph setup. A very bright, point source of light source (**a**) is used to create a divergent beam or a spherical front, which passes through a converging mirror (**b1**) to become planar, thus forming a column of collimated light if the source is positioned at the focal length of the mirror. Another mirror (**b2**) is placed along the path of this collimated light to converge it again towards a focal point, at a distance dependent on the focal length of the second lens introduced. Let's call the area between the two mirrors the test section. At this stage, an exact image of the light source will have formed again. However, the focal point of a lens is mathematically described as a Fourier plane, and at this plane the Fourier transform of the image received by the last mirror is formed. In the Fourier plane, the intensity values that comprise the original image are translated to frequencies. If all light is collimated, and the light source is infinitely small, only one frequency component will be present and appear as a round dot. Now, if we introduce a sharp opaque plate as a cut-off (**d**), some frequencies will be blocked leading to a new image. If the cut off is positioned so that half the Fourier plane is blocked, the intensity of the final image will be half of the original image since half the frequencies will be blocked. However, rays that diverge collimation, due to some disturbance in the test section (**c**), will also be part of the Fourier plane, only spatially placed outside the central frequency, since they are not part of the collimated light. Depending on the direction of divergence from collimation, this new component will either, be filtered according to the cut-off position, or it will manage to escape the cut off that was introduced and appear 100% of its original intensity, or it will be blocked completely and appear dark on the final image. This is also shown in Figure 2.6. The detection of the density gradients is thus performed based on the intensity variation compared to the undisturbed image. Other forms of cut-offs can also be used to manipulate the frequency components and will provide different results based on the frequencies blocked.

In Schlieren systems, a trade-off exists between the sensitivity of the systems and the measuring range. Provided that the cut-off is perfectly opaque, the deflected rays blocked from the cutoff will appear perfectly dark on the reconstructed image or, if they escape the cutoff perfectly bright. If greater measuring range is required, a few measures can be taken, at the expense of lower sensitivity. If the size of the light source is increased, less light will be collimated and therefore a less defined focal point is formed at the Fourier domain and more frequencies will escape filtering. Another technique would be to use a graded filter instead of the sharp cut-off previously mentioned, where the gradation length of this filter will define the measuring range of the setup. Longer gradation will provide low sensitivity with great measuring range and conversely, short gradation results in smaller range, similar to the case of a sharp cut-off. In addition, the position of the cut-off can be

used to define the sensitivity of the setup, since it defines the amount of filtering in the Fourier domain. However, the system response becomes non-linear away from the 50% position, especially below 10% or above 90% positions [58].

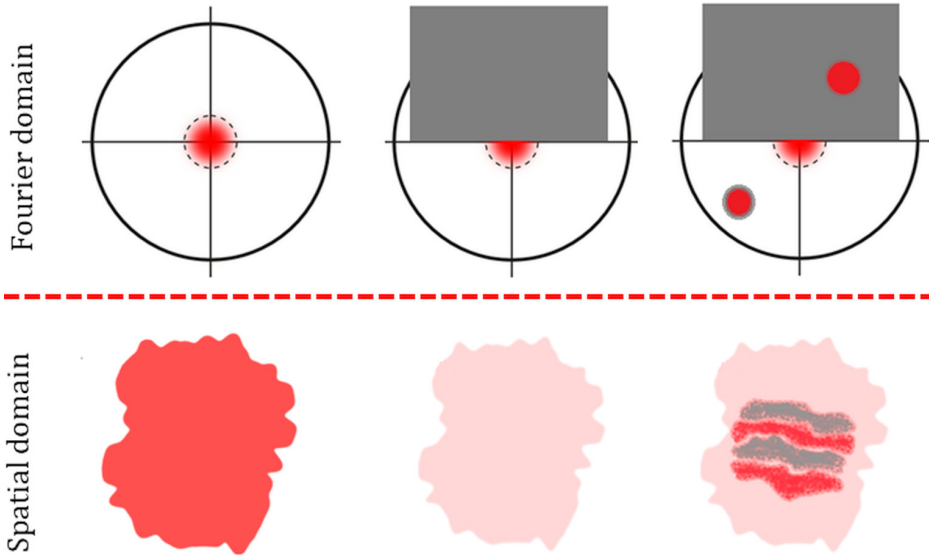


Figure 2.6. Illustration of how the cut-off affects the image in Schlieren techniques. If the cut-off is positioned at 50%, the final image intensity is evenly reduced by 50%. Once a density gradient introduces new components on the Fourier domain, some will be blocked appearing darker than the background and some will escape the cut-off and appear brighter than the background.

Shadowgraphy is very similar to the Schlieren technique, as the detection of density gradients again relies on rays that escape collimation and provide some contrast, proportional to their deflection. This time the cut-off filter is removed along with the second lens and, essentially, the only requirement is a light source that can provide collimated light. Thus, the experimental setup is much simpler and easier to use, requiring only a source of collimated light and a screen or camera sensor to measure the displacement of light rays.

Since these imaging systems rely on pure geometrical optics principles, the governing equations are relatively simple. By knowing the geometry of the Schlieren or shadowgraph optical setup, the deflection angles can be calculated and the density gradients that caused them can be derived. For air and other gases, the refractive index n and gas density ρ are related according to:

$$n - 1 = k\rho \quad (2.5)$$

where k , the Gladstone-Dale coefficient. In most cases the pressure, temperature and density at close to atmospheric conditions, are related by the ideal gas law:

$$\frac{p}{\rho} = RT \quad (2.6)$$

where R , the ideal gas constant. It can be shown that optical inhomogeneities refract light rays proportionally to the gradients of their refractive index and the resulting ray curvature is given by:

$$\frac{\partial^2 x}{\partial z^2} = \frac{1}{n} \frac{\partial n}{\partial x}, \quad \frac{\partial^2 y}{\partial z^2} = \frac{1}{n} \frac{\partial n}{\partial y} \quad (2.7)$$

where x and y are the Cartesian coordinates corresponding to the direction that the gradient deflected the ray on the image plane. By integrating along the optical axis (z direction), the ray deflection angles ε become,

$$\varepsilon_x = \frac{1}{n} \int \frac{\partial n}{\partial x} \partial z, \quad \varepsilon_y = \frac{1}{n} \int \frac{\partial n}{\partial y} \partial z \quad (2.8)$$

and for a disturbance extent of L along the optical axis the equations become,

$$\varepsilon_x = \frac{L}{n_0} \frac{\partial n}{\partial x}, \quad \varepsilon_y = \frac{L}{n_0} \frac{\partial n}{\partial y} \quad (2.9)$$

In the case of the Schlieren system, if we use the small angle approximation ($\tan \varepsilon \approx \varepsilon$), a ray displacement of $\Delta \alpha$ at the cut-off position will be described by:

$$\Delta \alpha = \varepsilon f \quad (2.10)$$

where f , the focal length of the second lens. If the light source is uniformly bright, the image contrast ($\Delta I/I$), or equivalently the sensitivity, will be given by:

$$\frac{\Delta I}{I} = \frac{\Delta \alpha}{\alpha} \quad (2.11)$$

where α , the size of the source's image on the focal point. Combining the above we obtain:

$$\frac{\Delta I}{I} = \frac{\varepsilon f}{\alpha} \quad (2.12)$$

From this simple equation it is easy to notice that the sensitivity of the setup will rely on the size of the source and the focal length of the second lens.

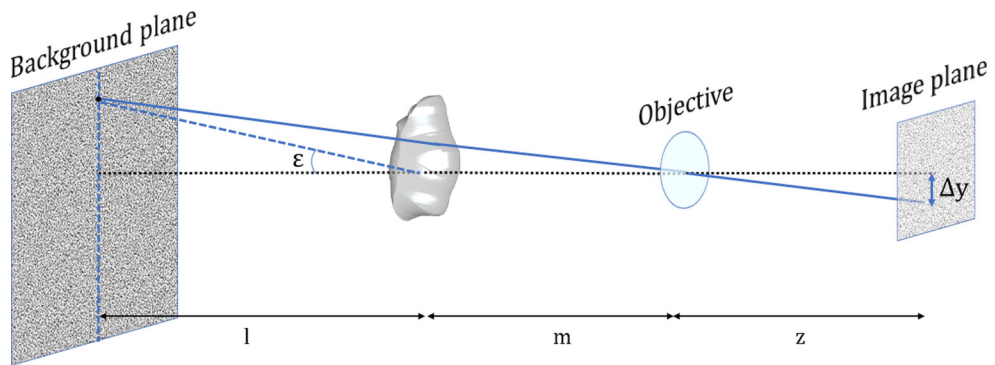


Figure 2.7. Illustration of the BOS principles and major units used to characterise the optical system.

In addition to the classical Schlieren techniques, more modern methods are less complicated and mostly rely on computational methods. For example, Background Oriented Schlieren (BOS) is a technique that, similar to Shadowgraph setups, only needs a detector and a characterized background image. This background image is used to obtain unique features and reference points that, once a disturbance is introduced, will change position according to the density gradient that forced them to be displaced. These reference points are compared to the background image and retraced in the new one and the displacement magnitude can be measured. Cross correlation algorithms perform the evaluation, in the same fashion as in Particle Image Velocimetry (PIV) measurements, and the displacement vectors are obtained. These vectors contain information regarding both, the magnitude of the disturbance and the directionality. Thus, only by obtaining two images, all of the necessary information is obtained without needing the complicated setup and evaluation methods required for Schlieren methods. Additionally, the BOS technique is not limited by hardware limitations, such as the mirror size and power of light source, and can thus be used in large scale applications such as full-size helicopters, airplanes in flight [59], ventilation hoods, etc. [58, 60-63]. Additionally, due to the simplicity of this method, multiple camera sensors and background patterns can be used to create a tomographic setup and reconstruct the density gradients in three-dimensions.

The parameters that define the capabilities of BOS are, the background pattern and the allowed distance of the density gradient, relative to the characterised background. The background pattern most commonly is comprised of randomly generated dot patterns, that are big enough to be detected with the camera's optical resolution, yet small enough to offer high spatial resolution of the displaced features. Nevertheless, anything can be used as a background image, provided that enough unique features can be found on them to be traced in the cross-correlation. The displacement of the feature however, and subsequently the sensitivity of the system, is mostly dependent on the distance of the density gradient to the background image.

The equations previously described still apply, and thus the deflection angle ε will force the feature to be displaced on the image plane. If Δy is the displacement of the feature on the image plane, then the equation to describe it is given by:

$$\Delta y = l \cdot M \cdot \varepsilon \quad (2.13)$$

where $M = z / (l + m)$, which is the magnification factor from the objective lens and the geometry of the setup. Thus, the density gradient that caused the displacement can be derived. The optical system, however, in these applications needs to be focused on the background for optimal contrast. Yet optimal sharpness of the density gradients is achieved when the detector is focused on the density gradients. This sharpness limitation is an inherent problem in BOS techniques.

A rather promising technique named Laser-Speckle BOS is discussed in section 5.4. A laser light source is used to create a speckle pattern on a screen, which is formed due to the interaction between the laser's coherent light and the projection screen. This usually undesirable effect creates an ideal dot pattern that can be used as a background image for BOS and provides the benefit of not needing to focus the detector on the target.

3. Equipment

An introduction to the equipment commonly used in optical and laser diagnostics is given in this section, particularly regarding imaging applications. In addition, optical engines are described which are essential in characterising combustion inside internal combustion engines.

3.1. Signal Filtering

Often, the raw signal we are trying to capture is convoluted with other sources of light that interfere with our measurement or sometimes the emitted signal is too high and needs to be suppressed. In these cases, there are a few tools that we can use to isolate and manipulate the signal, either spectrally or temporally.

As seen in section 2.1, natural flame luminosity can include the chemiluminescent footprint of combustion radicals, such as OH, CH, C₂, etc., and it can incorporate black-body radiation from soot particles. Often, when a lot of soot is produced during combustion, black-body radiation overwhelms many other features in the spectrum emission. Thus, it is important to first study the spectrum of the emission we want to analyse, since it might be impossible to capture the appropriate signal. Each emission has certain characteristics that we can utilise to our advantage, for example, soot luminosity will not reach into the UV region and thus OH which emits around 310 nm can still be resolved. Nevertheless, the detectors are usually sensitive to the whole spectrum and we need to somehow exclude all other interfering signals and keep the one we are interested in and this is usually done with optical filters. These allow us to select the wavelength regions that we need to capture and while many different types exist, they are separated in three major categories, shortpass, longpass and bandpass. As their name would suggest, shortpass filters allow wavelengths shorter than the cut-off threshold to be transmitted, and the opposite applies for the longpass. Bandpass filters allow only wavelengths within a certain range, called bandwidth, to be transmitted while the rest is absorbed. If the wavelength band we want transmitted is too specific in terms of region and bandwidth, a combination of one longpass and one shortpass can be used instead. Other filters exist, such as notch filters, that only reject a very narrow bandwidth and are usually made to reject the wavelength of a laser light in order for it not to be captured by the detector. Such filters are made for fluorescence detection, where the

laser is used as an excitation source and should not be measured. The most important parameter for all filters is the Optical Density (OD), which is a unit that determines how effective the filter is in rejecting the wavelengths that we want to exclude. This number ranges from 0 to 12 commonly and refers to the ratio of the incoming to the outgoing signal, expressed in terms of percent Transmission, as $T=10^{-OD} \times 100\%$. So, a signal that arrived as 10^6 , in arbitrary units, passing through an OD-6 filter will transmit only 1. When the signal is too high and we need to avoid saturating the detector, neutral optical density filters can be used which uniformly reduce the signal across the whole spectrum, according to their OD number.

Another way of adjusting the total intensity of the signal is by manipulating the imaging system that we are using. A well-known example of this is the aperture of an objective lens of a camera. The aperture can be opened and closed to adjust the intensity of the imaged feature and this is expressed in the f-number (f) of a lens, given by the expression $N=f/D$, where f is the focal length of the lens and D is the diameter of the aperture inside the lens. Usually the number is quoted unitless, as $f/$, followed by the ratio directly, without mentioning the focal length of the lens, as in a 100 mm length lens with an aperture of 50 mm will have $f/2$. Narrowing the aperture results in reduced total signal and a loss of fidelity or softness of the final image, if high f-numbers are used.

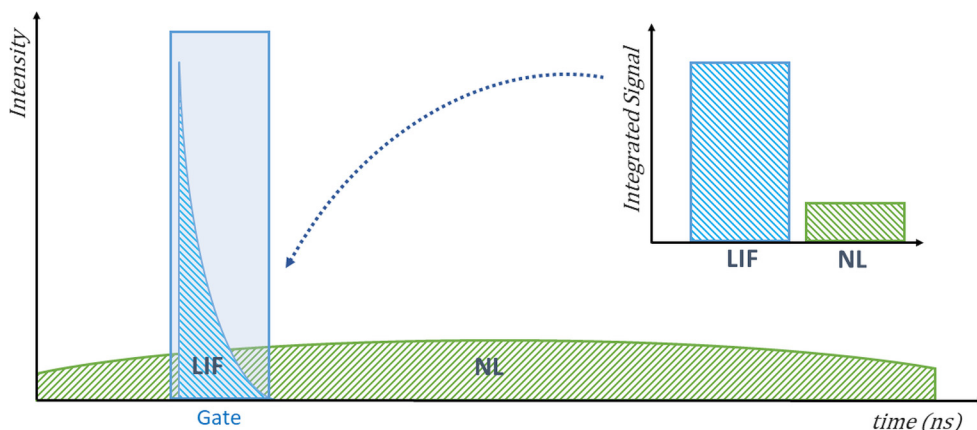


Figure 3.1. Illustration of the concept of temporal gating. If the signal we are capturing exists for a short period only, by exposing the detector just for the duration of this feature, the time-integrated signal will be dominated by that instead of any background signals. Such a case is in laser induced fluorescence where the lifetime of the fluorescence is shortlived.

Sometimes the signals that comprise the spectrum of the emission we are trying to capture have different lifetimes. One example of this is in LIF experiments where the lifetime in most cases is in the order of a few tens or hundreds of nanoseconds. Often in such measurements there might be other signals interfering, like soot luminosity, which also emits strong, but the time integrated signal will not be as strong. An illustration of this can be seen in Figure 3.1, where the background is

labelled as natural luminosity. Effectively, if the detector we are using is a camera, we try to expose the sensor only for the duration of the feature we want to record, and this will be the “gate” over which we integrate the signal. By doing so, the integrated signal from the fluorescence will be higher than any other interfering signal.

3.2. Detectors

While many types of detectors exist, in the context of this thesis, by detectors we will refer to camera sensors since all the applications presented regard imaging. There are two main types of camera sensors, the Charge-Coupled-Device (CCD) and Complimentary-Metal-Oxide-Semiconductor (CMOS). A brief overview of the important aspects of the two imaging sensors can be found in [64]. In CCD sensors, the charge created by the photons that are absorbed during the exposure is passed along from one pixel to another across the rows of pixels, until the read-out channel is reached and subsequently the charge is converted to voltage and is read-out across the row. CMOS sensors however, incorporate read-out circuitry in each pixel, which allows for parallel readout of the whole sensor. This voltage read-out from each pixel is much faster than the rolling charge implemented in CCD sensors, therefore high-speed cameras are almost exclusively based on CMOS sensors. Nevertheless, the pixel-level voltage probing performed in CMOS sensors results in a less accurate measurement of the charge stored in the pixel and, traditionally, CCD cameras yield better signal-to-noise characteristics. However, more modern iterations of CMOS sensors branded as scientific or sCMOS can achieve high frame rates and low noise, the main novelty being better amplification of the voltage read-out, by using improved Analog-to-Digital Converters (ADC), in addition to having greater dynamic range. Finally, the Intensified-CCD (ICCD) cameras use CCD sensors along with a photocathode, a Microchannel plate (MCP) and a phosphor screen. When the photons from the imaged feature reach the photocathode, photoelectrons are emitted, and an electric field is applied to draw them towards the MCP. In the MCP, the primary photoelectrons create secondary electrons from the channel plates, resulting in a cascade of electrons to develop. This cascade of electrons then strikes the phosphor screen resulting in a greatly amplified signal compared to the received image.

Quite commonly in imaging applications, we need to perform measurements where the absolute intensity is an important parameter and the signal we are trying to capture is most often comprised of many different wavelengths. In such cases, the quantum efficiency and the spectral response of the detector that is used to capture the images needs to be known and well characterised. Often the detectors response is not linear, so the correspondence between the incoming light intensity and the measured intensity needs to be known and factored in the analysis. A typical

example of a spectral response of a camera sensor is shown in Figure 3.2 and the variation of the sensitivity versus wavelength can be seen. A unit commonly used to describe the spectral response is A/W, which is the ratio of measured current from the sensor in Amps, to the intensity of the incident light measure in Watt.

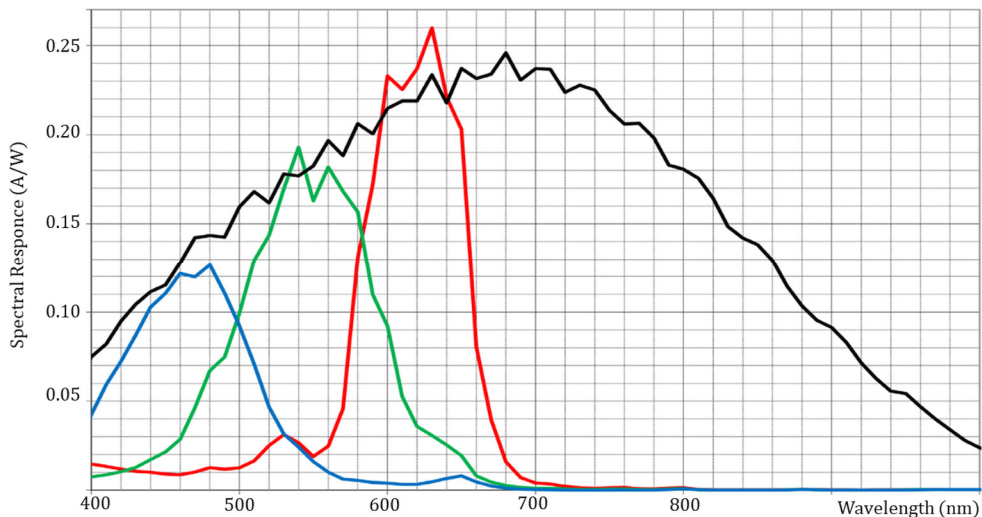


Figure 3.2. An example of the spectral response provided by the manufacturer, in this case from a Photron SA-X2, high-speed camera. The coloured lines show the spectral response for the colour sensor, while the black curve is from the monochrome sensor.

Another process that is commonly performed in digital cameras is the correction of the Fixed Pattern Noise (FPN). This noise pattern is specific to each sensor and needs to be compensated by a flat-field correction. Essentially, the sensor is shaded from any incoming light and a picture is taken; the signal captured in a dark environment is, by default noise, and thus can be set to zero. This FPN can change over time and depending on the temperature of the sensor, so it should be characterised during every experiment with the camera at operating temperature. Similarly to the FPN correction, another useful process is the flat-field correction, where the camera sensor is exposed to a constant homogeneous light profile and the divergence from homogeneity can be documented. This is usually performed by the camera recording in an integration sphere, which is a spherical volume that is painted white to reflect and homogenise the illumination pattern. If constant inconsistencies appear, with certain regions of the image brighter than others, the pixel gain is adjusted to compensate for the error.

In high-speed imaging applications, a trade-off is found between the repetition rate and the sensor area utilised. This results in a trade-off between temporal and spatial resolution of our imaging system. When a higher repetition rate is required, a smaller area of the imaging sensor can be used, thus offering poorer spatial

resolution. The reason for this trade-off is the rate at which the data can be read-out from the sensor and stored in a memory in the unit of time. Higher repetition rate means that more pictures are taken and thus a greater amount of data is created and needs to be stored. High-speed cameras use volatile memory, as in random access memory (RAM) modules, to temporarily store the information before they can be backed up in non-volatile storage, such as hard-disk drives. The data rate in such applications typically exceeds 30 Gigabytes per second and it is challenging for the electronic circuitry to offer such bandwidth. Nevertheless, we can decide to investigate a smaller area of the feature we are recording if both temporal and spatial resolution need to be retained.

3.3. Light sources

Here, we will discuss the light sources that are commonly used for research purposes. In the past, when film cameras were used, the repetition rate was limited from the light sources available and the speed at which the film was scanned. Faster film speed allowed quicker succession of frames, as long as the light source was pulsed, otherwise the image sequence would be blurred. With the advent of electronic imaging sensors, initially in the form of CCD or ICCD sensors, light sensitivity improved greatly but the repetition rate was compromised since each image must be read out and stored in the camera's digital memory. Traditionally in spray and combustion research, light sources need to be highly luminous and pulsed rather than continuous, either from the requirement to have ultra-short exposures to freeze the fast motion, or to keep low thermal load on optical components. These properties are provided by laser light sources, with a common drawback being their slow repetition rate. Typically, Q-switched lasers with a repetition rate of 10 Hz are used, that offer high pulse energy, narrow spectral bandwidth, short pulse-width and favourable beam properties like coherence and polarization, along with beam shape flexibility. The 10 Hz Nd: YAG laser systems have thus become the norm due to their wavelength being suitable for most combustion studies. To mention a few examples, the fundamental line of 1064 nm can be used for LII measurements, the second harmonic at 532 nm can be used for scattering of sprays, the third harmonic at 355 nm can be used to probe polyaromatic hydrocarbons, and the fourth harmonic with a wavelength of 266 nm is used to excite fluorescent tracers that can be added to the fuel and probe the fuel distribution. In addition, Nd: YAG systems can be coupled to a dye system, where a fluorescent dye is excited and, among the broad emission of the dye, the desired wavelength is selected depending on the application. A such, these systems are flexible tools that can be used in many experiments within the combustion diagnostics field.

For high repetition rate experiments, multiple laser cavities (usually 4) can be housed together, forming a cluster of lasers combined in a single laser module. Each

cavity is then triggered successively, resulting in a sequence of laser pulses with very high repetition rate. The repetition rate of these systems is effectively infinite since the cavities can be triggered at any time interval. These systems can also be capable of a dual pulse mode, originally required in particle image velocimetry (PIV) studies, where each cavity can fire two laser pulses in rapid succession, albeit at lower pulse energies. Typically, the separation between the double pulses is 10-20 μs , yet it is important to monitor the pulse energies as short separation usually results in the second pulse having lower energy, due to depletion of the gain medium after the first pulse. Another alternative for high temporal resolution are burst-mode systems, where multiple pulses are contained within a burst and high pulse energies can be obtained. These systems rely on a beam from a continuous fibre-coupled laser, which is then separated to individual pulses and subsequently, this pulse train passes through a number of amplification stages, depending on the energy and cost requirements of the application. Repetition rates of more than 100 kHz and up to 10000 pulses can be obtained typically, with very high pulse energies. A big caveat of burst-mode systems is that the optical components cannot sustain continuous operation and after each burst, typically a cool-down period of 10-20 seconds follows. Despite this, they are becoming increasingly popular since they offer unsurpassed temporal resolution, number of pulses and pulse energies. Other high-speed lasers are also available based on similar gain media, that offer up to 10-50 kHz repetition rates, albeit at much lower pulse energies. Nevertheless, they operate constantly, which might be more useful when studying time sensitive subjects.

When coherence and polarization are not particularly important, or in cases where the size of a full laser system is prohibitive, laser diodes and Light Emitting Diodes (LED) offer a practical alternative. In recent years ultrafast rise- and fall-time has been achieved in these solid-state light sources, allowing for their use in cases where pulsed light is required, while before their control could not be as responsive. Nowadays, LED's offer exposures even down to a few hundred nanoseconds, making them suitable for example, in Mie-scattering or shadowgraph imaging applications. The size of these systems is not bigger than a few square centimetres, allowing for easy installation and alignment, even in areas where it was not possible previously, due to size limitations or sensitivity to vibrations and harsh environments. Laser diodes can still offer high levels of coherence and polarisation but generally there is a trade-off between those parameters and power output. High-power laser diodes seem to lose coherence and the output wavelength tends to be broad, while fine emission line-width comes at the expense of lower power output.

3.4. Optical engines

Optical engines are engines that have been converted in some form to obtain optical access inside the combustion chamber and characterise the combustion behaviour. The degree of optical access necessary varies significantly depending on what needs to be investigated. In the simplest approach, a hole is drilled on the engine to provide access to a small borescope to give optical access to a camera or is coupled to a spectrometer to study the emission spectrum. In other cases, one of the valves is removed and in its place a glass insert is placed that allows a camera or a laser to look inside the combustion chamber. Other minimally intrusive techniques exist based on optical fibres to collect signal. A nice review article that outlines the history of optical engines and different variations can be found in [65]. Nevertheless, the most common conversion for research purposes, and the one that has been used for the work in this thesis, is done according to the Bowditch configuration [66]. In this configuration, the combustion chamber and the cylinder head are raised above the engine block, the piston is placed on an extension usually made from aluminium for lower weight, and a new liner is placed under the cylinder head. The liner is designed to be lowered and provide access for cleaning inside the engine. The piston extension is hollow to accommodate the placement of a mirror that provides optical access from underneath the cylinder, and through a transparent piston. A few example of this design are shown in Figure 3.3. The piston and the piston extension are mounted on the original piston and will perform the same reciprocating motion as normal. The rest of the pistons are drilled to release compression and weight is added on them, usually tungsten, to compensate for the increased mass of the transparent piston and the Bowditch extension. Otherwise, the engine block is usually kept as-stock.



Figure 3.3. Images from an optical engine converted according to the Bowditch design. In this case, drop-down liner is used, a flat-top piston and three liner windows are used to obtain lateral access inside the combustion chamber

Commonly, some form of optical element is incorporated in the liner to obtain lateral access inside the combustion chamber. Many variations exist, ranging from a transparent ring that encircles the whole combustion chamber, to small cut-outs that house windows. In the studies concerning this thesis, large windows were found on the heavy-duty engine used, that provided 30x55 mm access and have been utilised both, for imaging and for admission of a laser sheet. All optical components are usually made from fused silica, since it might be necessary to admit a UV laser light or capture the UV radiation from the emission spectrum of combustion, and normal glass absorbs the UV region. The same applies for the Bowditch mirror which is a glass surface coated with aluminium and should be UV-enhanced, to not filter any signal. Piston designs also vary greatly depending on the application, yet often a simplified geometry is used, with flat surfaces to mitigate distortions.

Nevertheless, incorporating so many optical components in an engine is a significant intervention that might affect the combustion behaviour. One important aspect is the much lower heat conductivity of glass or fused silica, which results in heat build-up inside the engine. As a result, the in-cylinder temperatures in continuous operation will far exceed what a fully-metal engine would experience under the same conditions. To combat this, a skip-fire mode of operation is implemented, where only some cycles are fired at a ratio of typically 1 fired to 10 skipped. Thus, heat can dissipate during the non-fired cycles to a level where it is representative of a metal engine. The exact ratio of fired-to-skipped cycles depends on the engine, engine load and the type of combustion, and some investigation is necessary to verify the correct ratio. One way would be to monitor the timing of the peak in heat release rate (HRR) and make sure it remains stable for the duration of the measurements. If the peak in HRR advances over time while all other factors are kept constant, it means that the accumulated heat inside the combustion chamber is raising and more skip-fire cycles should be used.

Another aspect is the reduction in the effective compression ratio, due to the increase of crevice volume. The compression rings in optical engines are moved much lower compared to metal pistons and are mounted on the Bowditch extension to avoid scraping on the interface with the liner windows. In addition, it is not possible to mount them on the glass and the periphery of the piston is often required to be transparent for lateral optical access. Additional liner clearance is also necessary to accommodate for the Bowditch extension, which commonly is 30-40 cm and results in greater lateral movement of the piston. The piston extension also deforms under operation and is compressed slightly due to the high cylinder pressure. Similarly, the squish height clearance needs to be greater, as the piston extension becomes elongated during the gas exchange stroke. In addition, the liner windows are slightly recessed for clearance and the result is much greater crevice volume in the whole combustion chamber. Nevertheless, a common strategy to combat this is to mindfully increase boost pressure and intake temperature to match the resulting conditions at Top-Dead-Centre (TDC).

4. Image processing and analysis

In this chapter, the discussion will focus on how to process image data to improve sensitivity and precision, correct for distorting agents, extract useful information and how to correlate images from multiple views. In addition, we discuss a few different techniques and tools that can visualise and intuitively communicate the information obtained from single-shot or time-resolved images .

4.1. Image processing

It is almost never the case that images obtained from the detector can be utilised directly without any post-processing. Raw images usually contain noise that needs to be considered as it interferes with the measurement. Optical distortions might be present and, depending on how they interfere with the measurement, might need to be addressed. In tomography for example, optical distortions must be compensated as they directly affect the quality of the reconstructed object. Optical engines use transparent pistons, often shaped to a certain geometry that introduces severe distortions and if an accurate representation of the imaged feature is necessary, the image needs to be corrected. Thus, a significant amount of processing is necessary to improve the measurement capabilities and provide more accurate information.

4.1.1. Noise and Background

In general terms, noise is the deviation of the measured signal from the real signal that the measurement is trying to capture. This can include external noise, such as interfering signals from sources other than the one we want to measure, or internal noise which would be introduced by the inability of the measurement technique to precisely capture the signal. Trying to record a singer's voice in a loud environment or trying to photograph the emission of a flame in broad daylight; in both cases there will be external signals that are interfering with the measurement. Following the same examples, internal noise could be distortion introduced by the microphone used to capture the voice of the singer, or in the case of a camera, grain-like noise which is commonly introduced by the camera sensor. In this chapter we will discuss both, with the convention that noise refers to the internal noise, which is introduced by the measurement, while the external noise will be referred to as background.

A common way of reducing noise on images is by applying smoothing filters, depending on what kind of noise needs to be suppressed. Image filtering is a somewhat counter-intuitive process however, since conventionally the drive is to increase resolution of the imaging sensors and obtain more precise information from what is imaged. Thus, smoothening an image should be avoided as it softens the image, reduces the resolution and some of the contained information is lost. While a variety of different filters can be applied, in this context we will mostly talk about spatial averaging filters and grain-noise reduction filters. An example that demonstrates the use of filters in images can be seen in Figure 4.1. A simple, low intensity (15% over background), stepwise transition is plotted along with a random noise pattern applied over the image, representing a case where some low intensity feature is imaged with a camera sensor that introduces noise. While our eyes are trained at detecting the transition, if a profile of the intensity across a line section of the image is plotted, it is impossible to distinguish where this step-up in intensity occurs. However, after a spatial averaging filter is applied, in this case a 5-pixel wide disk operator, the transition to the high intensity region becomes obvious. Plotting the signal across the same line section of the image clearly shows where the transition occurs. This is especially useful when edge detection algorithms are used to find the outline of features on an image, as filtering makes these intensity variations more visible. The drawback of such approach is that while the transition occurs within 1 pixel, after the filter is applied the transition becomes much wider, thus reducing precision in the spatial domain and effectively compromising the resolution. Nevertheless, filtering can be used to bring out features that we are interested in, then use them as a mask on the initial image to suppress background and maintain the original image in the regions of interest. This process is known as image segmentation and will be discussed in section 4.1.3.

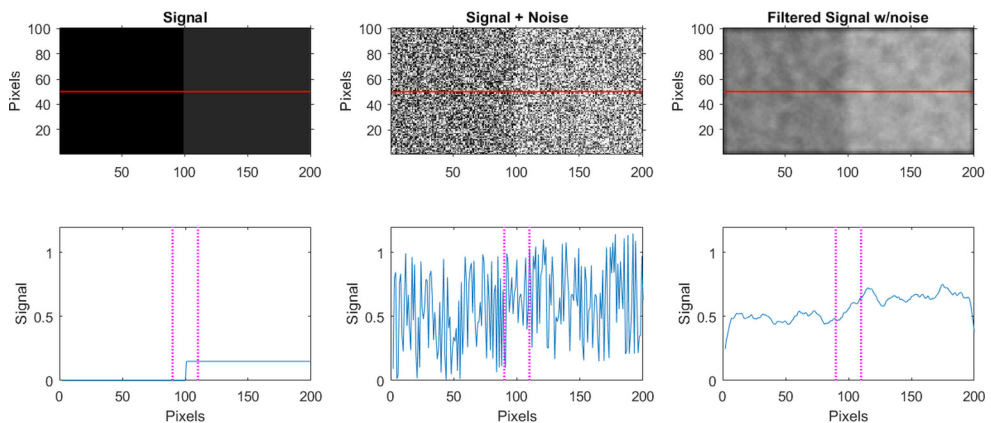


Figure 4.1. Example that demonstrates how filtering is useful in data with noise. The raw signal is shown on the left and some noise is introduced from our imaging sensor. Without filtering, the feature is lost within the noise as can be seen in the middle part of the figure. Taking a line profile of the intensity across the image reveals no perceivable transition, while doing the same process on the filtered image (right side of figure) clearly shows the step in intensity.

Multiple types of filters exist and ultimately, the choice depends on the objective and what features need to be enhanced or suppressed. A relatively less intrusive filter compared to the averaging filter mentioned before is the median filter, which excludes outliers, referring to data that is significantly different compared to their neighbouring. In an image sensor, this type of noise could be due to a bad pixel, essentially an unresponsive pixel, which is always at 0 or at maximum intensity. This type of noise is commonly referred to as salt-pepper noise as it appears either dark or white on an image and the median filter is ideal to exclude this type of noise from the final image. Other times, a high- or low-pass Gaussian filter can be applied to bring out features or reduce noise respectively. As an example, a single high-pass filter allows particle tracking techniques to be implemented on natural luminosity images as will be discussed in section 4.2.2, provided that the filter size is matched to the size of the flame features.

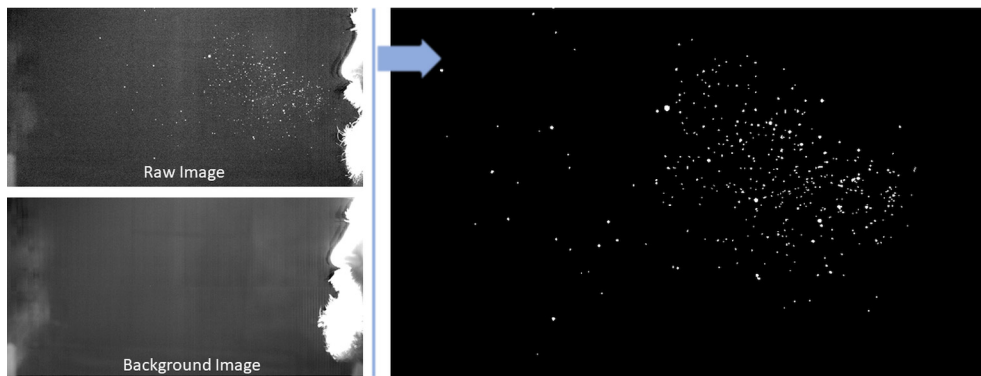


Figure 4.2. Illustration of the background suppression and the resulting image. The inhomogeneous background in the raw image is removed by subtracting an average image of multiple frames recorded, without any of the features of interest present. Subsequently, a filter is applied to reduce the noise and the desired features become apparent.

As discussed earlier, an important step in improving the measurement's precision is suppressing the background contribution. This can be involuntary light reflections or any light from unwanted sources that interferes with the measurement. One example is shown in Figure 4.2, from the experiments in Paper I (section 5.1), where stray light is present despite best efforts to eliminate it during the experiments. The camera sensor has captured the line-of-sight integrated signal that consists of the particles that need to be imaged along with the scattered stray light. Nevertheless, the background contribution is relatively consistent across the image sequences and the different cases that were studied during the experiment for each participant. Thus, several randomly selected images can be used to create an average image that manages to capture the inhomogeneous profile of the unwanted stray light. Subtracting this background image from the data provides a flat background field where other processing steps can follow in order to characterise the system. Since the signal captured by the sensor is line-of-sight integrated, it will consist of both

the feature and the background, thus subtracting the background must not affect the feature that needs to be imaged. Since signal and background are convoluted, there could be areas where the sum of high signal and low background might have lower intensity than areas with low signal and high background. Thus, simply introducing a global intensity threshold, capable of suppressing the background, would also remove a lot of the actual signal captured. However, after a flat background is achieved, a global intensity threshold becomes meaningful and can be applied to increase contrast and reveal the correct signal.

It is important to note that the background subtraction method mostly applies for line-of-sight integrated signals with transparent media. When the imaged feature is opaque, it traps the signal originating behind it and thus a background subtraction will only reduce the true signal of the feature, thus introducing error rather than improving the precision of the measurement. Such a case would be in Mie-scattering of sprays, where global illumination is used; once the sprays appear, the background contribution is lost as the sprays scatter light and become opaque. Similarly, when laser sheet imaging is employed, the feature is ahead of the background and becomes the predominant signal, so a background subtraction will only manipulate the signal. In cases where there are laser reflections and unwanted fluorescence at the sheet plane, we can proceed to subtract those contributions, however, such features should be avoided proactively. In sheet imaging, it might be necessary to compensate for an inhomogeneous laser profile, which is a similar process to background subtraction, only applied according to the sheet intensity distribution.

4.1.2. Image Undistortion

Another important aspect of raw data pre-processing is corrections for distortions that occur, either from the imaging system itself, or from the optical elements that the signal passes through before reaching the detector. The imaging system itself is rarely the primary concern as distortions are minimal, unless a very wide-angle lens is used which introduces severe distortions. Some applications, such as tomography and droplet sizing techniques, are very sensitive to any type of distortions and in most cases special lenses need to be used (telecentric) or the image distortion field needs to be characterised and compensated. Nevertheless, in most imaging applications distortions introduced by the imaging system are not as significant as the ones introduced because of the compromised optical access. Since most of the work in this thesis has focused on optical engines, the discussion will focus on distortions from optical components commonly used in such applications. Predominantly, there are two main optical elements used, the liner windows and the optical piston. While many liner windows styles exist, most commonly they follow the curvature of the cylinder bore on their inner surface to keep crevice volumes within the cylinder as little as possible, and are flat on their outer surface for easier clamping and securing on the engine. This results in them acting as thick, strongly

diverging, plano-concave lenses, with a focal distance approximately equal to the cylinder bore diameter. The transparent piston on the other hand has much greater flexibility and variability when it comes to the design. Some optical pistons are flat in order to minimise any distortions and are mostly used to preserve a high compression ratio. Even though the top part of the piston is flat, the bottom part might be curved to increase the effective field-of-view. In other cases, the design of the piston requires it to be identical or similar to some geometry from a stock engine or another design that needs to interact with the sprays and combustion in a certain way. For example, diesel pistons benefit from having a bowl-shaped piston top to contain the fuel and minimise heat losses, with various geometries regarding the top-land region, the bowl-wall, and the pip at the centre. The top-land might be angled or have a stepped-edge design, the bowl wall might be curved and the pip at the centre might also be curved or stepped. In addition, in order to reduce load, cyclic fatigue or thermal stress concentration, the design and manufacturing of the piston might require certain radius chamfers introduced. A transparent piston with all these requirements leads to light refraction, focusing and severe distortions introduced in the measurement. Some examples of such distortions can be seen in Figure 4.3. In the Bowditch configuration, a third distortion element is the angled mirror, which usually is not a concern as it sits at 45° . However, the camera is not necessarily looking straight into the Bowditch mirror but might be slightly angled, which would result in a tilt or perspective shift of the image. Other times it is necessary for a camera to view the Bowditch mirror through an additional angled mirror, as in the activities described in sections 5.2 and 5.3, in which case some tilt distortion will most certainly be introduced.

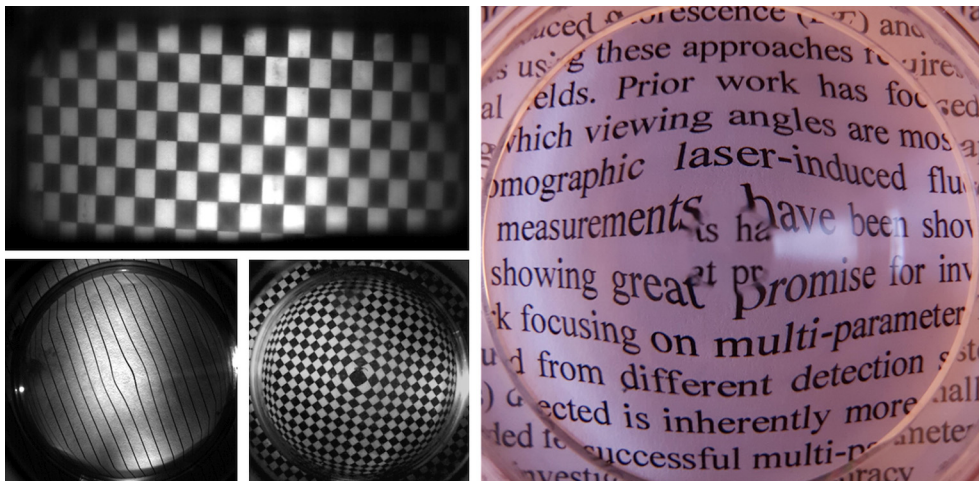


Figure 4.3. Examples of distortions introduced by optical engine components. The top left image shows a checkerboard image through a liner window, while the other images show distortions from transparent pistons.

In order to extract useful information from the imaged features, it might be necessary to compensate for the distortions introduced by the optical components. This process is called undistortion and most commonly relies on characterised target images that consist of patterns and features with well-known physical sizes. Checkerboard patterns, a series of lines or concentric circles, a grid of dots are a few examples of target images. The most commonly used in this work has been a checkerboard pattern with a box size of 3 mm since it can capture the distortions and at the same time provide a real-world length scale to derive the image ratio of the imaging system (pixels/mm or mm/pixel). The location of the box corners can be easily recognised, either manually by the operator or from algorithms such as the Harris-features detector [67] commonly used by Matlab® among others. The position of the corners in the undistorted target is a known physical property that is then compared to the detected points on the distorted target and thus, the distortion field is visualised and characterised. Subsequently, the inverse transformation can be derived and applied to the images to correct for the distortion. However, it is quite common that the distortions from optical engine components are too severe and the Matlab® built-in routines for image undistortion either fail to detect the corner points or the detected points are too far from the expected values. In other cases, the distortion field is discrete with abrupt changes, which is quite common in bowl-shaped pistons, and are difficult to characterise with a single function.

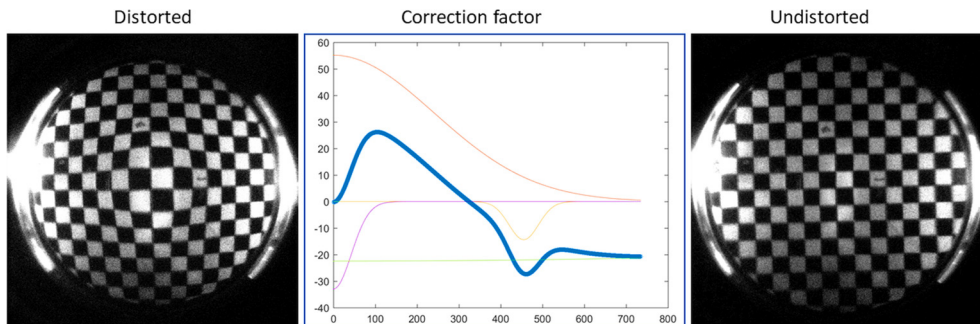


Figure 4.4. Example of the undistortion procedure for a bowl shaped piston. In this case, radially symmetric distortions such as the ones from a bowl-shaped piston, can be corrected by convoluting the position of pixels with a sum of Gaussian curves that redistributes the pixels in the undistorted position.

Since piston distortions are usually radially symmetric, a facile way of correcting the distortion field is to radially redistribute the pixels according to a correction function. An example of this process is shown in Figure 4.4, where the correction factor is shown. The coordinate system is switched to polar coordinates with very high fidelity and then the correction function operates across a line, so 1-dimensional rather than 2-dimensional. Then the complex distortion field can be characterised by a sum of Gaussian curves of different magnitudes and widths that radially redistribute the pixels to the correct distance. The added benefit of this method is that the radius range where the correction factor operates can be

discretised, thus it is possible to selectively apply the correction to certain circular bands of the image and leave others intact. Subsequently, the undistorted image is returned to a Cartesian coordinate system for further processing and analysis.

4.1.3. Image Segmentation

Having corrected the raw images in terms of background correction and distorting agents, often we need to isolate certain features or regions from the images. In image processing, this process is called image segmentation and as the name would imply, it means to divide the image in separate parts with certain properties. The segmentation of the features can be done with a variety of criteria, like intensity, area covered, length, eccentricity, shape, or a combination of some of these factors. Usually, the process starts with setting an appropriate intensity threshold to separate the features from the background or maybe we are mostly interested in the high intensity features. Then, the size criterion might be of interest and regions that are small, large, or within a range of area covered can be selected. Other times the selection is based on location and we can select a region-of-interest within which to operate. The selection can also be done manually if the feature we are looking for is particularly erratic or if the number of images is small.

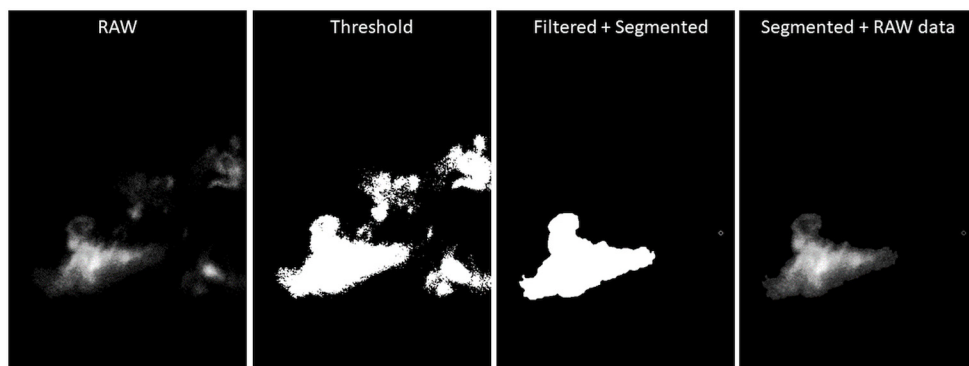


Figure 4.5. Illustration of the steps involved in segmenting the image and isolating the feature of interest. In this case the selection of the area is done manually as properties like the shape and size are not constant.

An example of the segmentation process is shown in Figure 4.5, from the experiments described in section 5.3. The feature is fluorescence from partially oxidised fuel, and due to the laser sheet used to excite it being wider than the feature itself, other neighbouring regions are captured too. After applying an intensity threshold, the image becomes binarised and all features are isolated as individual areas. At this step, one could simply select the largest area, however in this case the feature of interest is not consistently the largest feature for all the sample images. In this particular application, the selection was performed manually as the sample set

was not too big and the nature of the feature was erratic. Subsequently, a filtering step follows to clear the borders of the region, along with an erosion step to reduce the dimensions back to the original feature size. Finally, having derived an outline that we are confident in, the original intensity values can be applied on this binary image and thus, the feature is isolated from the rest and retains the original qualities.

4.1.4. Image Registration

Commonly in optical and laser diagnostics, the requirement is to visualise two or more features simultaneously. This is usually because these features are in some form co-dependent and we want to analyse their relation, a prime example being the hydroxyl radical, OH, and formaldehyde, CH₂O. These intermediate species are used as markers for different reactions taking place in the oxidation process of the primary hydrocarbon that was used as fuel. In particular, CH₂O is used to visualise where the chemical reactions have started and OH is used as an indicator of a flame front or where the high-temperature reactions are taking place. In the case of Paper II, explained in section 5.2, natural luminosity and fuel-tracer LIF were used simultaneously to investigate the correlation between fuel concentration and combustion development. In Paper V, described in section 5.3, natural luminosity and CH₂O LIF were used to investigate a flame extinction phenomenon in multiple injection strategies. In order to perform such measurements, usually one detector is required for each feature we need to visualise, and the images obtained need to be spatially correlated. The process of combining or correlating multiple views is known in the image analysis field as image registration. Quite commonly this refers to a recording from a moving camera, where features of an image need to be matched among the frames and a stitching process combines them in a panoramic view. In other cases, images of a feature like a statue, are captured from multiple views and are used to perform a reconstruction of the feature in three-dimensional space. In this chapter however, we will focus on the process of spatially overlapping two images from two different cameras imaging two different features.

In order to achieve a successful registration, first we need to discover the differences in image ratio (pixels/mm) and the translational, rotational, perspective (tilting) shifts and inversions (mirroring) that might be applying between the two views. Initially, the checkerboard pattern image discussed earlier that is used to obtain the distortion field is imaged in both views. This allows us to obtain the image ratio for each camera since the box size is known. This time however, the target image should have one or more points or features that can be cross-referenced between the two views in order to obtain the other correlation factors. A simple off-centre mark on the target is enough to show rotation and translation but cannot distinguish mirror inversions without prior knowledge of the setup. In papers II (section 5.2) and V (section 5.3) for example, an extra mirror is used for one of the cameras to view through, resulting in an inversion of the image around a certain axis. Already

knowing this, it would be possible to include this inversion in the post-processing routine, however, it is always good practice to treat the data as a black box and not have any predetermined bias. Thus, a second point that would form an asymmetric structure in conjunction with the background or the addition of a letter is necessary. Alternatively, a letter or shape alone, without any symmetry, should be used on the target to capture the correlation. Some examples of appropriate letters could be F, G, J, L, P, R, etc. since they cannot be mistaken when mirrored, while A, B, C, D, E, H, I, etc. should be avoided as they have at least one axis of symmetry, meaning that they could be mistaken when mirrored and rotated by 180° .

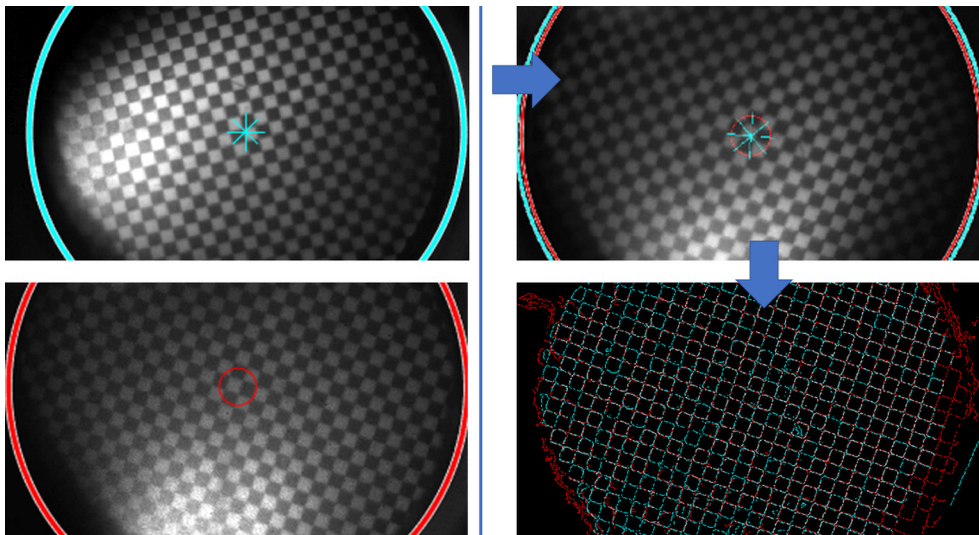


Figure 4.6. Illustration of the calibration process for registering two camera views. The circular piston extension is used as a reference where a circle can be fitted and the centre of this circle is used as the centre of the image. The final image is used to evaluate the quality of the overlap, where the edges of the boxes are used to visualise mismatches.

Having discovered the geometric relation between the two views, we can iteratively apply the necessary processing steps in one of the two views, or on both depending on the distortions present, until the registration is successful. These processing steps include inversion, rotation, translation, and down- or up-scaling to match the image ratios. It is worth mentioning here that distortion corrections should be applied before the registration process, as without accounting for them the correlation is impossible to assess. In the case of Figure 4.6, the process of verifying the result and evaluating the quality of the registration is shown. A feature that is common in both images is found, in this case the base that supports the piston on the piston extension. This is visible in both images as it limits the effective field-of-view inside the combustion chamber for both cameras. An equivalent diameter circle is fitted at that location for both images and the centres of those circles are plotted in the same frame. The circle diameter is not important as the ultimate goal is only to obtain the

coordinates of the centre of the piston. After the necessary image processing is performed, the two points should overlap as the purpose is to achieve a perfect overlay of two images. Having succeeded in matching the centres does not ensure that the image ratios are correct and thus, the checkerboard pattern is used next to assess the overlay across the entire image. Instead of the actual images, the gradient images or other edge detection algorithms are used, to visualise the transitions between black and white neighbouring boxes. Now the transformed images are binary, consisting only of lines at the box edges, thus making the images easier to assess. If the original intensity values were preserved, an error in the registration by a few pixels would be very hard to visually perceive since it would only result in less defined box edges, while with a grid consisting of 1-pixel wide lines, even a 1-pixel stand-off is visible in this false-colour overlay. When the borders overlap, the match is perfect and is shown in white, while when they don't overlap their respective colours appear. Since the two detectors have different light sensitivity and different viewing geometry, the edge detection will not perform equally across the whole frame and consequently the borders cannot be expected to correlate perfectly. Nevertheless, it is possible to understand the quality of the overlap even without a pixel-to-pixel correspondence. Having the image centres matched and the borders predominantly overlapped, the registration can be considered successful.

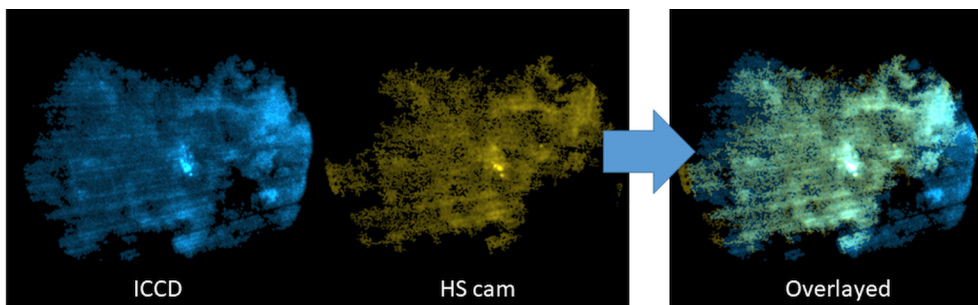


Figure 4.7. Example of raw data from the activity described in section 5.2.1 showing the resulting overlaying. In this case the entire imaged feature was present in both views and thus we can evaluate the result on the real data.

With the calibration now performed, the images containing the experimental data can be overlaid, and the features in them can be correlated. However, it is crucial to ensure that the detectors and engine hardware do not move relative to each other, as that would result in a new system that the calibration is not valid for. In real-world measurements though, it is quite common that the signal we are trying to capture moves in relation to the detectors, such as an optical engine where its operating position will differ slightly to the stationary one upon which the calibration is based on. Nevertheless, small translational shifts are the least problematic and can be compensated for, if the new relative position is known. For this reason, it is always beneficial if some feature can be traced in both views as that will provide a checkpoint that can be used to monitor and compensate for

movement. In optical engines that can be an injector, a valve or some other circular feature like the piston bowl, etc. that can provide at least one set of coordinates to be used as reference for the two images. This case is discussed further in section 5.3, where the injector tip location was used as a checkpoint. In other cases, like the one in Figure 4.7 (with data from section 5.2.1), the entire captured feature is used, as it is picked up by both detectors. The intensity values might be totally different, but the feature is predominantly the same and the spatial overlap can be evaluated. In addition to the translational shifts, another significant concern is the movement of the piston itself. If the shape of the piston causes significant distortions and the imaging technique is line-of-sight integrated, the distortion field changes with piston position and even a position-based undistortion will not be capable of compensating for the distortion field. The reason for this is further explained in section 5.3 and it is because we cannot know where the signal originates from, relative to the piston.

4.2. Image analysis

Having discussed how to prepare the images, in this chapter, let's discuss image analysis which is the process of extracting useful information from them. Usually, images will have features that we want to evaluate over a number of samples or how they vary over time in an image sequence. Such features can be number of separate regions, along with the area they cover, variations in size within the same image or other physical sizes like length, eccentricity, centroid to name a few. In other cases, we might be more interested in intensity or intensity variations of the features of interest. These parameters can be measured regardless of whether the images are from a time sequence or from separate events. Often, a periodic phenomenon is studied and due to hardware limitations, only one sample image can be obtained per period. When the timing is the same every period, the most common representation of this sample set of individual images is the average image, or a probability density function to show variations in these periodic events. In time resolved sequences however, the entire investigated effect needs to be captured, thus the whole process needs to be somehow analysed and communicated. Rather than simply describing in writing and showing a sample set of images which can be hard for the reader to perceive, mathematical tools have been developed and are also discussed in this section that allow for an intuitive communication of the temporal variations in dynamic phenomena.

4.2.1. Individual or single-shot images

On temporally uncorrelated images, after the post-processing is performed as shown in chapter 4.1, the features of interest are already corrected for aberrations, segmented and referenced in real-world coordinates at as high precision as the

experimental setup allows. Now the analysis of the images revolves around the physical properties of the segmented features like size, shape, intensity, number of individual areas and their relative position. Regarding intensity measurements, a discussion can be found in section 3.2, where the quantum yield and the spectral response of the detectors are discussed. These are important parameters when accurate intensity measurements are required, however, such applications were not investigated in the work involved in this thesis and will not be discussed further. When it comes to sizes, area and relative position, all measurements are performed in pixels and the image ratio should be known in order to return to millimetres or other length scales. Some commonly studied parameters are length, shape uniformities like roundness, eccentricity or irregularities, area covered either by isolated features or average area of all features within the frame. An example of these properties is shown in Figure 4.8, where the area of the individual areas is measured along with the perimeter. In this case the images are from a time-resolved sequence, but the measured properties are global and specific to each individual image, so this example is only used as an illustration of the whole process from raw images, to measured quantities. A more in-depth discussion regarding the derived data from these images can be found in section 5.3.

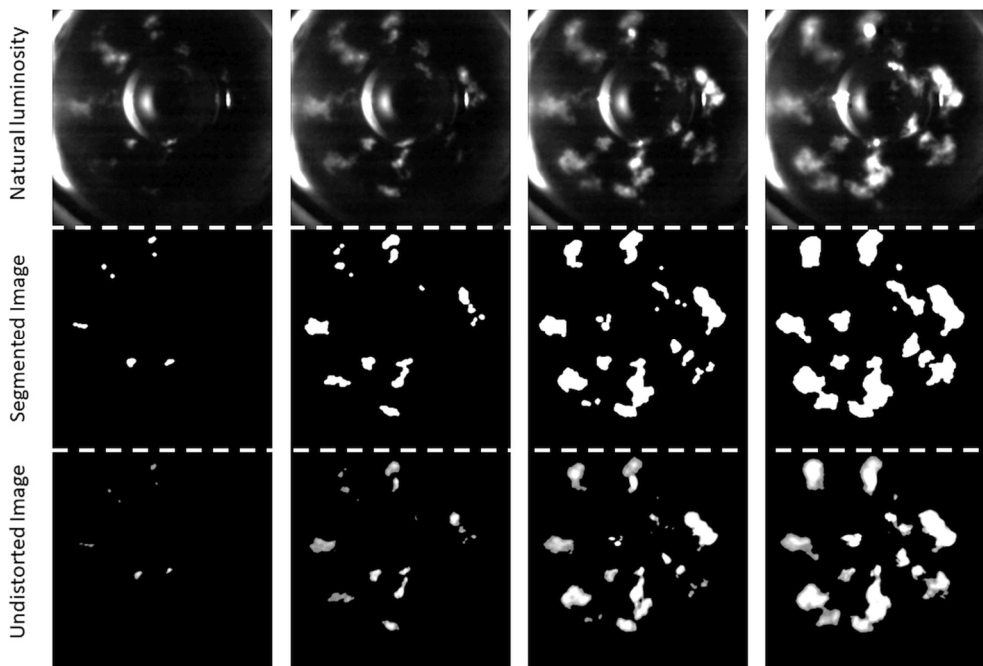


Figure 4.8. The raw data showing four frames from the evolution of combustion are shown at the top, along with the segmented features with reflections and the background contribution removed in the middle row. The bottom row shows the original intensity values reintroduced and the distortion field compensated.

It is rarely the case that an effect we are trying to analyse is captured only once, but rather multiple times since we need to understand if our measurement is consistent and repeatable. However, most phenomena in nature are dynamic and unpredictable to a certain degree, thus, while trying to characterise the same process with multiple measurements, minor variations are to be expected. This applies to a great degree in combustion and spray studies where multiple competing mechanisms are present. For example, the injection process in an engine depends greatly on a number of parameters, such as ambient pressure and temperature, injection pressure, fuel density, etc. and minor fluctuations in these parameters can affect the final result. Similarly, in combustion, temperature and fuel concentration variations greatly affect the combustion propagation or the chemistry involved in the auto-ignition of fuels. These variations in the combustion engine field are named cyclic variations or cycle-to-cycle variations, as an engine is expected to operate similarly from one combustion cycle to the next and deliver a smooth and predictable work output.

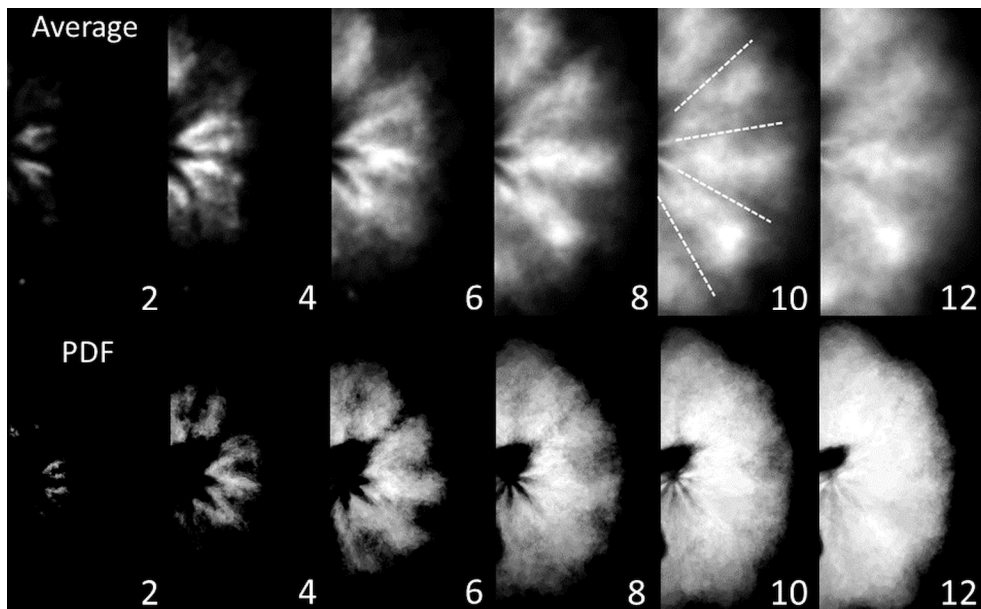


Figure 4.9. The average combustion images are compared with the PDF-derived images. The intensity of the PDF images corresponds only to the probability of the flame being present.

Nevertheless, it is common practice to average across multiple measurements to obtain a well-sampled view of the system and the quantities we are analysing. The average image can reveal the most probable location along with some vague indication of the variation of the imaged features. Yet, an average image over few samples is easily biased by large variations both in terms of location and intensity. In addition, the accumulated signal on the average image is ambiguous to intensity and the appearance frequency of the feature at the same location, meaning that it is

unknown if the feature is present multiple times at the same location or if it exhibits higher intensity at that specific location. In such cases, the probability density function (PDF) is ideal as it is not biased by the intensity and relies solely on the location of the feature. An example of this is seen in Figure 4.9, where average combustion images are shown, along with the corresponding PDF-derived images. The PDF images are created by using the combustion images without the intensity information, or as binary. Averaging the binary images across multiple cycles results in an intensity variation stemming from the flame presence alone and subsequently a confidence interval can be applied to select the most probable flame locations. In this example the confidence interval was set to 80% and managed to illustrate the behaviour of methanol spray-driven combustion. The white dotted lines in frame 10 indicate the integrated signal being much lower along the spray axes and it was not known if this is due to lower intensity along those axes or less frequent flame appearance. Comparing the early frames, they appear very similar in intensity distribution in both, the mean and the PDF image, meaning the flame is less frequently present across the jet axes. For later frames however, the PDF image becomes more uniform while the average image still exhibits lower intensity along the spray jet axes which lead to the conclusion that the line-of-sight integrated signal is lower across the centreline of the spray jets. A more detailed discussion on this subject is found in section 5.2.1.

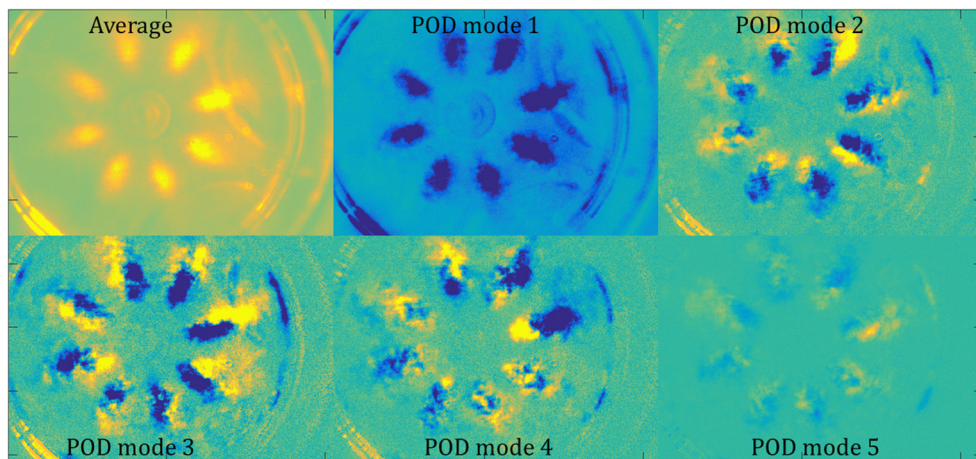


Figure 4.10. The first five modes from a POD modal analysis of 50 fuel distribution LIF images is shown, along with the average image of the same dataset to illustrate the differences.

Another very useful tool in determining the variations in image datasets is Proper Orthogonal Decomposition (POD). POD is very similar to Principal Component Analysis (PCA) and Singular Value Decomposition (SVD) techniques and can be applied to any arbitrary dataset. All these techniques have a similar goal, which is to decompose the dataset into a minimal number of basis functions which are

referred modes, that contain as much energy as possible. Originally, POD was introduced by Lumley in 1967 to extract coherent structures in flow data from turbulent flow fields, and since it has traditionally been used in PIV data to extract the prominent features of the flow. Nevertheless, the method can be applied to any arbitrary dataset, and as such image set can also be analysed. However, the physical interpretation of the outcome is the important aspect, and in images what can be derived is a decomposition of how the pixel values vary within the dataset. Let's assume we obtained 50 LIF images from the fuel distribution inside the combustion chamber, at the same timing, with a resolution of 100x100 (for simplicity). The images can be converted to linear vectors and the sample set of 50 is stacked in a matrix X ($m \times n$), that will be $m=10000$ and $n=50$. These images are independent samples of the fuel distribution of different cycles and will of course be slightly different because of cyclic variations and turbulence. The average image is then subtracted from the set of images, as we want to study only the variations in the data. While this is not necessary, it does affect the interpretation of the data. Nevertheless, with the average subtracted, POD can derive the variations in our dataset that are consistent and recurring, and rank them according to how frequently they occur. This is performed by calculating the SVD of matrix X to give,

$$X = U \Sigma V^* \quad (4.1)$$

Where U ($m \times n$) has orthonormal columns, Σ ($n \times n$) is a diagonal matrix, and V ($n \times n$) has orthonormal columns, and the asterisk shows that it is the complex conjugate transpose. For brevity, U is the correlation matrix XX^* which is a measure of similarity between the rows of X , matrix V is the eigenvectors of X^*X and thus indicates similarity between the columns of X , and finally Σ holds the singular values of matrix X , or the square roots of the non-zero eigenvalues of both XX^* and X^*X . The columns of U are the POD modes and capture the energy of the system, where the first mode will be the spatial structure that optimally captures the system energy with one vector, the second mode with two orthogonal vectors, etc. Thus, the coupling of the system is mixed in the POD modes that we have derived. An example of the results from this analysis can be seen in Figure 4.10, where indeed the variation of the data in 50 LIF images that capture the fuel distribution is decomposed and the first five POD modes are shown, together with the average image. The first POD mode depicts the most prominent spatial intensity variation, the second will be the second most prominent and so on. It is important to note that the intensity variations of each spatial structure are co-dependent, meaning that a region of high intensity will coincide with the lack of intensity in other regions within the same image. In this case, knowing that it is fuel distribution data, within the same mode, a lack of fuel in a certain region results in the appearance of the fuel in another location. This is a great tool to visualise the cyclic variations of the data when sampling single-shot images and provides a visual aid that illustrates the exact pattern of these variations. Commonly, only the first 2 to 5 modes are enough to

describe the whole system. More thorough mathematical formulations and explanation of the method can be found in [68-71].

4.2.2. Image sequences

Usually, it is difficult to communicate the effects that are taking place throughout an image sequence and usually a few snapshots or a series of images is shown, and the effect is then analysed in writing form to convey the message to the reader. In this section a few ways of presenting time-resolved data will be shown.

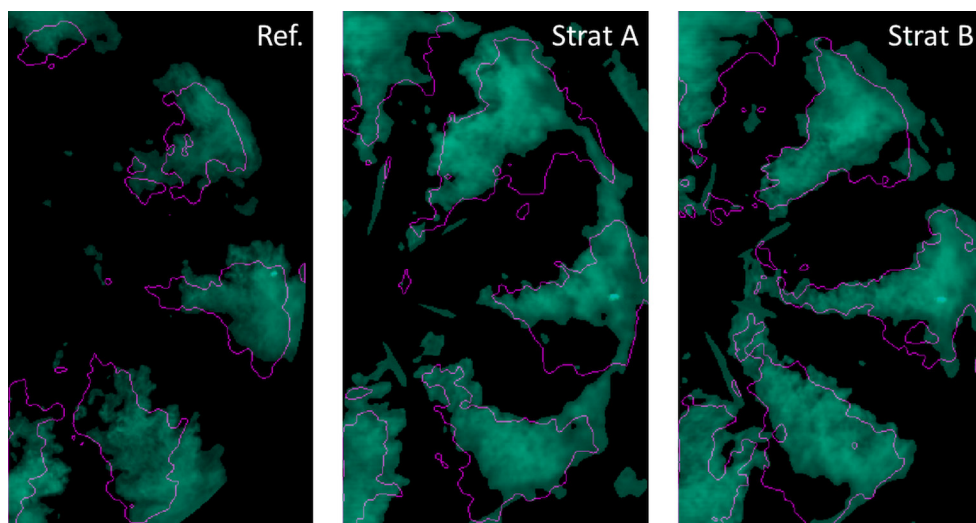


Figure 4.11. Comparing three different injection strategies by overlaying a predating frame (purple outline) and another from later in the image sequence (green regions), the progression of combustion can be visualised. In this case part of the pilot flame is extinguished due to a subsequent injection in the middle and right images.

One way of showing spatial changes in images is by overlaying early frames with subsequent. One example of this is shown in Figure 4.11, where a flame extinction effect is demonstrated for three different injection strategies discussed in section 5.3. A series of images for three different events would occupy one full page of an article, and small variations in flame shape are not easy for the reader to distinguish, unless the whole video sequence is shown. However, by overlaying two frames at the timings where the effect is observed, it is enough to notice the shift, or lack thereof, in the pattern. A certain amount of post-processing is required however to best illustrate the effect, since simply adding the two images would create an average image of the two. For this reason, it is best to use just the outline of one of the two images, which reveals the outer border of the feature, and overlay it with the other image. This process is handy when significant changes in the spatial features need to be shown.

Another process that is capable of communicating smaller changes in image sequences is the use of cross-correlation algorithms to detect pattern motions in consecutive images. The process is identical to the one used in PIV techniques, where the pattern of particles seeded in a flow is monitored, and the relative motion of the particles is tracked to obtain a visual representation of the flow. Two images are obtained and are split in small sections, called interrogation windows, where within them a unique pattern of particles exists. The unique pattern within the interrogation windows is then cross-correlated and matched between the image pair, thus the displacement of the group of particles can be measured. The result is that each interrogation window can define a vector with known direction and magnitude and the flow can be characterised. The application of such techniques in natural flame luminosity images is known as Combustion Image Velocimetry (CIV) or Flame Image Velocimetry (FIV). Similar work can be found in [72-74]. In the case presented in Figure 4.12, a simple 5-pixel wide, high-pass filter is used on an image pair from a sooty diesel flame. The result of this process brings out the high intensity features within this 5-pixels wide filter, and the image reveals many unique particle-like features, which can be tracked between the two images. The image is split in interrogation windows and the cross-correlation can then be applied, in the same way the process is done in PIV analysis. The result is a vector field that can clearly relay the motion that is taking place inside the combustion chamber. However, the vectors derived reveal the motion across the image plane while the signal received is a line-of-sight integrated signal from the whole chamber. Thus, the exact motion of the flame features cannot be accurately resolved and is only approximate. Nevertheless, the method does relay everything that the observer can see with their own eyes and is therefore a useful tool in showing the motion across the image pair.

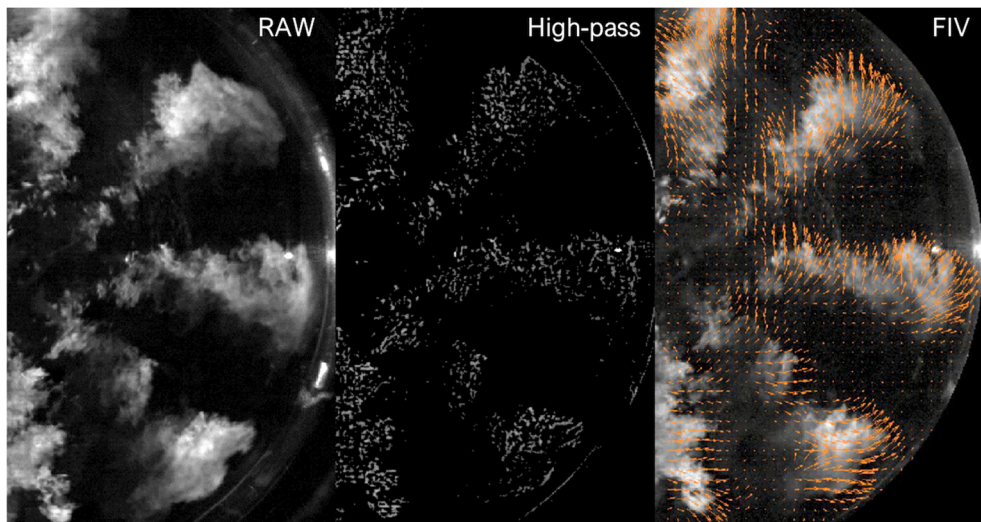


Figure 4.12. Illustration of the Flame Image Velocimetry technique. After a high-pass filter is applied on the raw data, the texture of the flame is revealed and is used as seeding for particle tracking across the frames of the image sequence.

Last, another method of modal decomposition is the Dynamic Mode Decomposition (DMD) [70, 71, 75-77]. The method is very similar to the POD and is once again solved by solving the SVD for the same data matrix X . However, this time the data that is used is from a time-resolved image sequence of a continuous event, and the temporal variations are decomposed. The average image is not subtracted from the data this time, as the images are from a sequence and the variations of the imaged feature need to be illustrated. Essentially, we assume a linear relationship between the dataset X , which is all the images from the sequence stacked, and a dataset X' , which is the same dataset only shifted by one image. Essentially, we are comparing subsequent images to obtain the temporal variation of the feature we are investigating. An example of the DMD applied on an image sequence of a spray is shown in Figure 4.13 where again the features present on each mode are co-dependent in magnitude. In this case the fluctuations of the liquid spray body can be seen to oscillate. The DMD analysis can even quantitatively reveal the frequency at which the oscillation occurs.

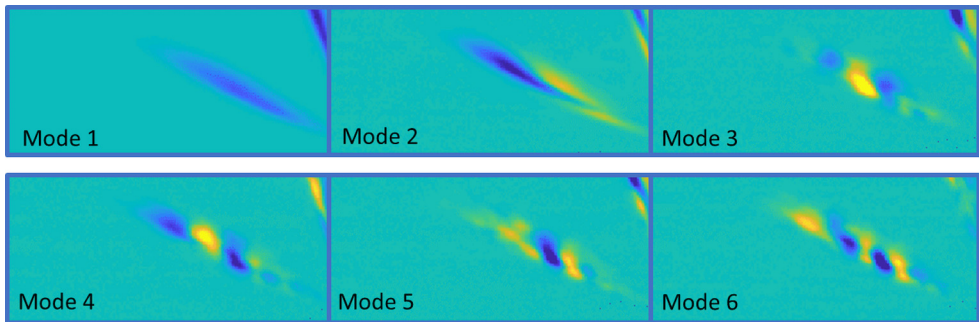


Figure 4.13. The first six modes from the DMD analysis of a spray plume are shown.

5. Results

In this section, both published and unpublished results will be discussed in detail. Utilizing all the techniques and processes mentioned earlier in this thesis, the discussion will include the initial research questions that launched the experiment, the design of experiment and the results obtained. In addition, some experimental considerations and tips will be mentioned in order to make the experimental setup easier and more versatile in alternating conditions and demands.

5.1. Exhaled respiratory particles

In this experiment, the goal was to visualise the exhaled particles from people under various conditions, such as breathing, talking, singing, wearing a mask and at various tones and volumes. The participants of the study were given a simple, consonant rich verse to voice in constant tonality for each case, in order to separate variations due to tonality and volume. The cases investigated were talking, talking loudly, singing and singing loud in two tonalities, singing with exaggerated diction and finally singing loud with exaggerated diction while wearing a mask. The verse was repeated twice for the high-speed camera measurement as the memory filled after 22 seconds of recording. Before performing the actual experiment however, some initial screening tests were necessary as we had not performed anything similar in the past. Yet, the process is similar to studying spray systems since the goal is to visualise liquid droplets. The main difference is their size and number, as when visualising fuel droplets, their number is usually extremely high and they cannot be individually resolved. From previous studies [56, 78], the size of exhaled particles ranges from submicron to a few hundreds of microns.

There are a few ways to optically visualise particles and liquid droplets, mainly shadowgraphs and scattering experiments. In shadowgraph techniques, the shadow of particles passing in front of a bright background screen is imaged. In this case, detection is limited by the optical resolution of the imaging system, as there is direct correspondence between real world dimensions and pixels on the detector, known as the image ratio. In optical systems, there is a trade-off between field-of-view (FOV) and optical resolution, thus a large FOV means that small features will not be resolved by the detector. In elastic light scattering, the detected signal ultimately depends on droplet size and the geometry of the system, mainly the power and the

incident angle between the light source and the particle. Depending on the size of the particle, different incident angles of light can be scattered more effectively towards certain directions. Droplet size is also important as the larger the droplets, the higher the scattering power. Additionally, a more powerful light source will result in higher scattered signal from the droplets, irrespective of size. Thus, in scattering, detection is not as limited by the optical resolution of the imaging system, but rather depends on design of the light source and geometry of the imaging layout. In addition, since the desired FOV for this experiment was large (~50cm), the preferred choice was to detect the particles through their scattering properties.

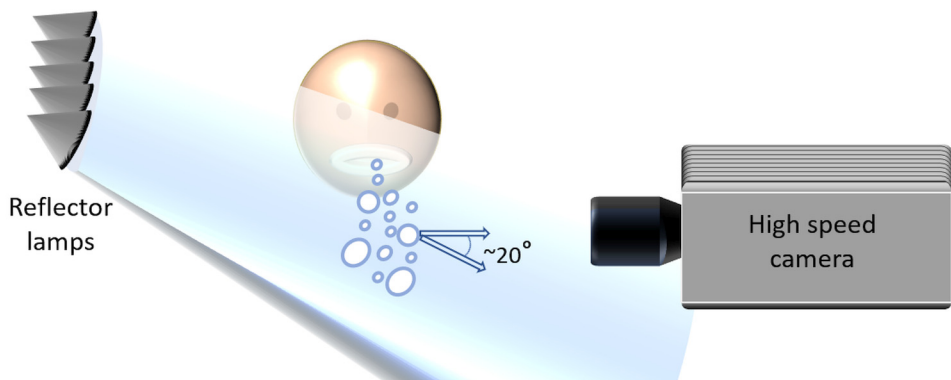


Figure 5.1. Illustration of the experimental setup for the detection of exhaled respiratory particles. The light was aimed approximately 20° off the horizontal plane of the camera to utilise the forward-direction scattering properties of smaller droplets and improve detection sensitivity.

In screening studies performed before the experiment, a laser diode light source was initially used with a diverging lens, creating a diverging, sheet-like light profile. The power output of the laser diode was 2 Watt and emitted in a wavelength of 452 nm, since this is commonly used in liquid spray imaging. The results showed that a more powerful light source would be beneficial as detection kept improving all the way to the maximum power output of the laser diode and additionally the detected particles tended to flicker. Flickering is an indicator that the particle is going in and out of a favourable incident angle for scattering. Additionally, when inexperienced users are involved, as the participants in this study, working with laser light needs a lot of precautionary measures like warning lights, shielding, laser goggles, safety briefing, etc.

In order to derive a powerful working setup within reasonable time, conventional, incandescent narrow spread-angle reflector lamps were used. In addition to having a lot of power and being scalable, these lamps reflect light off the centrally located light bulb towards multiple angles, collectively however, rated at 10° of divergence. This provides multiple incident angles that the particles can scatter towards the detector, thus providing a wider emission which in turn reduces flickering that

occurs with unidirectional light. In order to achieve the highest possible sensitivity, ten 50 Watt reflector lamps were used in two arrays of five, positioned offset and at an angle between them. The angle between them was determined so as the light path would intersect at a distance of approximately 1 meter, where the desired area is imaged. This 500 Watt light source was positioned so as the illumination would arrive at approximately 20° off of the horizontal plane of the camera. Given the complexity of the illumination pattern, only approximate angles are quoted. However, the goal of this lighting arrangement was to utilise the forward scattering properties of particles smaller than $1\ \mu\text{m}$, which scatter more effectively in a range of 0 to 45° off the incidence angle. A factor that limits this angle is the placement of the camera, where it needs to be as close as possible to improve signal and detection efficiency, while providing the required FOV and not be dazzled by the light source. The experiment took place inside an airtight, controlled environment chamber to minimise the contribution of ambient airborne particles like dust, fibres, etc. The ventilation of the chamber was constantly running to reduce the particle count, frequent cleaning of floors and walls was carried out and people entering the chamber wore surgical clothes to minimise introduction of new particles. As a result, background particles detected by the camera were measured at 5-10 across each frame of the background sequence. This result was satisfactory, given that the presence of three people was necessary in the chamber to run the experiment.

The raw images already reveal many particles, however, mostly the large droplets are visible initially as they emit stronger. Nevertheless, smaller droplets also scatter light and are captured in the lower intensity range of the detector. Subtracting a background image, without the contribution of particles, improves the contrast ratio and allows for a more consistent determination of what consists signal from particles and what can be considered noise. An illustration of the process is shown in Figure 5.2. If an uneven background exists on the image, a low global threshold value will result in noise being detected as particles. Conversely, a high value will result in fewer particles detected, thus it is important to subtract background non-uniformity contribution in order to best utilise the detection capabilities of our system. The background image is provided by the participant simply breathing for the duration of the recording. No exhaled particles are detected during this process, only few dust and ambient particles that linger mid-air. Since the background image was recorded as a sequence, simply averaging the whole sequence would lead to streaks from the particles continuous motion. Thus, in a sequence consisting of 2700 images, every 7th frame was selected and used to obtain an average image of the background intensity levels. Subtracting this average image resulted in a very even intensity distribution and allowed for a global intensity threshold to be selected in order to distinguish the particles from noise.

After subtracting the background contribution, a global intensity threshold is chosen by probing the average noise levels in a few dark areas of the image and multiplying by a factor of 3. This way, we can be certain that the remaining background will be

suppressed when applying the threshold value. There is no obviously right or wrong approach when selecting a threshold value, however, it is important to always communicate the procedure to the reader. Subsequently, the face of the participant, along with a buffer zone around the face are masked off the image in order to not interfere with the particle detection. The buffer zone is necessary since the participants face is not stationary across all image sequences and can move in and out of the frame. In addition, the high intensity light, scattered off the face dazzles the neighbouring pixels of the detector. A mirroring reflection of the face is also formed internally in the objective lens of the camera and was not possible to remove with the background subtraction, thus a zone, 200 pixels wide, is cropped and excluded from the analysis. From the initial camera resolution of 1024x512 pixels, the final image that is processed is 699x512 pixels.

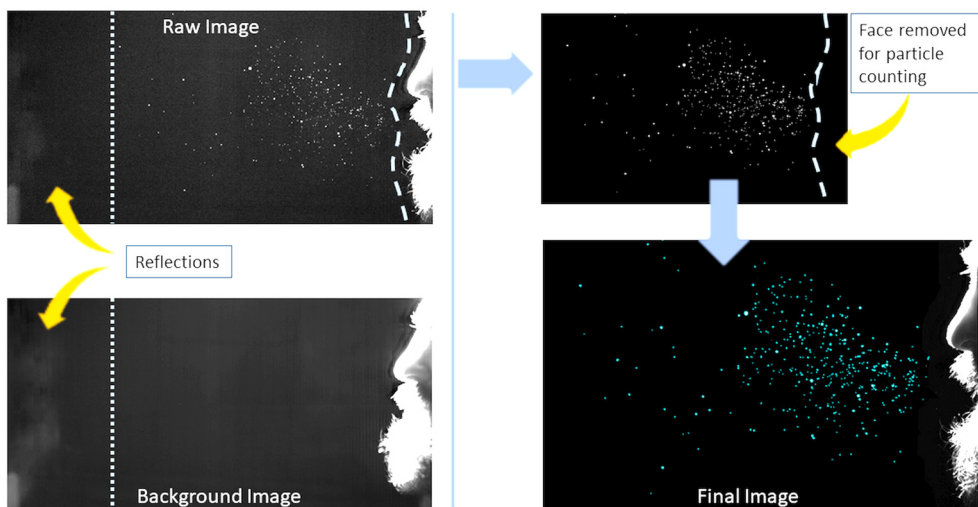


Figure 5.2. Illustration of the data processing used. First the background contribution is subtracted and the face of the participant is removed along with a surrounding buffer zone that due to the high intensity of the light dazzled the neighbouring pixels of the sensor. The picture is cropped to avoid reflections of the participants face and finally the particle counting can be performed.

The analysis of the final processed image is then performed in Matlab (Mathworks®) with a custom routine relying on the function “regionprops”. The final image is a logic character matrix, where detected particles are islands of ones in a background of zeros. Individual regions of ones are counted in order to obtain the number of particles, the area of each is stored, along with the coordinates of the centroid of each region. Thus, the derived parameters are number of particles, size and position of each across all frames of each image sequence. Since the verse that participants voiced was the same across all cases, it was possible to correlate number of particles to specific letters being voiced and the dependence on loudness and tonality. Higher tonality and volume always resulted in a higher number of particles

exhaled and consonants like ‘p’, ‘b’ and ‘t’ were identified as the ones with the highest production of droplets. In the case of vowels, plain breathing and wearing a mask, no emitted particles were detected. This does not necessarily mean that no particles are exhaled, but the detection capabilities of the system might be limited because of the decision to image a large FOV. However, the primary goal of the experiments was to study the number of particles, how far they reach and investigate their motion. An example of the results obtained can be seen in Figure 5.3, where one of the participants was singing loud with exaggerated diction and the graph on the left illustrates how the number of particles varies depending on the letters voiced across the verse. The black dotted line indicates where the verse ends and starts over across the sequence. The position of the peaks in the curve of emitted number of particles are found to be quite symmetric on the left and right side for this participant, not in absolute numbers, but rather the trend which very similar between the two verses. This was not the case for other participants, where the curves did not repeat so well and varied significantly depending on the saliva production or accumulation throughout the approximately 20 seconds of recording. Thus, in such studies where the number of particles is important, the verse should be repeated multiple times to ensure that the result is not affected by such factors that are not easy to control or keep constant.

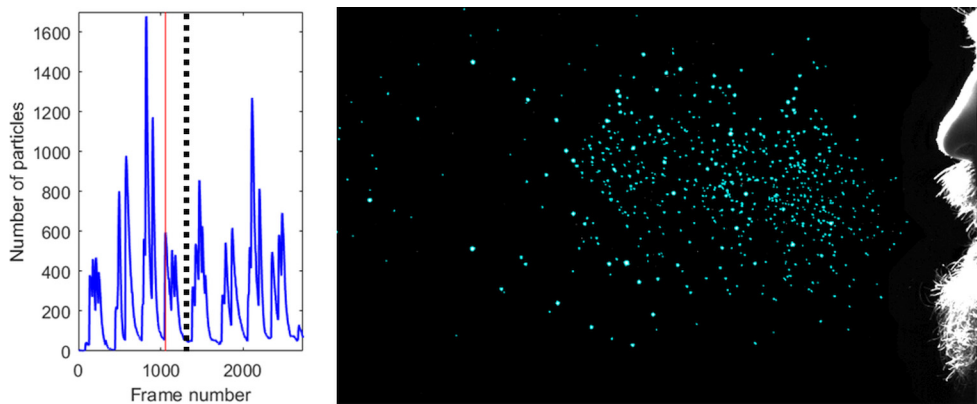


Figure 5.3. Image of a choir singer singing in high tonality and high volume with the detected particles outlined in cyan colour. The graph shows the number of particles over the whole image sequence and the red bar indicates the frame corresponding to the image. The black dotted line indicates where the 1st verse ends and then repeats along the sequence and the symmetry of the peaks can be assessed between the two verses.

Motion analysis can be performed via a process called Particle Tracking Velocimetry (PTV). The relative motion of individual particles is followed across an image pair or a sequence of images. In systems where the image ratio is known, i.e., the correspondence between millimetres and pixel resolution, the motion can then be characterised in real world units of speed. In addition, if the motion of the particles is tracked across multiple frames, a track can be assigned to each and the

motion can be visualised very intuitively. Two examples of this process are shown in Figure 5.4. PTV analysis reveals the relative speed and direction of each particle by correlating particle positions between two successive frames of the image sequence. This is a strong illustrative tool that shows the differences in speed and direction that can be expected in such a system and can be expanded across the whole image sequence to study the variations for different letters voiced or the speed variation of individual particles over time. Another way of illustrating the particle path and direction is by assigning tracks to the particle motion and plotting them for a certain interval of images. The differences in speed are visualised as short or long tracks, along with the relative speed of each particle given by following the stepwise position of the particle on each track. In this representation, the path followed by each particle can also be seen, thus providing a very information-dense illustration of the motion of such droplets.

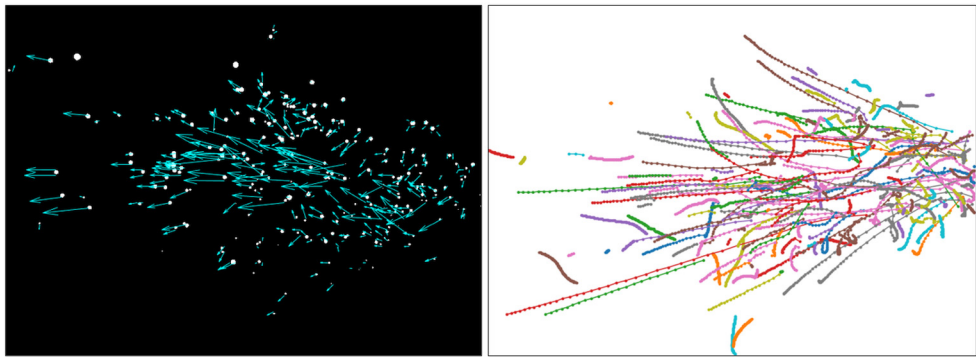


Figure 5.4. Two example images are shown. On the left, an image that comes from PTV analysis of two successive frames and the velocity vectors are plotted along with the particles, thus indicating their speed and direction. On the right, all particles across a span of 150 frames are plotted and tracks are assigned that show the path they follow. Velocity can also be seen by the position interval of the particles. (Right photo, courtesy of Adrian Roth).

5.2. Optical study of methanol

The purpose of this study was to investigate the combustion and injection characteristics of methanol, under a compression-ignition regime. The goal was to compare the fuel mixing process and show where ignition was most likely to occur. An initially wide range of injection timings was reduced to a range of approximately 20° CA (Crank Angle) as it became apparent that methanol mixes rapidly, and no significant benefit comes from injecting earlier. CFD simulations had indicated that methanol ignites on lean mixtures due to the quick mixing and the evaporative cooling of methanol. This was studied by combining a high-speed camera to record the natural flame luminosity, with fuel-tracer laser induced fluorescence to study the fuel distribution before the onset of combustion. In addition, other simulations

showed an increase in NO_x formation for high injection pressures and this effect was optically investigated. Liquid spray length measurements were also obtained for various in-cylinder conditions in order to provide data for spray modelling and compare to other fuels typically used for PPC combustion.

In these experiments, a six cylinder, heavy-duty, direct-injected, compression ignition, Scania D13 optical engine was used, with one of the cylinders converted for optical access in a Bowditch configuration [66]. Three fused-silica windows are housed on the top section of the cylinder liner and a flat fused-silica piston is used. The compression ratio (CR) was set at 16:1 and the engine was operated under a skip-fire regime, with one fired and nine motored cycles. Acetone was chosen as the fluorescent tracer, since the boiling point is very close to that of methanol, 56°C and 65°C respectively, and is not quenched drastically by oxygen [79]. The amount of acetone added to the fuel was 10% (v/v) and based on previous experiments. In these experiments, a six cylinder, heavy-duty, direct-injected, compression ignition, Scania D13 optical engine was used, with one of the cylinders converted for optical access in a Bowditch configuration [66]. Three fused-silica windows are housed on the top section of the cylinder liner and a flat fused-silica piston top is used. The compression ratio (CR) was set at 16:1 and the engine was operated under a skip-fire regime, with one fired and nine motored cycles. Acetone was chosen as the fluorescent tracer, since the boiling point is very close to that of methanol, 56°C and 65°C respectively, and is not quenched drastically by oxygen [79]. The amount of acetone added to the fuel was 10% (v/v) and based on previous experiments [80, 81], while lower tracer concentrations would also be adequate to visualise the fuel distribution, more tracer yields better signal/noise ratios, particularly in early injection cases where the fuel mixture is diluted. Since acetone has lower octane rating compared to methanol, its addition forms a slightly more ignitable mixture, requiring ~2% lower inlet air temperature for the same CA50 phasing. Nevertheless, when studying the heat release, no major difference was observed in the way combustion takes place. A 10 Hz, 266 nm wavelength laser was used to excite the acetone, with a laser pulse energy of 60mJ and the beam was formed into a sheet 55 mm wide and ~0.5 mm thick. In order to capture the natural flame luminosity and the spray motion, a high-speed camera was used, operating at 30 kHz while the engine operated at 1200 rpm, resulting in a temporal resolution of ~4.16 frames per crank-angle degree (CAD). No filters were used on the (HS) camera and the exposure was set to 30 μs for the NL images and 5 μs for Mie-scattering experiments to avoid blurring of the spray motion. Simultaneously, an ICCD camera with a UV-transmitting lens was used to probe the fuel distribution by detecting the fluorescence signal of acetone, through a 30 mm thick dimethyl-formamide liquid filter to attenuate any laser light. Due to some jitter in the laser pulse arrival time, the minimum exposure time allowed was 110 ns, enough to suppress NL in the acetone PLIF recordings however, since methanol is a low-sooting fuel. In order to keep the image data consistent, the intensifier was operated

at a constant gain for all operating conditions. The two cameras were mounted perpendicular to each other with the ICCD camera pointing straight towards the Bowditch mirror, while the HS camera was at a right angle and recorded via an additional mirror angled at 45° . This second mirror was placed right next to the lens of the ICCD camera and thus sharing the optical access. A custom-built 3 W, 452 nm wavelength, continuous wave (CW) laser was used to visualise the liquid sprays by means of elastic light scattering. The beam was expanded to a rectangular cross section and entered the combustion chamber through another side window. These experiments were performed independently from the fluorescence measurements to avoid signal crosstalk; however, its addition enabled the unaltered optical setup to perform scattering experiments as well. A custom Lab-View interface controlled the engine operation and the triggering of the optical components. The laser system required a 10 Hz signal, once every full cycle at 1200 rpm, while the cameras only received a trigger when a fired cycle occurred. The HS camera was triggered to start recording five frames before the laser pulse arrived, then captured the fluorescence on the sixth frame along with the ICCD camera and continues to record for 40 frames in total. The HS camera also captured the fluorescence since acetone's emission is spectrally broad and reaches into the visible region. The calibration procedure and the overlaying of the two frames is described in section 4.1.4.

5.2.1. Combustion Characterisation

One of the main goals of this study was to characterise methanol combustion, relative to fuel distribution and an important part of combustion characterisation is combustion location. Typically, a number of cycles is recorded, approximately 50 in this case, in order to have high confidence that some effect or feature is consistent and repeatable. Any type of combustion exhibits cyclic variations in internal combustion engines, but even more so in the case of methanol as a fuel. In [40], an order of magnitude greater cyclic variations were observed in terms of SOC when running on methanol, compared to a typical diesel fuel. In our study, variations in SOC were optically derived and were found to range up to 3-4 CAD, thus similar to the findings in [40], despite the absence of a glow-plug. Simply averaging the NL image sequences on a frame-to-frame basis would therefore introduce high uncertainties on the average combustion area and location, particularly in the early stages of combustion since SOC will not occur in the same frame. To combat these variations, the image sequences were time-shifted and phase-locked to start of combustion. The significance of this effect is shown in Figure 5.5. The orange box shows the phase-corrected case, where all curves representing combustion progress (combustion area on the image) share a common start while the raw curves in the blue box show a big spread due to cyclic variations. The phased average curve demonstrates an almost linear response while the non-phased curve shows a more exponential increase. The image shift however, results in a reduced number of available frames, proportional to the number of shifts necessary for the required

phasing. The resulting fewer frames are not a concern as mostly the early ignition behaviour is monitored and the correlation to the probed fuel distribution is only valid for the early stages of combustion. Cycles that require shifts greater than 13 frames, equivalent to ~ 3 CAD, are excluded from the analysis along with cycles where combustion pre-dates the PLIF image. The phasing effect on the average combustion images is also demonstrated in Figure 5.5 where half the cylinder is shown. While the phased image appears almost as a single-shot image, in the non-phased average, frames with a wide flame spread from advanced combustion merge with delayed combustion cycles, creating an inconsistent image.

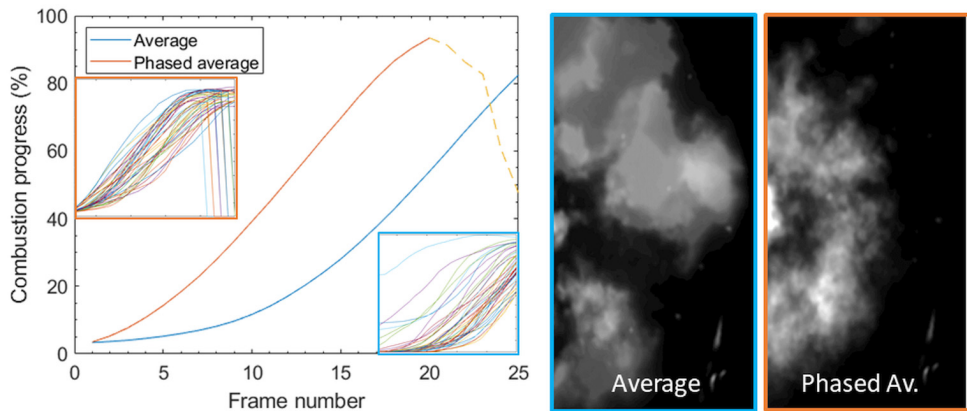


Figure 5.5. Illustration of the effect of phasing the image sequences to start-of-combustion. The resulting common-phase average image shows a consistent spatial representation of the flame.

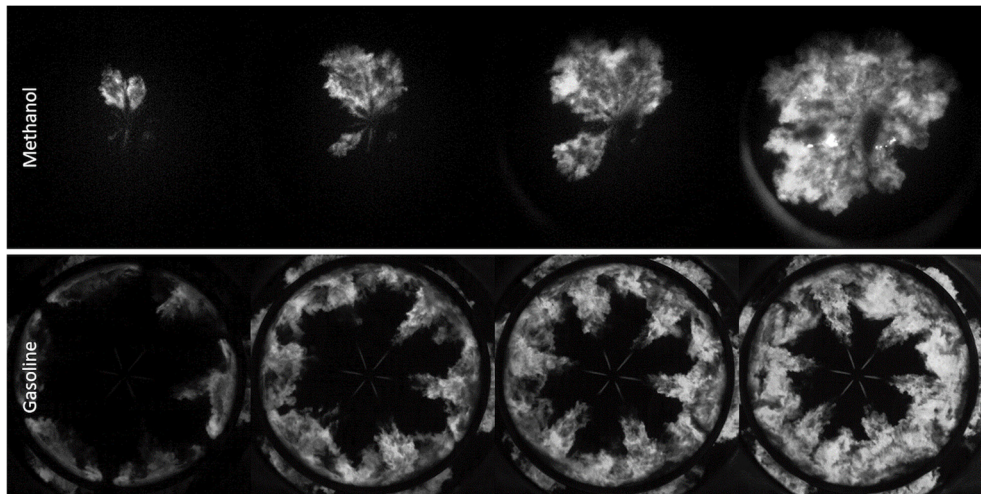


Figure 5.6. Image sequences showing the difference between methanol and gasoline combustion in spray-driven conditions. Methanol ignition is very close to the centre of the injector and burns without any measurable lift-off length, while gasoline combusts in the typical Diesel-like fashion.

Commonly, in diesel-like combustion, ignition occurs after an initial ignition delay, somewhere downstream in the fuel spray jet. The ignition location will depend, spatially, on where the most favourable conditions exist for auto-ignition. Depending on the piston geometry, the in-cylinder conditions and the injector parameters, ignition will occur where the most reactive mixture is formed, according to the combination of local temperature and fuel/air ratio. Following the path from the injector orifice and radially outwards into the cylinder, the injected liquid fuel gets vaporised and mixes with the air inside the chamber. As a consequence, with increasing distance from the centre of the bore the mixture is heated and the fuel/air ratio drops. Thus, hotter and more ignitable mixtures are formed at greater distances from the centreline of the bore and these locations are where auto-ignition will occur. The initial auto-ignition sites will then grow to form individual diffusion flames that are stabilised at a certain distance from the injector nozzle by the fuel jets coming off the injector. This distance is commonly known as the lift-off height or length and corresponds to the metastable equilibrium point between chemical oxidation and mixture reactivity. As the combustion chamber is of finite volume and heat conduction, the heat from the combustion will increase the cylinder temperature, thus increasing the reactivity of the fuel mixture, which in return forces lift-off length to become progressively shorter during the injection process until the new metastable equilibrium is achieved.

Having corrected for combustion phasing, the average images can be evaluated in terms of combustion location and progression. In Figure 5.7, the results are shown for all the SOI timings studied. These cases range from spray-driven combustion for SOI -7 and -10° CA, to premixed for SOI -17 and -25° CA. Here, the negative sign indicates before top-dead-centre. SOI -10° CA represents a boundary case where the end of injection coincides with the start of combustion and can be considered partially premixed combustion, as per definition. The two early injection cases don't show any significant differences when compared to other fuels such as low octane gasoline blends which are commonly used in a PPC regime. Combustion luminosity is overall low as only small amounts of soot are formed and the flame emission is dominated by chemiluminescence as plenty of mixing time is allowed and low local fuel/air mixtures are prevalent when combustion takes place. Due to the flat piston used and the wide umbrella-angle of the injector, even earlier injection cases like -35° and -46° CA resulted in the majority of the fuel finding its way outside the field-of-view offered by the piston design and were excluded from the study.

The spray-driven cases of SOI -7 and -10° CA combust quite differently with methanol compared to conventional diesel combustion. Initial combustion location is not found to be downstream of the spray jet, but rather close to the injector nozzle and the centre of the cylinder. This can be attributed partly due to the fact that methanol reaches stoichiometry much quicker compared to non-oxygenated fuels and thus ignition location is expected to be at upstream locations. In the time-resolved sequences, as shown in Figure 5.6, combustion initially seems to be similar

to a conventional-diesel flame only miniaturised, with small flamelets established at minimal lift-off lengths. However, the flame luminosity is very different as the highest intensity is found outside the centreline of the jet, with the tip and the central

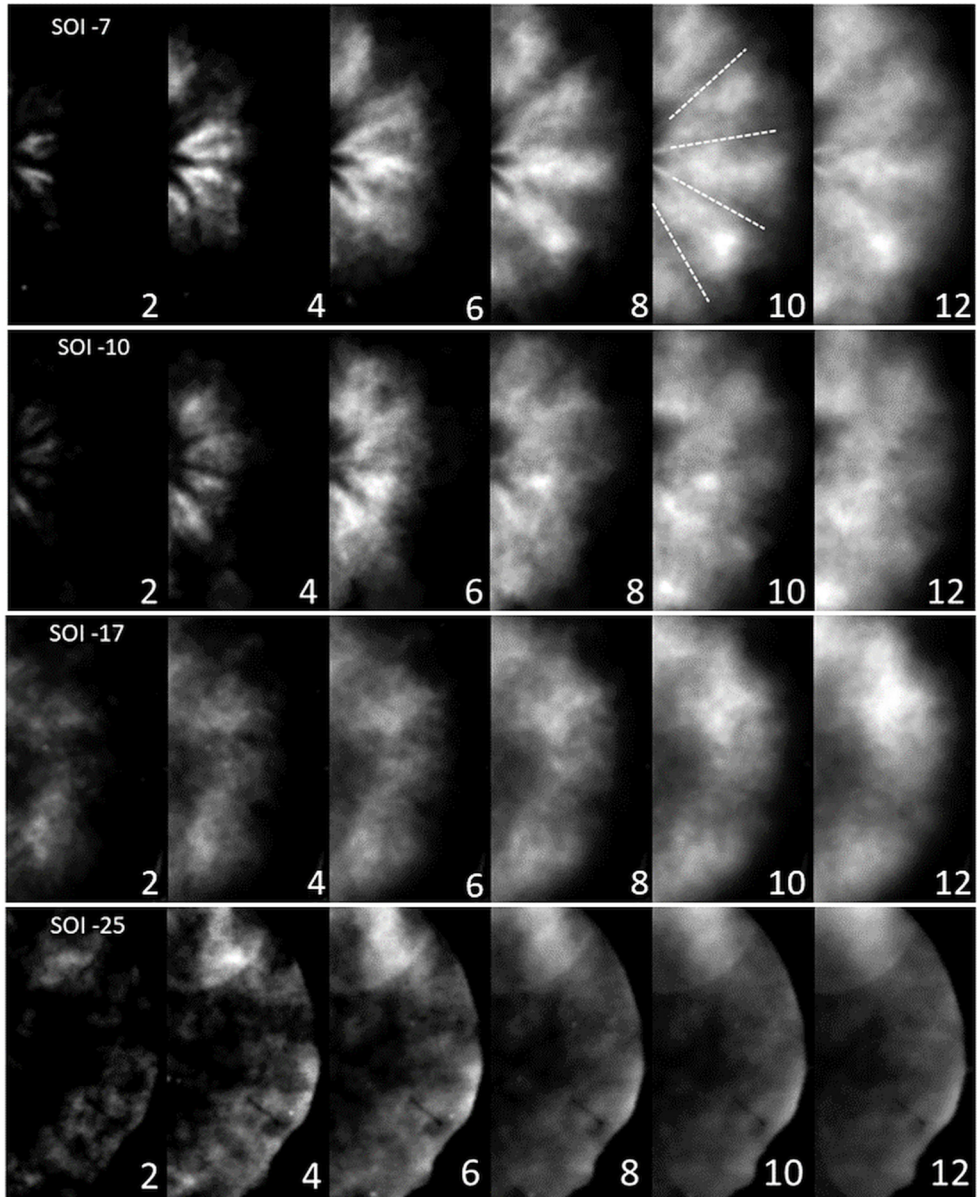


Figure 5.7. Phase-corrected average images showing the progression of combustion for the four different SOI timings. The number at the bottom right of each image is frame number after SOC. Given the 30 kHz frame rate of the detector, each frame is 33.3 μs apart, thus the time-interval between each image in this graph is 66.6 μs .

regions of the flamelets showing much lower intensity, presenting almost an inverse view of a typical diesel flame. This V-shaped luminosity profile becomes more apparent for the spray-driven cases on the average images shown in Figure 5.7. In the case of SOI -7° CA, this intensity profile persists until late in the combustion process, even 3-4 CAD after ignition. Essentially, this profile remains for the duration of the injection event indicating that some extinction is taking place within the centreline of the spray jet. The hypothesis here is that the line-of-sight integrated signal is lower at the centre of the spray jet in comparison to the region surrounding it. Since so little soot is formed during methanol combustion, we are allowed to look through the flame surface and collect all of the emitted chemiluminescence signal. This is very improbable in sooty flames as they are optically opaque, and signal emitted from inside or behind the flame is trapped. The collected signal is derived predominantly from the flame outer surface which is facing the detector. For methanol, assuming that the centre of the spray jet is not combusting, most probably due to the high heat of vaporisation of methanol, the result would be less flame emission integrated along the centreline in comparison to the periphery of the spray jet. Corroborating with the previous hypothesis is the case of SOI -10° CA, where this V-shaped intensity profile is not as prominent and does not persist until late in the combustion cycle. The injection process stops almost concurrently with the start of combustion; thus, no extinction occurs along the centreline of the spray jet and the intensity distribution on both, the real-time and the average images, is more homogeneous.

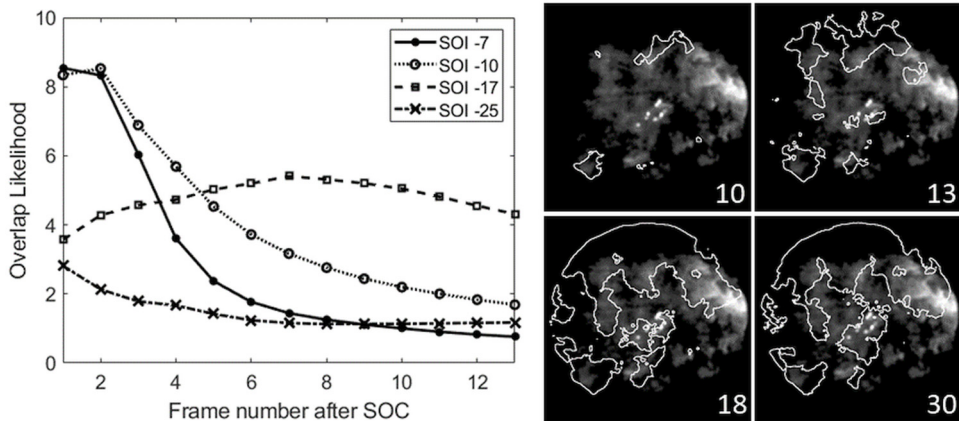


Figure 5.8. Graph of the overlap likelihood of cycle-resolved combustion (white contours) over the single-shot PLIF fuel distribution image. This assessment is performed to understand if and for how long the fuel distribution image is relevant for. The number on the bottom corner of the overlaid images corresponds to the actual frame number of the image sequence, while the frame number on the graph is the phase corrected number.

Overlaying the average combustion images with the average fuel distribution images allows to visualise the preferable pathways of combustion relative to the fuel concentration. Initially, a sensitivity analysis is performed in order to see whether

the single PLIF image obtained before the start of combustion is relevant and for how long. This is necessary in order to understand if the planar technique that is probing the fuel distribution provides an image that is representative of the whole cylinder which is three dimensional. Additionally, this analysis is required since only a single laser pulse is possible for each cycle and thus cannot provide the cycle-resolved fuel distribution. The single-shot fuel distribution image is overlaid with the cycle-resolved combustion images and assessed for all the SOI cases investigated in this study. The results can be seen in Figure 5.8, where in the late injection cases the overlap likelihood is initially very high and drastically reduces after the first few frames. The reason for this is that the injection process is still ongoing when the PLIF image is obtained, thus the final fuel distribution will be different. Nevertheless, the difference is mostly found at how far the fuel has penetrated into the bore and the fuel distribution is largely the same as will be seen in Figure 5.9. For the early injection cases of SOI -17 and -25° CA, the overlap likelihood is lower initially but more consistent for the duration of the image sequence. SOI -17° CA in particular, presents the case with the highest overall likelihood, since the injection process has finished by the time the laser pulse probes the fuel distribution and the fuel is well contained within the imaged area. For SOI -25, fuel is delivered outside the imaged area and close to the cylinder walls as the piston used is flat and cannot contain the fuel. As such, the overall likelihood is greatly reduced for this operating point. In all cases however, the overlap likelihood is above two, meaning that it is twice as likely for combustion to occur on a region where the fuel distribution is probed by the laser sheet and thus can be used to evaluate the combustion progress relative to the fuel distribution, especially for the first few frames after the onset of combustion.

After establishing that the fuel distribution obtained is relevant to the dynamic and three-dimensional effects taking place, the average images are overlaid and the combustion progress is compared to the fuel distribution. The results can be seen in Figure 5.9, where the full set of results is shown and Figure 5.10, where the average fuel concentration of the combusting areas in each frame is plotted. As combustion progresses, it sweeps through the fuel map and we obtain a trend over the preferred pathways. To improve the accuracy of the fuel concentration estimation, between each frame only the newly combusting regions are used to obtain the area of the fuel map and derive an average fuel concentration (white areas on figures). The trend is similar for the two spray-driven cases as they both sweep rapidly from initially high fuel concentration to low after the first few frames. Equally similar are the two premixed cases but inversely, they ignite at low fuel concentration and gradually progress towards higher fuel concentrations. The tendency here however is less pronounced especially since the fuel distribution is much more homogeneous. In all cases, it seems like ignition is a geometric function rather than a function of fuel concentration, with the first areas of combustion appearing at the same location close to the centre of the cylinder regardless of the injection timing.

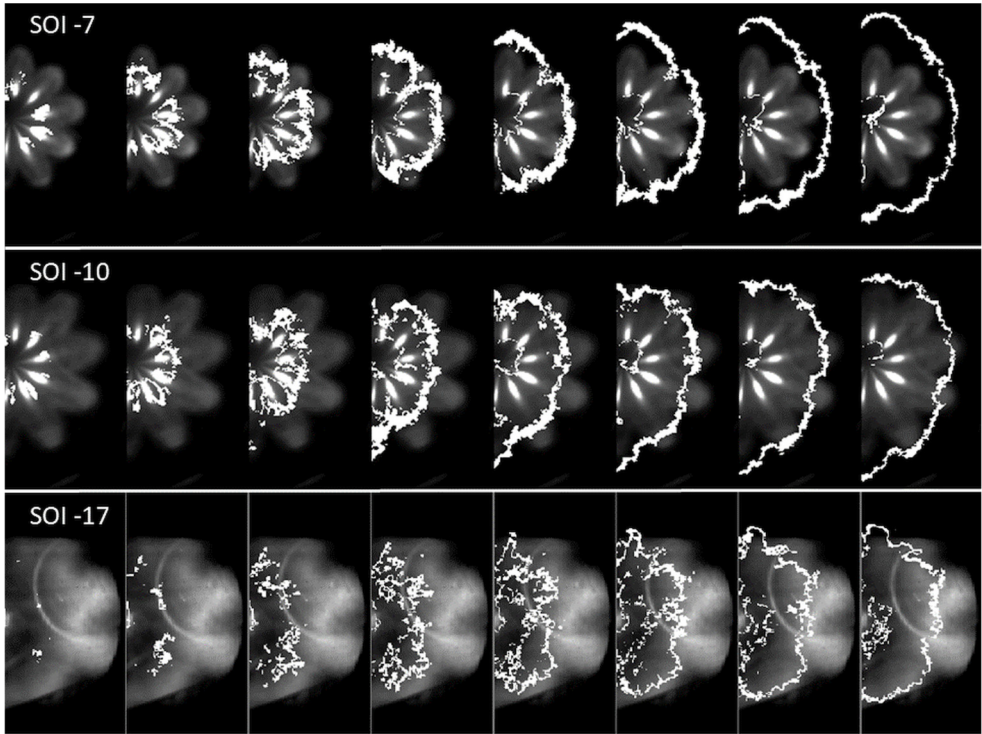


Figure 5.9. The combustion progress of the average sequences is overlaid on the average fuel distribution image for each SOI. Only the newly combusting regions are shown in each frame as it sweeps across the fuel map.

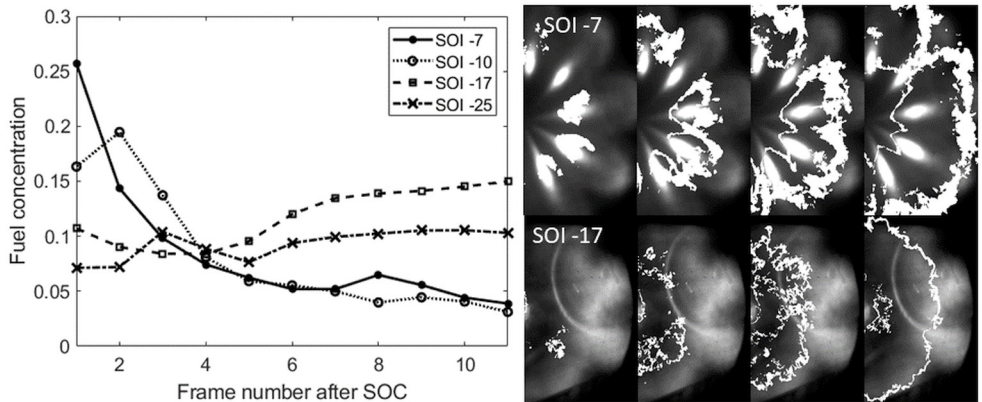


Figure 5.10. The graph illustrates the average value of fuel concentration for the areas over which combustion occurs for the various injection timings. The images of the two SOI cases shown are not at the same image ratio as SOI -7 is cropped and zoomed in further.

5.2.2. Injection Characterisation

In this chapter, the spray and mixing characteristics of methanol are presented. Since very little data existed in the literature, a comprehensive optical study was conducted, where various SOI timings and different injection pressures were tested with methanol fuel, along with a comparison to PRF81, a low octane gasoline surrogate fuel, in identical in-cylinder conditions. The analysis is performed in terms of liquid spray length, spray cone angle and fuel distribution. The first two are found by elastic scattering of light from the liquid fuel droplets while the second is based on fuel-tracer PLIF of acetone as seen in the previous section.

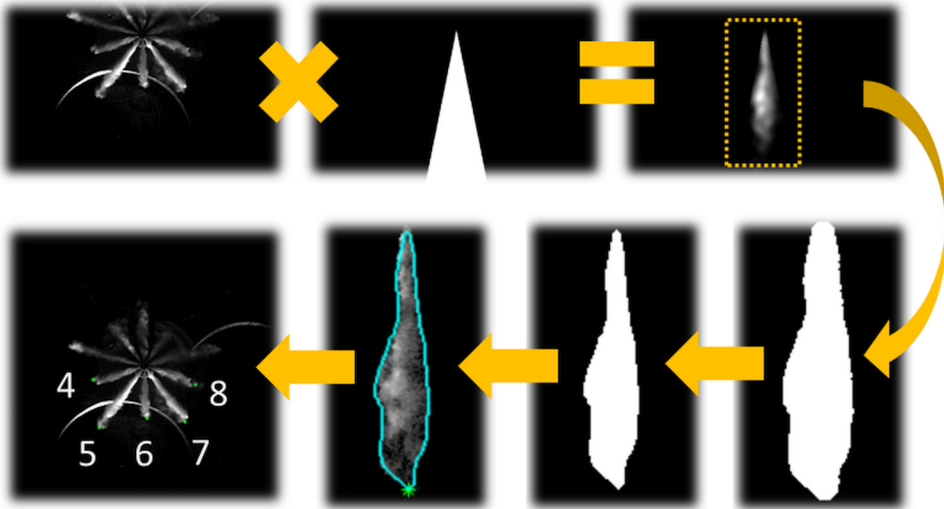


Figure 5.11. Image processing routine to determine liquid spray length. A pie-cut sector is selected to isolate each spray, a smoothing filter is applied and finally an erosion step follows to account for dilation due to the smoothing process. Then the furthest point from the centre of the bore is found as the spray tip.

In order to derive the liquid spray length and the spray cone angle, first the raw images need to be processed to offer consistent and accurate results. The injector tip is selected as the centre of the bore and is used as a reference point for the image. Based on this new coordinate system, a pie-cut sector is selected to include just one of the 10 sprays. Then, a disk-shaped averaging filter, 4-pixel wide, is applied on the image to reduce sharp intensity differences and noise across the image, thus clearly revealing the liquid spray boundary, albeit with less accuracy as discussed in section 4.1.1. A global threshold is then applied, and a binary image of the spray is derived. The vaporisation process is not linear as sprays are highly turbulent, so it is often difficult to distinguish the tip of the liquid spray jet as, often, large parts break off or shade the main spray body. Here, after the images have been binarised, the region with the largest area and closest to the injector is selected as the main body of the spray jet and all smaller regions are discarded. Subsequently, a 2-pixel

wide disk erodes the outline of the binary jet to account for overestimation due to the smoothening filter applied previously. Then, the pixel that is furthest away from the injector tip is selected as the maximum liquid penetration length. The sprays originate from the injector orifices however, not the centre of the bore, thus that distance (14 pixels) is subtracted from the derived length to account for the injector size. Having characterised the first spray plume, the pie-cut sector is rotated 36° so that it falls on the neighbouring spray plume and the same process is repeated, until all spray plumes are measured. An illustration of this image processing routine can be seen in Figure 5.11. The measurements are performed in pixels and the camera has a constant image ratio which can be found by imaging a physical object of a known size, such as a checkerboard pattern with a known box size. The measurement in pixels is performed by using polar coordinates in order to determine the liquid penetration length. Finally, the injector orifices in compression-ignition engines are commonly angled downwards, towards the piston surface, in order to avoid fuel being delivered in crevice volumes and the cylinder walls. The characteristic unit for this is the in-between or umbrella angle of the injector and refers to the angle between the sprays in the plane vertical to the cylinder head. In this set of experiments, the umbrella angle was 156° , or 17° off the plane of the cylinder head. Thus, the measured liquid length needs to be multiplied by a factor of $1/\cos(17^\circ)$, so the real liquid length is approximately 4.6% greater than measured.

The cone angle is estimated according to [82], by assuming a triangle with the top corner on the injector nozzle as the start of the spray plume, and its base at half the length of the liquid penetration length. With this approximation, the equation can be derived to calculate the spray cone angle α as:

$$\alpha = \tan^{-1} \times \left(\frac{A_{p,S/2}}{(S/2)^2} \right) \quad (5.1)$$

where, S is liquid spray length and $A_{p,S/2}$ is the projected area of the triangle formed by half the upstream spray plume. By knowing the maximum length and the area of the spray plume up to half the liquid length the cone angle can be derived. This half-spray area is derived by placing a normal line at half the spray length and counting the pixels in the upstream region of the binary image.

Spray vaporisation is highly dependent on in-cylinder conditions, particularly air density and temperature. By evaluating the liquid penetration length for different SOI's, we can determine how each fuel is affected by temperature and air entrainment during the injection process. In this study three SOI's were tested, -8, -25 and -46° CA, thus one spray-driven case and two well-mixed cases representing partially premixed combustion. The injection pressure was 800 bar and injection duration 900 μs , intake pressure was set at 1.5 bar and inlet air temperature was 70°C for all the cases. Since the data would be used for spray model validation, the operating conditions were set in order keep the initial conditions identical for all

cases and to avoid combustion as that would interfere with the liquid length measurements. Thus, the only difference between the cases was the in-cylinder pressure and temperature, due to the timing of the injection and at which stage of the compression stroke they occurred, so the dependence on those two parameters can be studied. The results can be seen in Figure 5.12 along with an average pressure trace recorded by the pressure transducer inside the cylinder. The exact temperature and air density can be derived with simple thermodynamic equations and the injection models can be validated with the experimental data acquired. The differences are quite interesting as, both, the maximum liquid length and the transient response of each spray can be seen for these cases. The maximum liquid length is progressively shorter due to the increase in temperature which helps vaporise fuel faster and increased air density that causes more air entrainment as soon as the fuel exits the injector nozzles.

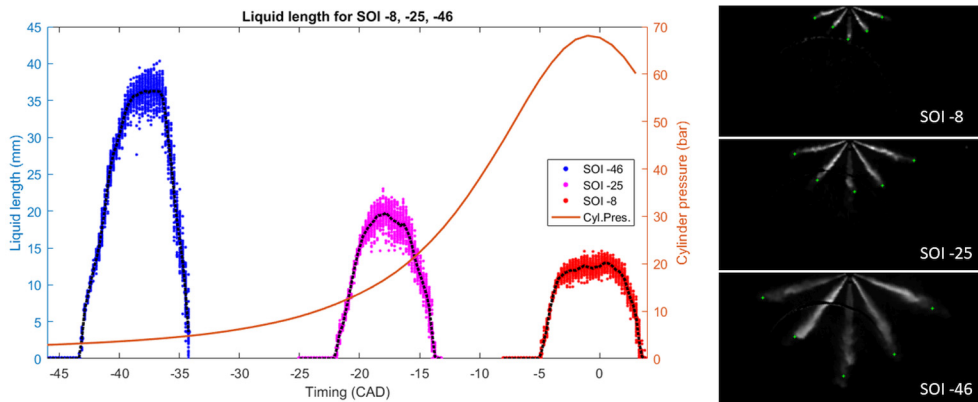


Figure 5.12. The graph shows the derived liquid spray length for the different SOI's, along with the curve of the measured in-cylinder pressure. The variation of the data can also be seen as the dots represent experimentally measured liquid spray length. For illustration purposes, three images are shown on the right side of the figure for each SOI with the sprays at their fully developed length.

Additionally, a comparison was made between the liquid penetration length of methanol and PRF81, a fuel typically used for PPC combustion since it is a low octane, gasoline reference fuel. The inlet temperature was reduced to 20°C to avoid combustion for both fuels, since PRF81 is more ignitable. Two intake pressures of 1.3 and 1.7 bar were tested at two SOI timings of -17 and -35°C. Injection pressure was 800 bar and injection duration 900 μ s in all cases, with the exception of PRF81 at SOI -35°C, where the injection duration was accidentally set at 580 μ s. The results can be found in Figure 5.13, where the right two graphs show the differences to be expected from increasing the intake pressure for both SOI timings. Methanol's liquid spray length seems unaffected by the increase in air-density at both SOI timings, while for PRF81 the liquid length at the plateau region of SOI -17°C is reduced from 22 to 13 mm approximately (top right graph). For SOI -35°C

unfortunately the plateau region was never reached, however, the curve is also lower at the initial transient stage. Meanwhile, the two left graphs of Figure 5.13 show the dependence of liquid length on injection timing at two intake pressures. The liquid length of PRF81 between SOI -17 and -35°CA shows only a small change, while for methanol the liquid length is reduced to almost half (top left graph). To summarise, SOI timings has greater effect on methanol, while intake pressure has a greater effect on PRF81. As such, PRF81 is more sensitive to air density and methanol shows greater sensitivity to in-cylinder temperature. The reason for this behaviour could be that methanol has much higher heat of vaporisation at 1165 kJ/kg compared to 317 kJ/kg for PRF81, leading to a much higher sensitivity to heat. In addition, the density PRF81 is lower at approximately 690 kg/m³ compared to 786 kg/m³ for methanol, which might explain the increased sensitivity to air density.

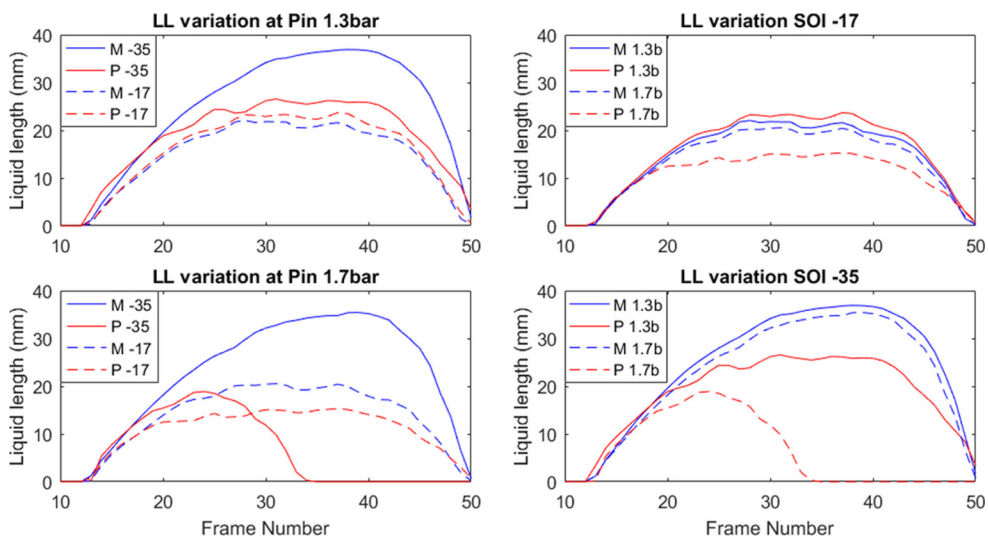


Figure 5.13. Liquid penetration length of methanol and PRF81 for different SOI and intake pressure. The two left graphs show the effect of SOI, while the right graphs illustrate the dependence on intake pressure.

Another parameter investigated was the injection pressure, where three cases were tested, 800, 1200 and 1600 bar. The operating conditions in this part of the experiment were carried over from a previous study performed in a metal research engine [83, 84] and in CFD simulations [2, 83, 85]. The injection duration and timing were adjusted in order to compensate for the increased injection pressure, so that the fuel mass and combustion timing were kept the same. This was done in order to study the effect of rail pressure for the same engine load and realistic condition and as a result, the injection timing had to be delayed by 1°CA for every 400 bar increase in rail pressure. The results regarding liquid length and spray-cone angle can be seen in Figure 5.14, and Table 5-1. Only minor differences are observed regarding the fully developed sprays, however, the transient phase until

the liquid length reaches the plateau region is affected, particularly in the case of 1600 bar injection pressure, with a much faster development rate and an earlier peak in spray cone angle. Interestingly, a downward trend is observed for all cases after the initial peak in liquid penetration length, followed by a progressive increase towards the plateau region. The duration of this downward trend is different depending on the injection pressure and that is also summarised in Table 5-1.

Table 5-1. Engine operating conditions and summary of the liquid length measurements for all cases.

Rail pressure	800 bar	1200 bar	1600 bar
SOI timing	-14° CA	-13° CA	-12° CA
Injection duration	1520 μ s	1150 μ s	940 μ s
Air inlet Temp.	70°C	70°C	70°C
Inlet Pressure	1.5 bar	1.5 bar	1.5 bar
Initial peak (frame no.)	26	24	20
Downward trend duration	300 μ s	233 μ s	166 μ s
Initial peak LL	18.15 mm	17.42 mm	16.10 mm
Mean LL at plateau	18.17 mm	17.58 mm	16.55 mm

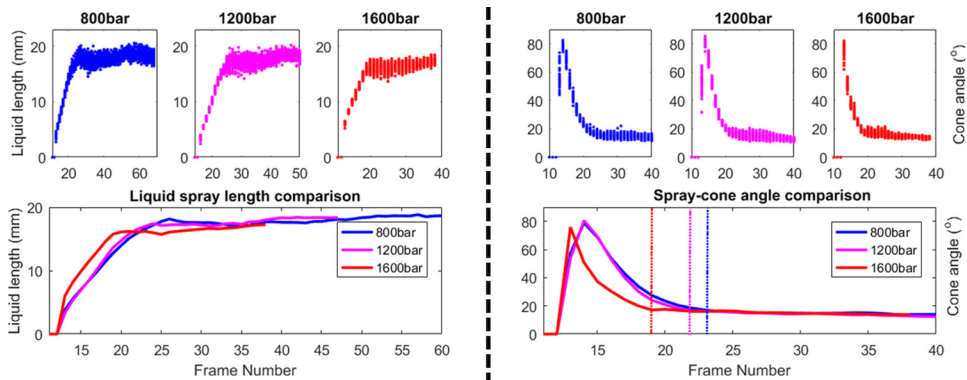


Figure 5.14. The liquid length measurements are shown on the left part and the derived spray cone angle on the right. Only a minor effect is seen on the fully developed spray jet and the biggest difference is the rate at which the spray reaches the plateau region. The colour-coded dotted lines on the cone angle graph represent the point at which the plateau region is reached.

In addition to the liquid spray length and spray cone measurements, the effect of rail pressure was studied in terms of fuel distribution by acetone fuel-tracer PLIF. The laser timing was set at -1° CA in order to probe the fuel distribution before or close-to the timing of ignition. Since the cases studied here were non-combusting, the exact timing of the laser pulse was not crucial but was set close to the timing where ignition would occur. The fuel distribution images are obtained by averaging 50 cycles for each operating condition and are shown in Figure 5.15. These images are colour-coded to three arbitrary intensity bins corresponding to low, medium and

high fluorescence intensity. In this setup the exact equivalence ratio is not known as that would require a calibration procedure which would be challenging since methanol has high heat of vaporisation, resulting in high temperature stratification around the evaporating fuel sprays. This thermal stratification can lead to uncertainty in deriving a reliable fuel/air ratio as the fluorescence yield of most fuel tracers, acetone included, is temperature dependent. Nevertheless, this qualitative analysis is capable of demonstrating the differences between the three injection pressures. The highest injection pressure shows that the highest amount of fuel is found in the lean region and the least in the medium and rich region. The lowest injection pressure on the other hand, shows the least amount of fuel in the lean region and the highest in medium and rich region. Thus, the highest injection pressure of 1600 bar will have the most homogeneous mixture before the onset of combustion, despite the fact that the injection timing is delayed and less mixing time is available. From the studies mentioned previously [2, 83, 84], an increase in NO_x emissions was observed for higher injection pressures with methanol fuel. The explanation was that most of the fuel in the high injection pressure case was combusting at, or close to, stoichiometric conditions resulting in the highest possible flame temperature during combustion, thus, leading to the highest amount of NO_x formation. The findings in this optical analysis seem to agree with this hypothesis, as the highest injection pressure showed the least stratified fuel mixture with most of the fuel in fuel-lean conditions.

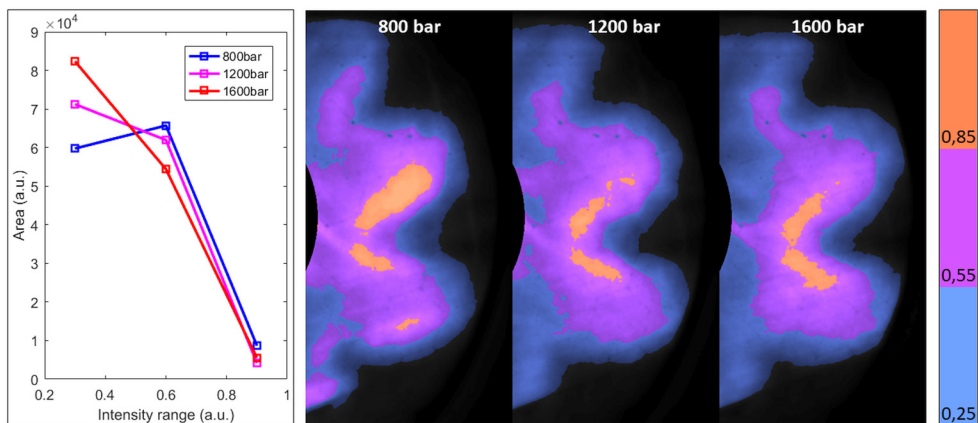


Figure 5.15. The graph illustrates the area covered by the three intensity bins shown on the images. Increasing the rail pressure progressively increases homogeneity and more of the fuel is found on the low intensity region, meaning less fuel-rich mixtures

5.3. Diesel multiple-injection characterization

In this study the objective was to optically investigate the combustion phenomena taking place inside a light-duty engine running on a few multiple-pilot injection strategies with conventional diesel. The main idea was to study the effect of dwell time between the pilot injections on the combustion phenomena and the emitted noise. Three strategies were tested, one with two pilot injections and two with three pilot injections and different dwell times. The injection strategies, along with the resulting cylinder pressure and the apparent Heat Release Rate (HRR) can be seen in Figure 5.16. One strategy was used as a baseline case and was called Reference strategy, which consisted of four injections, a double-pilot, one main and one post injection. The other two called A and B consisted of a triple-pilot injection with Strategy B having shorter dwell times between them. The main and post injections were the same between the two, but their timing was much earlier compared to the reference strategy. Even though the peak pressure and the pressure rise rate were much higher for strategies A and B, the average combustion noise over the whole cycle was significantly lower in these two cases. This comes in contrast to what is commonly believed that the emitted noise is a result of cylinder pressure and pressure rise rate. The combustion noise dropped from 79.6 dBA in the reference case, to 76.5 dBA for strategy A, and 75.5 dBA for strategy B. In the two works presented in this chapter [86, 87] one previous study [88] and a following one [89], a new unit was introduced as a predictor of combustion noise, namely the Ratio of Reduced Heat Release (RRHR). This unit essentially corresponds to the area occupied by the troughs of the heat release and thus, the number and size of undulations of the HRR.

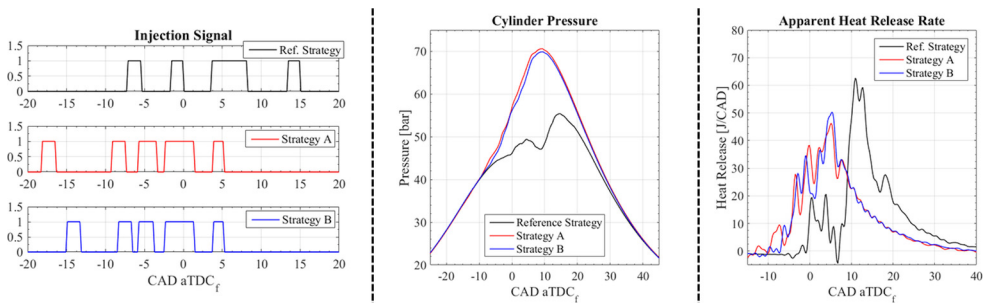


Figure 5.16. The three injection strategies can be seen on the left graph with the resulting in-cylinder pressure in the middle graph and the apparent heat release on the right.

The engine used was a based on a Volvo Cars Euro 6d-temp production diesel engine that was converted for optical access according to the Bowditch configuration [66]. The cylinder head was a special single-cylinder casting with the exact same geometry as the production engine. The top part of the liner was a steel

assembly, that housed four windows to allow for lateral optical access, while the bottom part of the liner was designed to drop and allow for cleaning of the optical surfaces. All optical elements were made by fused silica to allow for UV-light transmission with minimal absorption. The optical piston had a geometry identical to the production engine which, particularly in light-duty engines, results in severe optical distortions. Nevertheless, in the second part of this experiment, the geometry of the piston was used to direct the laser sheet on one of the spray-jet axis and provide a cross-section view.

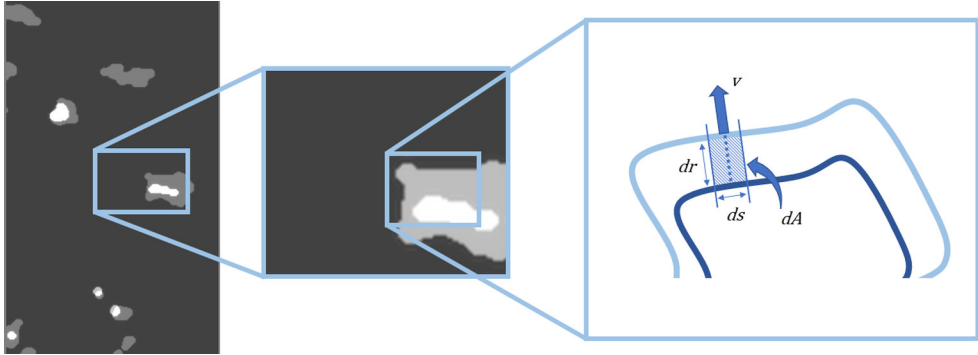


Figure 5.17. Two successive frame overlaid to show the difference in area occupied by the auto-ignition sites, along with the illustration of the process to derive the average flame speed and characterize the type of combustion.

Initially, a high-speed camera was used to capture the natural flame luminosity throughout the cycle and the sprays that were illuminated by a 452 nm CW laser diode. Two setups were used, one with the laser diode off and without any filter, to capture the low intensity cool-flame that occurs when fuel from the pilot-injections auto-ignites, and another setup with the laser diode on and a 452 nm (45 nm FWHM) filter. The 45 nm bandwidth of the filter resulted in a well-balanced exposure between combustion and sprays; it did however filter the auto-ignition sites from the pilot-injections, thus necessitating the “high-sensitivity” setup. This high-sensitivity setup was used to study the auto-ignition sites and the type of combustion taking place. As discussed in section 4.2.1, after the images are processed and undistorted, the ignition sites were analysed in terms of area and perimeter to obtain an estimation of the flame speed. To estimate the flame speed in these areas, we study the radially outward spread of the flames dr , and thus assume combustion to propagate perpendicular to the perimeter. If we take an infinitesimal piece of the perimeter with length ds , we can assume that the propagation speed v is constant along the perimeter ds (see Figure 5.17). After an infinitesimal time-interval dt , the area growth along this piece of the perimeter can be expressed as,

$$dA = ds \times dr = ds \times (v \times dt) \quad (5.2)$$

and integrating along the entire perimeter provides the total area growth over the time interval dt . When the propagation speed is constant along the entire perimeter, the integral along the perimeter will be,

$$v = \frac{\Delta A}{s \times \Delta t} \quad (5.3)$$

Thus, by measuring the perimeter and the difference in area between each time step of the image sequence, we can derive the average flame speed of the auto-ignition regions. The time-interval Δt , is given by the frame rate at which the camera is operated at, in this case 31000 Hz, thus 32.26 μ s.

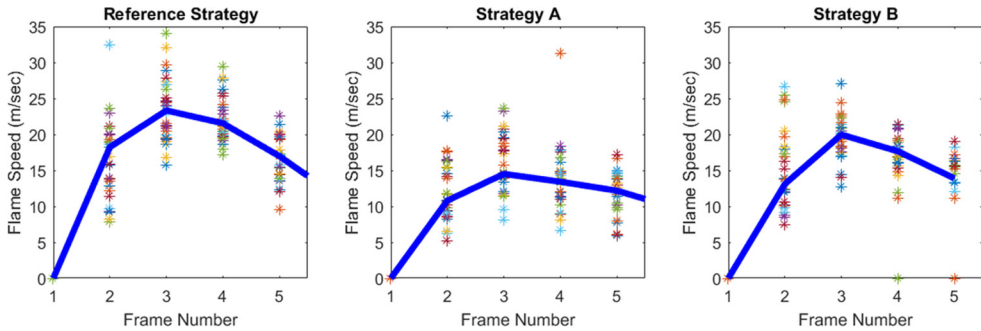


Figure 5.18. Flame speed calculated based on the area/perimeter method. The solid blue line indicates the median values of the data points for the different injection strategies.

The derived flame speeds can be seen in Figure 5.18 and, while the median values ranged from 15 to 24 m/s depending on the injection strategy, in some cases flame speeds up to 35 m/s were seen. These numbers are in line with what can be found in the literature for auto-ignition of these isolated regions [90-94]. Generally, during the phases of low temperature heat release (LTHR) and intermediate temperature heat release (ITHR), the chemical kinetics of the reactions are relatively slow in comparison to the hot auto-ignition phase [5], where speeds greater than 80 m/s have been documented [90]. A potential bias in this measurement is introduced from the fact that the distortion correction is optimised for a certain bowl depth, while the natural luminosity measurement is a line-of-sight technique. The target used to obtain the distortion field was mounted on a fixture that placed it a few millimetres inside the bowl of the piston. The result would be an underestimation in the size of the flame kernels, and thus the derived flame speed, when the ignition kernels are below the plane of the target used for the distortion correction. The opposite is true for flame kernels above the target plane as those would be overestimated in size. Nevertheless, placing the target inside the bowl at approximately half the depth, or where you expect most of the combustion to take place, is the best option for line-of-sight integrated techniques as it is impossible to distinguish the depth from which the signal originates.

Another intriguing finding of this study was a flame extinction phenomenon of the prevailing combustion established during the pilot injections, at the early stages of the main injection. This effect initially was analysed with the overlaying of a preceding frame with one from when the main injection occurred. The result of this process was shown in Figure 4.11, and the three different injection strategies tested showed different extent of the extinction. Reference strategy showed the least amount of extinction as the main injection was postponed significantly compared to the other cases. This effect was investigated further in a following study and is described later in this chapter.

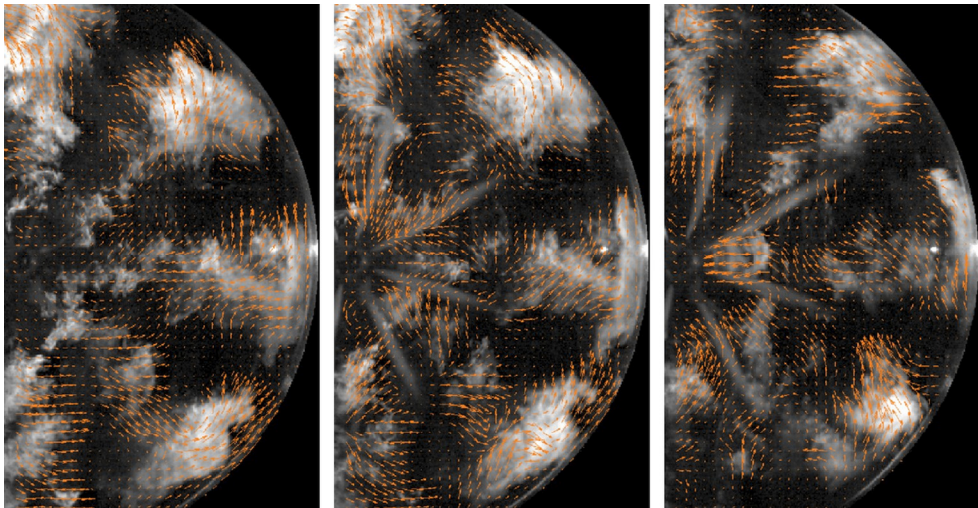


Figure 5.19. Processed frames from the same combustion event, where flame features are used to track motion across the sequence by a pair-wise comparison of subsequent images. The swirl motion is captured along with the reverse flow field created around the spray jet during injection.

In addition to the flame speed measurements and the extinction effect, a technique called Flame or Combustion Image Velocimetry (FIV or CIV) was applied to characterise the processes taking place inside the engine. More details on the technique are described in section 4.2.2 where the processing involved in this experiment is explained. The texture and local features of the flames are tracked over image pairs and their motion is tracked across the image sequence to obtain a sense of their motion inside the cylinder. The results are shown in Figure 5.19, where initially, the flames established by the pilot injections are seen to move towards the bowl and follow the counterclockwise swirl motion of the engine. Minimal motion is observed close to the centre of the bore, partly due to the fact that, since very little combustion is taking place, few features are present to be tracked. Once the next injection starts, we observe that there is a reversal in the flow pattern, approximately up to half the radius of the bowl, while the flames close to the wall are not affected drastically. Small flamelets that were moving along with

the in-cylinder flow are seen to reverse and move rapidly towards the centre of the cylinder and get consumed by the sprays. These motion patterns are evident when reviewing the image sequences, yet it is challenging to convey in written form and impossible to demonstrate without the use of the FIV technique. With the derived vectors plotted over the original images, direction and relative magnitude are communicated intuitively. Nevertheless, there is some ambiguity in distinguishing between a stationary flame or one that moves along the z coordinate, that is outside the horizontal plane of the piston, thus, moving towards the bottom of the bowl or towards the cylinder head.

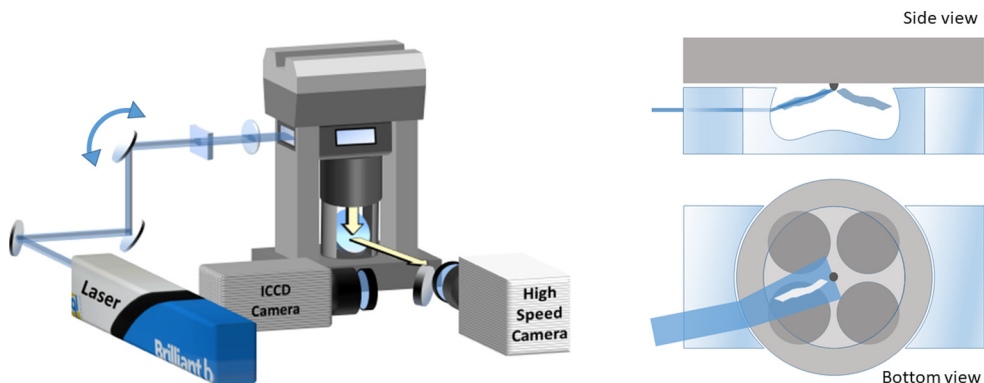


Figure 5.20. Illustration of the optical setup and engine. On the right, the laser sheet alignment and path is shown.

To investigate the extinction effect mentioned previously, the Natural Luminosity study was complimented by PLIF of partially oxidized fuel (POF), in order to see if the extinction coincides with a rise in precombustion radicals and try to explain the dips in the rate of heat release. Similar work can be found in the literature in [81, 95-104], nevertheless this study is among the first to optically investigate multiple injection strategies with LIF of formaldehyde and POF. A 10 Hz Brilliant-B Nd:YAG laser was used that provided 355 nm wavelength laser pulses to excite the formaldehyde and POF and the signal was captured by a 10 Hz Andor ICCD camera. The beam was guided through mirrors into the engine through one of the liner windows, in the form of a 2 cm wide horizontal sheet. The laser pulse energy provided by the laser was set at 40 mJ for stable operation and fluence was quite high due to the sheet's small height. The laser sheet was aligned radially with one of the sprays and was refracted upwards towards the injector tip due to the curved piston bowl-wall geometry. An illustration of the experimental setup and the laser sheet configuration can be found in Figure 5.20. One of the mirrors that guided the beam towards the engine was motorised and could be tilted in two axes. This was of great value as this alignment configuration was heavily dependent on piston position and the POF signal needed to be probed across the whole injection process and multiple crank angle degrees. Thus, for every timing point the laser sheet was

realigned with the motorised mirror and the camera feed, so that the sheet would terminate on the cylinder head, close-to but past the injector tip, to ensure the same cross section of the spray. The high-speed camera was positioned to view straight at the Bowditch mirror and next to its objective lens sat an additional angled mirror through which the ICCD camera viewed the engine. This layout was preferred over a beam splitter, despite making the alignment more challenging, to maintain as high signal as possible for the POF camera. In addition, the placement of the mirror and the cameras were arranged so as to avoid any vignetting that would lead to loss of signal. Both cameras were positioned as close to the engine as possible and the ICCD camera was mounted on a sliding rail with fixed locating tabs, allowing it to be retracted for cleaning of the piston and quickly set back in the correct position.

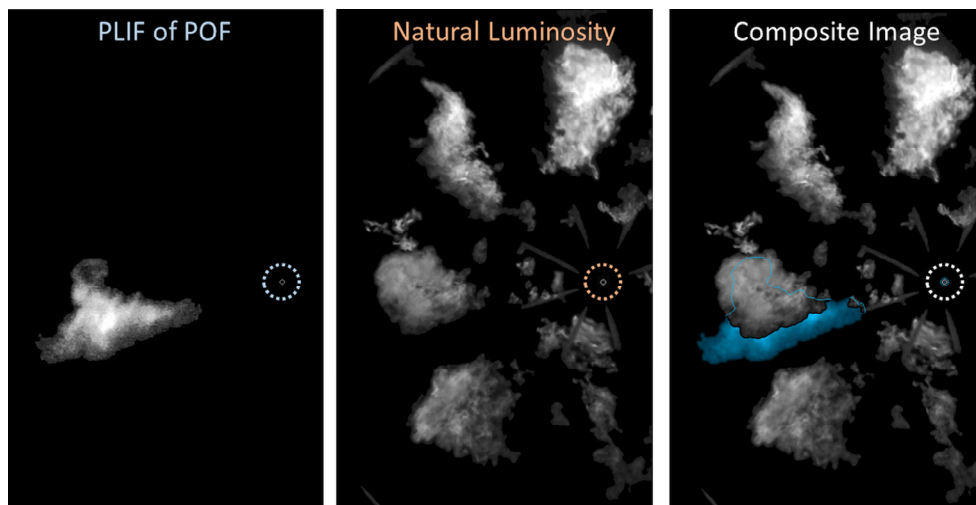


Figure 5.21. On the left the POF is shown and in the middle the natural flame luminosity image. A small circle is inserted where a known item, visible in both images, can be used as a spatial referencing point, in this case the injector tip.

The images from the high-speed camera and the ICCD camera are overlaid with the same process as explained in section 4.1.4. An illustration of this process is also shown in Figure 5.21, where the PLIF image is overlaid with the natural luminosity image. Here, it is important to note that we assume the POF signal to lay behind the natural luminosity as the laser sheet captures a cross-section of the spray jet, where combustion cannot occur due to the high fuel/air ratio. Thus, the outer surface of the flame captured by the high-speed camera is assumed to be over the POF image. A small circle is inserted at the location of the injector tip and used as a reference point to ensure that the image registration is performed correctly for all the images. This was necessary because generally, optical setups are often sensitive to shifts that might occur throughout the experiment by accidental touching during the cleaning of the engine optical surfaces or sometimes even by changes in room temperature. Additionally, in most engine applications the laser alignment is

challenging as the engine is allowed to move relative to the optical setup, since it sits on a cushioned cradle. Thus, the engine can shift over time and due to torque fluctuations during operation, the result is that the dynamic position is most likely different from the stationary position on which the calibration is based. As a result, the image tagging allows for a visual confirmation that the distortion correction and the spatial referencing of the two images are applied correctly.

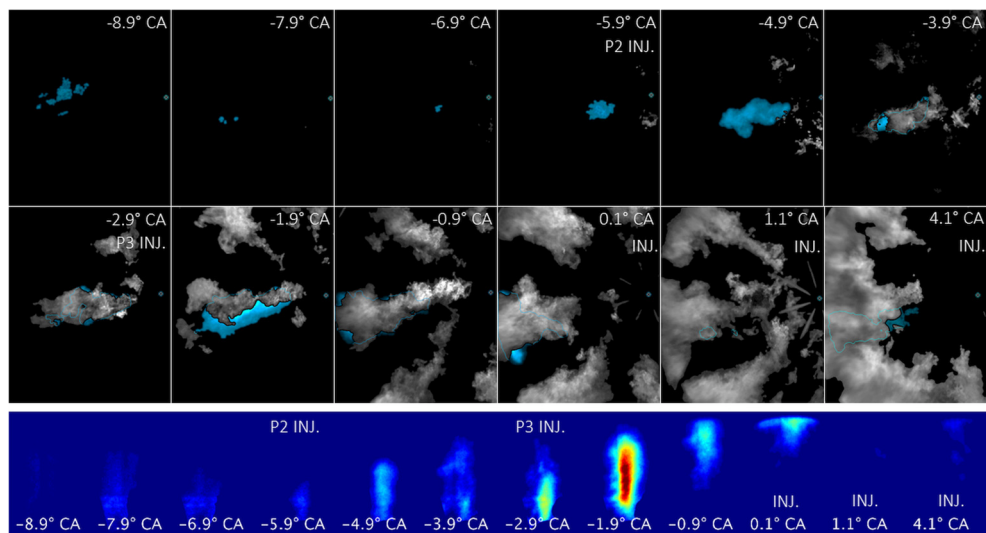


Figure 5.22. The results of the overlaid POF fluorescence and the natural flame luminosity are shown for the case of strategy A in the top part of the figure. A continuous cycle is shown for the natural luminosity with some matching single-shot POF images. The bottom part shows the average POF signals across a few timing points throughout the cycle.

The results from this investigation for Strategy A are shown in Figure 5.22, where some single-shot images are shown of the overlaid natural luminosity and POF, along with the average concentration of POF across the cycle, starting at -8.9° CA and up to $+4.1^\circ$ CA. The injections are also reported to illustrate which injection event is taking place and when it starts. The first pilot injection (P1) is injected at -14° CA and until the timing of -5.9° CA, very little POF signal is present. Similar to what was seen in [87], the high-speed camera could not detect this weak signal since the chemiluminescence of formaldehyde and other partially oxidized hydrocarbons is relatively weak and is mostly emitted in the region of 350-500 nm with the peak at 400 nm, where most detectors are less sensitive. The ICCD camera does however collect the fluorescence signal which is seen to decay until P2 injection comes and starts rising again. P2 pilot ignites shortly after start of injection and encompasses the POF signal indicating that high temperature combustion is taking place. Subsequently, P3 is injected and is seen to extinguish a large part of the natural luminosity, despite the simultaneously very high POF signal, as can be seen for the timing of -1.9° CA. The hypothesis here is that the in-cylinder

temperature is high enough to rapidly start the oxidation processes, aided by the fact that the injection duration is very short. In the next frame the natural luminosity is seen to enlarge and cover the POF, meaning that combustion has progressed and consumes the radicals. The subsequent injection is the main injection and the combustion is seen to be pushed at greater radial distances and close to the bowl-wall, while very little POF signal is observed here. One reason for this could be that the laser sheet is scattered due to thermal gradients at the surface of the bowl wall, or absorption of the laser due to the high concentration of soot. Another hypothesis could be the reduced amount of oxygen available since this is late in the cycle and combustion has progressed significantly. Strategy B showed very similar results across the whole cycle and once again no POF is found during the main injection. In the case of Reference-Strategy, the same extinction effect is observed, however this time only at the start of the main injection and in contrast to the other cases, the POF signal remains strong late in the cycle and during the main injection. A comparison of strategy A and Reference strategy be seen in Figure 5.23, where the injections are shown, along with the heat release and the captured POF signal, while Strategy B is omitted due to its similarity to A.

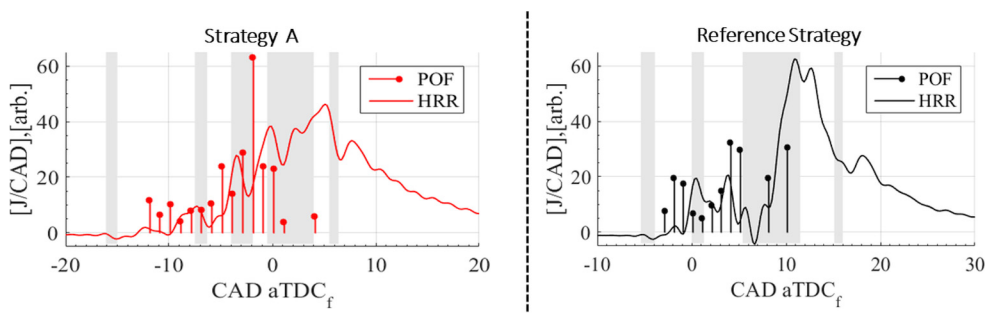


Figure 5.23. The heat release rate is shown for strategy A and Reference strategy, along with the average POF signal and the injection timings and durations indicated in grey bars.

Summarising, hot combustion products are replaced by cooler when a new injection occurs, accompanied by a dip in the heat release and a subsequent rise when the cooler products are combusting. The extent of this mechanism is not fully analysed here and further investigations, in terms of dwell time and injection duration, are necessary to understand the full effect on the dips of the HRR. By combining POF imaging in conjunction with the natural luminosity imaging, it was possible to distinguish at which stage the combustion had progressed. POF with no natural luminosity meant that cooler products are introduced, and flame extinction was occurring; these cool products eventually transition to advanced combustion, which can be confirmed by the simultaneous appearance of natural luminosity in the high-speed camera.

5.4. Laser speckle Background Oriented Schlieren

This chapter will cover some results from lab-scale test experiments of a rather novel implementation of Background Oriented Schlieren (BOS). In conventional BOS, a camera is focused on a characteristic pattern with various features. A picture of this pattern is taken as a background and then a schliere, or an object with some density variation, that we want to characterise is placed somewhere in the volume between the camera lens and the pattern. Due to the density variation of this test object, the background pattern will appear distorted according to the density variation and its distance from the background. The benefit of the BOS technique is the theoretically unlimited applications in terms of physical size and working environment, provided sufficient distance to the characteristic background is allowed. Additionally, the optical setup requires minimal technical equipment with only a camera and a background necessary. Applications range from airplanes mid-flight, helicopter blades in real-time operation, along with stereoscopic approaches where multiple image sensors are used with multiple background patterns and tomographic reconstructions show the three-dimensional flow patterns. The major drawback with this setup is that the camera needs to be focused on the background and, since the requirement is usually high sharpness, the object that causes the density variation is far from the background, thus out of focus and not visible.

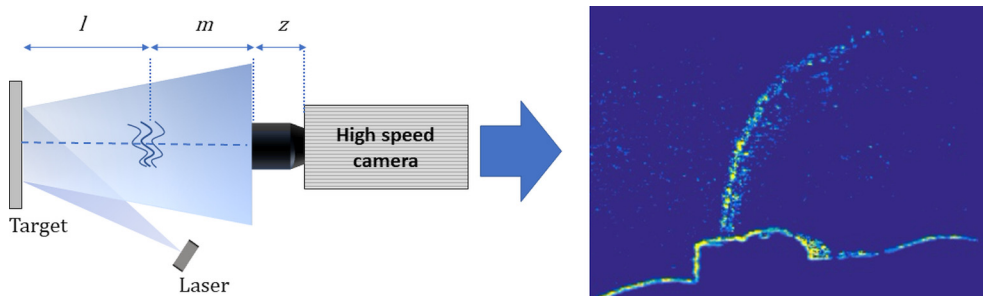


Figure 5.24. An illustration of the experimental setup is shown on the left, along with the resulting image of a convective plume of gas from a handheld lighter. The image was obtained by using an optical flow analysis based on the Horn-Schunck method [105].

Laser speckle BOS (ls-BOS) is an alternative technique that mitigates most of the limitations of conventional BOS and provides a very versatile setup to detect density variations. This method has been introduced by Meier et al. in [106] and we will follow the same naming convention of variables. In ls-BOS the pattern is created on a surface by illuminating the surface with a laser light source. The laser light source will create a pattern that is dominated by laser speckles due to the interference caused by the coherent light source. While this pattern can be used as a conventional BOS background pattern by focusing the camera on it directly, the difference is that the laser light will scatter off the surface and create a speckle

pattern that is emitted at a certain solid angle from the surface. The result is a somewhat collimated light pattern consisting of speckles, that originates from the background surface illuminated by the laser light. Speckle diameter D_s , is a function of the imaging system and the laser wavelength used, according to the relation:

$$D_s = \frac{4}{\pi} \cdot \frac{\lambda f}{D} \quad (5.4)$$

Based on this relation, the speckle size will only depend on the size of the aperture of our lens (D) and the laser used to create it. The result is that, unlike conventional BOS, the target can be placed anywhere in space and the speckle size will remain the same. Thus, maximum sensitivity is allowed without the requirement of a large distance of the background target. Effectively, the characterise target is virtual, and the lens imaging distance becomes the decisive factor. From theoretical calculations and verified results shown in [106], maximum sensitivity is reached already at a focusing distance of 2 meters with an $f=50\text{mm}$ lens set at $f/11$ aperture. In addition, the camera can be focused ahead of the density variation, in which case the sensitivity of the setup is increased even further. This presents a great opportunity to be used in an optical engine where the camera can be focused ahead of an evaporating spray jet or a flame. The laser speckle pattern can be generated by sending an expanded laser beam through one of the lateral windows, and the signal can be collected from the Bowditch mirror.

Once the images containing the speckle pattern, with and without the density gradient, the analysis is largely similar to PIV, FIV and other cross-correlation techniques. The displacement of the speckles is traced and measured. Some results from this technique are shown in Figure 5.25, where the gas from a lighter is visualised. There are two ways to analyse the displacement data; one is to compare each frame to the background target, and another is to compare every frame of the image sequence with its preceding, thus obtaining the displacements on a frame-to-frame basis. In addition, optical flow algorithms can be utilised to study the displacement, however, in that case it is difficult to quantify and understand the resulting signal. An example of such a technique is shown in Figure 5.24.

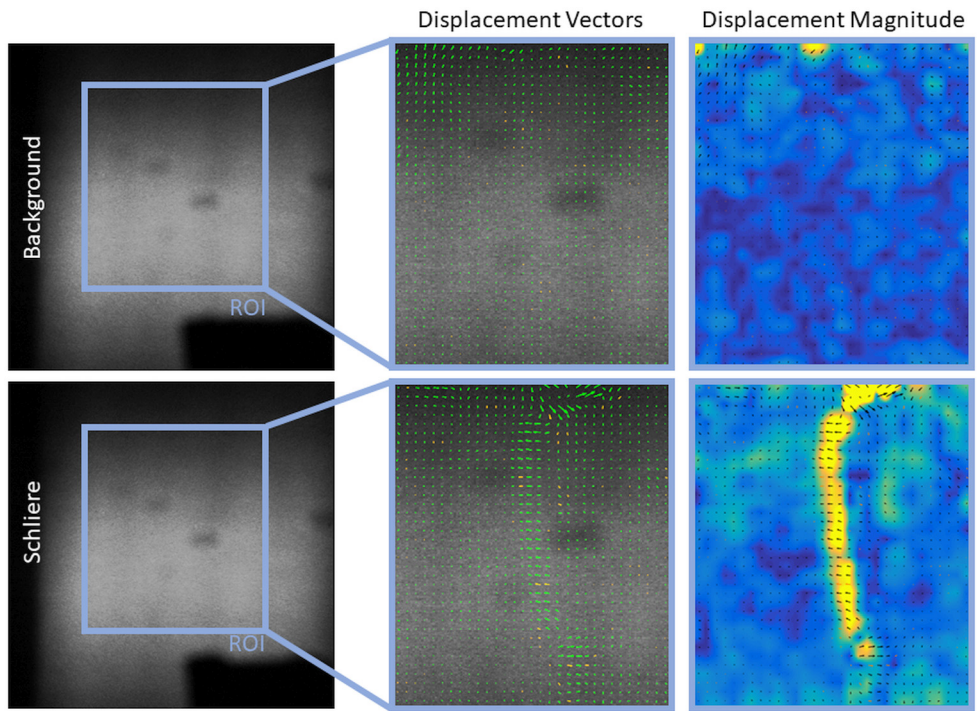


Figure 5.25. Results from the Laser Speckle-based BOS. On the top row, the background image is shown with some baseline vectors that manage to be detected even without the Schliere. On the bottom row, the Schliere is introduced and the resulting vector field, along with a map of the magnitude, is shown

6. Conclusions and Outlook

Many imaging applications within the field of optical and laser diagnostics are presented in this thesis, along with post-processing routines and tools for data analysis. This thesis provides an overview of some of the diagnostic techniques where imaging can be applied, the required experimental equipment and explains the post-processing required to extract accurate and useful information from the images. Some methods for presenting spatial variations of features are explained, along with other useful tools to communicate temporal variations in temporally resolved data.

A lot of work was focused on evaluating the combustion behaviour of methanol in compression-ignition engines. Both spray-driven and PPC combustion regimes were investigated, thus contributing to the limited knowledge and providing optical data of methanol's behaviour. For future activities in this field, I would highly recommend further investigation of the spray-driven combustion regime to even later injection timings, with low injection pressures to minimize parasitic losses of the engine. No benefit is observed in the combustion behaviour by increasing the injection pressure, but rather CFD simulations studies show that NO_x emissions increase. The chemiluminescence characteristics in this regime can also be further investigated optically, to better understand the emission characteristics of the translucent flames of methanol and the resulting line-of-sight signal. In addition, the spray behaviour and subsequent fuel distribution of methanol under various in-cylinder conditions were analysed. This data can be used to tune and calibrate vaporization models in CFD simulations.

In addition, the interaction between sprays and prevailing combustion in closely coupled pilot injections has been characterised with LIF of partially oxidised fuel in conjunction with high-speed imaging of the natural flame luminosity. An extinction mechanism was observed, and is thought to play an important role in the dips of the heat release rate and the subsequent perceived noise emitted from the engine. This study can be expanded to investigate this extinction effect for various dwell times between the injections and further analyse the effect in comparison to the heat release rate.

The study on exhaled particles managed to quantify the number of particles emitted during various everyday tasks and will shortly be complimented by an analysis of the velocities observed and the path followed by these particles. More advanced

techniques can also be applied to improve the detection capabilities and capture even smaller droplets.

Preliminary results are shown from an application of the Laser Speckle-based Background Oriented Schlieren technique. The technique is very promising as can observe density gradients in areas were traditionally it has not been possible to use conventional Schlieren techniques or the distance of the feature we need to analyse is very close to the background pattern resulting in poor sensitivity. More testing is required, and we would like to implement this technique in an optical engine to test its performance.

A brief description is given on modal decomposition techniques and a few applications that illustrate their usefulness in resolving spatial or temporal variations. The implementation of these techniques on image sets has been challenging due to the sheer size of the data, however, optimisation techniques already exist and should be studied further.

Acknowledgements

Where to start really...these years in the Division of Combustion Physics have been amazing and pivotal in making me the person that I am today. I guess I should begin with the person that trusted me and hired me. Mattias Richter, huge thank you for everything, you've been next to me and Giota for all these years, through good times and bad. You opened a portal for me into the field of combustion diagnostics, where I could use and develop my knowledge of physics and engines at the same time and helped me realise what I truly enjoy doing. Also, I never expected a supervisor that can help me bleed brakes while having a broken back. Cheers to what more there is to come! Marcus Alden, you're a huge inspiration for me, your character and attitude have been shaping the division for all these years and creating this fantastic "family-like" environment. Per-Erik Bengtsson, you have been a great successor of Marcus in the limited time you have had this responsibility, especially given the fact that we are amidst a global pandemic. Your efforts, friendliness and always approachable character are truly appreciated. Sven-Inge Möller, you were among the first people that I got close to, thanks in part to our quality-nicotine-time! Always a pleasure to chat with you about all things imaginable. Edouard Berrocal, what are you really, you must be an alien? Great researcher and amazing social skills usually don't go together! I truly appreciate the talks we've had, both on casual and research topics. Andreas Ehn, you're a true source of joy, I still remember your reaction when you found out that Alkis can be a Greek name. Elias Kristensson, thanks for always being open and welcoming to optics discussions. Frederik Ossler, always a pleasure chatting with you. Christian Brackmann, your willingness to discuss diagnostics is inspiring. Igor Buzuk, you are the true unsung hero of the division. Thanks for all your help and the little personal time I've managed to have with you, I really hope I can find more time in the future. Minna Ramkull, thanks for all your help and patience over the years, you rock. Cecilia Bille, thanks for always being helpful and glad to chat. I'd also like to thank all other seniors for the fun moments and the constructive talks and tips that you've shared with me.

Then I'd like to thank all the members in our group that I've had the chance to meet. Fahed Abou Nada, thanks for always being there and for all the discussions. Joakim Rosell, thanks for getting me going in the beginning, thanks for the welcoming and happy attitude. Zheming Li and Zhenkan Wang, thanks for all your help and the time we've spent together in labs and outside work. Christian Binder, special thanks to you, you've been great to live with...in the test cell...and a couple of hotel rooms!

Your energy levels are amazing and motivating, both in work and life in general. Saeed Derafshzan, thanks for being such a great friend and good listener. David Sanned, thanks for the quality research talks we've had. I'd also like to say thank you to the new generation of Richters, Henrik Feuk, Ruike Bi, Sebastian Nilsson and Kailun Zhang. You guys have all the knowledge, enthusiasm and patience to succeed, keep it up, cause it's gonna be a ride!

I'd also like to thank all the fellow PhD students in our division. I'll start with my officemate, Ali Hosseinnia, thanks for being there although you were sick half of the time, and the other half I was in the Matamis-building! When we did share the office, it was a sanctuary of free thinking and speech unlike anything else. Thanks for all the great times. Erdzan Hodzic, technically you're not from the division, but you were amazing to hang out with and I have to thank you for introducing me to turbulence and modal decomposition. Huge thank you for always helping me/us out and for being fun! Marco Lubrano Lavadera and Gianluca Capriolo, grazie per tutti, Arman Subash thanks for all the fun moments, Jim Larsson thanks for also being an amazing neighbour and sorry for keeping your Badminton racket for 2 years, Elin Malmqvist thanks for all the mature discussions. Manu Mannazhi (manari) you might be the nicest person I've ever met, Haisol Kim thanks for saving my @ss with Endnote for the symposium paper, Christopher Pichler, you saved my @ss with Matlab, Adrian Roth you're a programming guru, a tall one too! Maria Ruchkina and Yupan Bao, you're the guaranteed-laughter-duo. The rest of you are too many and as the last-minute person I am, I have to print this damn thesis!

I did also spend a lot of time in the building opposite the street where all the right (and wrong) noises are made. Of course, I'm talking about the Combustion Engines division in M-building, where everybody has also been very welcoming. Övind Andersson, Martin Tunér, Per Tunestål, Bengt Johansson, Sebastian Verhelst, thank you all for being there in so many ways, teaching, planning, and helping me. Michael Denny, it was an absolute legend to work with you, both in the lab and out. We did some great work that I am particularly proud of. Sara Lönn, we've been through a lot! Thanks for not giving up and pushing through the hardship. Special thanks to my methanol (and ethanol) buddies, Sam Shamun, Mateusz Pucilowski, Erik Svensson, for all the time we've spent productively and not so productively! Marcus Lundgren, Vikram Singh, Kenan Muric, Ted Lind, Pablo Garcia, Yann Gallo, thanks for the work or the time we spent together, it's been amazing. Nhut Lam, I put you in this section, but in reality you belong to the friends category. Thanks for being there for me and for all the time we've spent together. Cheers to more of the same in the near future. Nikolaos Dimitrakopoulos, the same applies for you, you were one of the first people I met in Sweden back in 2012 in Chalmers. I hope to have more time in the future to hang out.

Special thanks to Johan Hult and Eric Baudoin for all the work we did together and thanks for tolerating my ignorance at the time. Also huge thanks to Daniel Norrling, for nerding over physics and engineering topics with me and connecting personally.

A massive thank you to all my friends in Sweden! Karolina and Kenny, you've been with us from the very beginning, helping and supporting our lives and careers. Thanks for always making us smile and have a good laugh. Dina, you've gone above and beyond to help us and you've been an amazing friend. It's great to have you in our lives. The same applies for you, fellow Dr Fabian, thanks for all the great times we've had and for always being keen to meet up even at my last minute calls, so un-German of you! Big thank you to my Greek friends, in Greece and abroad. You've all partly contributed to this thesis happening and shaping me to who I am today.

The biggest thank you, however, is reserved for the people that have offered the greatest to this thesis, and that is my family. Dad, thanks for being who you are, for supporting me mentally and financially, and for pushing me the extra step. I couldn't be where I am today without you and your persistence (some say stubbornness!). Your father wasn't as lucky to have a dad like you. Mom, your patience, strength, resilience, and hard-working attitude are inspiring. Thanks for raising us how we are and for always doing everything you can for us. Panos and Giannis, thanks for all the help and support. Giota, it feels like yesterday that we first met and it's been more than 11 years. We live together and we work together, in the same group for God's sake, and yet I can't get enough of you. You've been massively supportive and patient with all my obsessions over cars and work. I cannot thank you enough for being the main person in my life. Though now, you share that spot with Dimitris! Dimitri, you are the happiest thing that has happened in my life. I've neglected you while writing this thesis, but I will pay it back. I will always try to be there for you and support you in whoever you choose to become in the future. Huge thank you to my mother-in-law, yiayia Chrysi, who is taking care of Dimitris and Giota while I'm not there. I am extremely grateful to all of you and I wish I can return your love.

References

- [1] H. E. B. Miller, Edward G., " *Spray penetration with a simple fuel injection nozzle*," NACA Technical Reports, vol. Report No.222, pp. 319-326, 1926 1926.
- [2] E. Svensson, C. Li, S. Shamun, B. Johansson, M. Tuner, C. Perlman, *et al.*, " *Potential Levels of Soot, NOx, HC and CO for Methanol Combustion*," 2016.
- [3] IEA. *Tracking Transport 2020, IEA, Paris* [Online]. Available: <https://www.iea.org/reports/tracking-transport-2020>
- [4] Z. Han, A. Uludogan, G. J. Hampson, and R. D. Reitz, " *Mechanism of Soot and NOx Emission Reduction Using Multiple-injection in a Diesel Engine*," 1996.
- [5] J. E. Dec, " *Advanced Compression-Ignition Combustion for High Efficiency and Ultra-Low NOX and Soot*," in *Encyclopedia of Automotive Engineering*, ed, pp. 1-40.
- [6] T. Li and H. Ogawa, " *Analysis of the Trade-off between Soot and Nitrogen Oxides in Diesel-Like Combustion by Chemical Kinetic Calculation*," ed: SAE International, 2011.
- [7] M. P. B. Musculus, " *On the Correlation between NOx Emissions and the Diesel Premixed Burn*," 2004.
- [8] Ö. Andersson, " *Diesel Combustion*," in *Handbook of Combustion*, ed, pp. 415-440.
- [9] IEA. *Carbon intensity of electricity generation in selected regions in the Sustainable Development Scenario, 2000-2040, IEA, Paris* [Online]. Available: <https://www.iea.org/data-and-statistics/charts/carbon-intensity-of-electricity-generation-in-selected-regions-in-the-sustainable-development-scenario-2000-2040>
- [10] L. D. Erik Emilsson, " *Lithium-Ion Vehicle Battery Production - Status 2019 on Energy Use, CO2 Emissions, Use of Metals, Products Environmental Footprint, and Recycling*," C444, 2019.
- [11] Q. Dai, J. C. Kelly, L. Gaines, and M. Wang, " *Life Cycle Analysis of Lithium-Ion Batteries for Automotive Applications*," Batteries, vol. 5, p. 48, 2019.
- [12] M. S. Masnadi, H. M. El-Houjeiri, D. Schunack, Y. Li, J. G. Englander, A. Badahdah, *et al.*, " *Global carbon intensity of crude oil production*," Science, vol. 361, p. 851, 2018.
- [13] S. A. Mattias Eriksson, " *LCAs of petrol and diesel*," Dept. of Energy and Technology, Sveriges lantbruksuniversitet 058, 2013.
- [14] E. Johnson, " *A carbon footprint of HVO biopropane*," Biofuels, Bioproducts and Biorefining, vol. 11, pp. 887-896, 2017.

- [15] S. Soam and P. Börjesson, "*Considerations on Potentials, Greenhouse Gas, and Energy Performance of Biofuels Based on Forest Residues for Heavy-Duty Road Transport in Sweden*," *Energies*, vol. 13, p. 6701, 2020.
- [16] S. Shamun, P. Garcia, and E. Svensson, "*Alternative Fuels for Particulate Control in CI Engines*," in *Engine Exhaust Particulates*, A. K. Agarwal, A. Dhar, N. Sharma, and P. C. Shukla, Eds., ed Singapore: Springer Singapore, 2019, pp. 181-197.
- [17] P. Napolitano, C. Guido, C. Beatrice, and L. Pellegrini, "*Impact of hydrocracked diesel fuel and Hydrotreated Vegetable Oil blends on the fuel consumption of automotive diesel engines*," *Fuel*, vol. 222, pp. 718-732, 2018/06/15/ 2018.
- [18] H. Pflaum, P. Hofmann, B. Geringer, and W. Weissel, "*Potential of Hydrogenated Vegetable Oil (HVO) in a Modern Diesel Engine*," 2010.
- [19] T. Hartikka, M. Kuronen, and U. Kiiski, "*Technical Performance of HVO (Hydrotreated Vegetable Oil) in Diesel Engines*," 2012.
- [20] P. C. Shukla, S. Shamun, L. Gren, V. Malmborg, J. Pagels, and M. Tuner, "*Investigation of Particle Number Emission Characteristics in a Heavy-Duty Compression Ignition Engine Fueled with Hydrotreated Vegetable Oil (HVO)*," *SAE International Journal of Fuels and Lubricants*, vol. 11, pp. 495-505, 2018.
- [21] H. Aatola, M. Larmi, T. Sarjoavaara, and S. Mikkonen, "*Hydrotreated Vegetable Oil (HVO) as a Renewable Diesel Fuel: Trade-off between NOx, Particulate Emission, and Fuel Consumption of a Heavy Duty Engine*," *SAE International Journal of Engines*, vol. 1, pp. 1251-1262, 2008.
- [22] Ö. Andersson and P. Börjesson, "*The greenhouse gas emissions of an electrified vehicle combined with renewable fuels: Life cycle assessment and policy implications*," *Applied Energy*, vol. 289, p. 116621, 2021/05/01/ 2021.
- [23] E. E. Agency. *Country level - Greenhouse gas emission intensity of electricity generation* [Online]. Available: <https://www.eea.europa.eu/data-and-maps/daviz/co2-emission-intensity-6>
- [24] G. A. Olah, "*Towards Oil Independence Through Renewable Methanol Chemistry*," *Angewandte Chemie International Edition*, vol. 52, pp. 104-107, 2013.
- [25] C. M. Charlie Hobson, "*Renewable Methanol Report*," Methanol Institute 2018.
- [26] J.-F. L. Robert Edwards, Jean-Christophe Beziat, "*Well-to-Wheels Analysis of Future Automotive Fuels and Power Trains in the European Context - Report, Version 3c*," European Commission, Joint Research Centre, Institute for Energy and Transport EUR 24952 EN - 2011, 2011.
- [27] G. Knothe, "*Historical perspectives on vegetable oil-based diesel fuels*," *INFORM - International News on Fats, Oils and Related Materials*, vol. 12, 11/01 2001.
- [28] D. A. G. Prof. Dr. George A. Olah, Prof. Dr. G. K. Surya Prakash, "*Production of Methanol: From Fossil Fuels and Bio-Sources to Chemical Carbon Dioxide Recycling*," in *Beyond Oil and Gas: The Methanol Economy*, ed, 2009, pp. 233-278.
- [29] N. S. Shamsul, S. K. Kamarudin, N. A. Rahman, and N. T. Kofli, "*An overview on the production of bio-methanol as potential renewable energy*," *Renewable and Sustainable Energy Reviews*, vol. 33, pp. 578-588, 2014/05/01/ 2014.

- [30] S. Verhelst, J. W. G. Turner, L. Sileghem, and J. Vancoillie, "*Methanol as a fuel for internal combustion engines*," *Progress in Energy and Combustion Science*, vol. 70, pp. 43-88, 2019/01/01/ 2019.
- [31] Q. I. Roode-Gutzmer, D. Kaiser, and M. Bertau, "*Renewable Methanol Synthesis*," *ChemBioEng Reviews*, vol. 6, pp. 209-236, 2019.
- [32] M. Martín and I. E. Grossmann, "*Towards zero CO₂ emissions in the production of methanol from switchgrass. CO₂ to methanol*," *Computers & Chemical Engineering*, vol. 105, pp. 308-316, 2017/10/04/ 2017.
- [33] L. Gustavsson, P. Börjesson, B. Johansson, and P. Svenningsson, "*Reducing CO₂ emissions by substituting biomass for fossil fuels*," *Energy*, vol. 20, pp. 1097-1113, 1995/01/01/ 1995.
- [34] N. Meunier, R. Chauvy, S. Mouhoubi, D. Thomas, and G. De Weireld, "*Alternative production of methanol from industrial CO₂*," *Renewable Energy*, vol. 146, pp. 1192-1203, 2020/02/01/ 2020.
- [35] A. M. Brownstein, "*Chapter 4 - Synthesis Gas-Based Fuels*," in *Renewable Motor Fuels*, A. M. Brownstein, Ed., ed Boston: Butterworth-Heinemann, 2015, pp. 33-46.
- [36] M. J. Bos, S. R. A. Kersten, and D. W. F. Brilman, "*Wind power to methanol: Renewable methanol production using electricity, electrolysis of water and CO₂ air capture*," *Applied Energy*, vol. 264, p. 114672, 2020/04/15/ 2020.
- [37] R. H. Julia Hansson, Maria Taljegård, Selma Brynolf, Maria Grahn, Karin Andersson, "*Electrofuels – a possibility for shipping in a low carbon future?*," IVL Swedish Environmental Research Institute C150, 2016.
- [38] V. Dieterich, A. Buttler, A. Hanel, H. Spliethoff, and S. Fendt, "*Power-to-liquid via synthesis of methanol, DME or Fischer–Tropsch-fuels: a review*," *Energy & Environmental Science*, vol. 13, pp. 3207-3252, 2020.
- [39] L. J. France, P. P. Edwards, V. L. Kuznetsov, and H. Almegren, "*Chapter 10 - The Indirect and Direct Conversion of CO₂ into Higher Carbon Fuels*," in *Carbon Dioxide Utilisation*, P. Styring, E. A. Quadrelli, and K. Armstrong, Eds., ed Amsterdam: Elsevier, 2015, pp. 161-182.
- [40] C. J. Mueller and M. P. Musculus, "*Glow Plug Assisted Ignition and Combustion of Methanol in an Optical DI Diesel Engine*," 2001.
- [41] A. Matamis, S. Lonn, L. Luise, B. M. Vaglieco, M. Tuner, O. Andersson, *et al.*, "*Optical characterization of methanol compression-ignition combustion in a heavy-duty engine*," *Proceedings of the Combustion Institute*, 2020/07/18/ 2020.
- [42] R. Barbella, A. Ciajolo, A. D'Anna, and C. Bertoli, "*Effect of fuel aromaticity on diesel emissions*," *Combustion and Flame*, vol. 77, pp. 267-277, 1989/09/01/ 1989.
- [43] H. H. Mi, W. J. Lee, C. B. Chen, H. H. Yang, and S. J. Wu, "*Effect of fuel aromatic content on PAH emission from a heavy-duty diesel engine*," *Chemosphere*, vol. 41, pp. 1783-90, Dec 2000.
- [44] A. Azetsu, Y. Sato, and Y. Wakisaka, "*Effects of Aromatic Components in Fuel on Flame Temperature and Soot Formation in Intermittent Spray Combustion*," 2003.
- [45] A. Violi, "*Modeling of soot particle inception in aromatic and aliphatic premixed flames*," *Combustion and Flame*, vol. 139, pp. 279-287, 2004/12/01/ 2004.

- [46] T. H. Päivi Aakko, Markku Niemi, Leena Rantanen- and Kolehmainen, "*PAH content of diesel fuel and automotive emissions*," VTT Technical Research Centre of Finland VTT-R-1155-06, 2006.
- [47] A. D'Anna, M. Alfè, B. Apicella, A. Tregrossi, and A. Ciajolo, "*Effect of Fuel/Air Ratio and Aromaticity on Sooting Behavior of Premixed Heptane Flames*," *Energy & Fuels*, vol. 21, pp. 2655-2662, 2007/09/01 2007.
- [48] G. Yanfeng, L. Shenghua, and L. Yu, "*Investigation on Methanol Spray Characteristics*," *Energy & Fuels*, vol. 21, pp. 2991-2997, 2007/09/01 2007.
- [49] W. Zeng, M. Xu, G. Zhang, Y. Zhang, and D. J. Cleary, "*Atomization and vaporization for flash-boiling multi-hole sprays with alcohol fuels*," *Fuel*, vol. 95, pp. 287-297, 2012/05/01/ 2012.
- [50] W. Zeng, M. Xu, M. Zhang, Y. Zhang, and D. J. Cleary, "*Macroscopic characteristics for direct-injection multi-hole sprays using dimensionless analysis*," *Experimental Thermal and Fluid Science*, vol. 40, pp. 81-92, 2012/07/01/ 2012.
- [51] W. Zeng, M. Xu, M. Zhang, Y. Zhang, and D. Cleary, "*Characterization of Methanol and Ethanol Sprays from Different DI Injectors by Using Mie-scattering and Laser Induced Fluorescence at Potential Engine Cold-start Conditions*," 2010.
- [52] A. K. Aigal, B. P. Pundir, and A. S. Khatchian, "*High Pressure injection and Atomization Characteristics of methanol*," 1986.
- [53] B. S. Higgins, C. J. Mueller, and D. L. Siebers, "*Measurements of Fuel Effects on Liquid-Phase Penetration in DI Sprays*," *SAE Transactions*, vol. 108, pp. 630-643, 1999.
- [54] D. L. Siebers and C. F. Edwards, "*Autoignition of Methanol and Ethanol Sprays under Diesel Engine Conditions*," 1987.
- [55] M. Richter, A. Franke, M. Aldén, A. Hultqvist, and B. Johansson, "*Optical Diagnostics Applied to a Naturally Aspirated Homogeneous Charge Compression Ignition Engine*," 1999.
- [56] G. R. Johnson, L. Morawska, Z. D. Ristovski, M. Hargreaves, K. Mengersen, C. Y. H. Chao, *et al.*, "*Modality of human expired aerosol size distributions*," *Journal of Aerosol Science*, vol. 42, pp. 839-851, 2011/12/01/ 2011.
- [57] R. G. Loudon and R. M. Roberts, "*Singing and the Dissemination of Tuberculosis*," *American Review of Respiratory Disease*, vol. 98, pp. 297-300, 1968/08/01 1968.
- [58] G. S. Settles, "*Basic Concepts*," in *Schlieren and Shadowgraph Techniques: Visualizing Phenomena in Transparent Media*, G. S. Settles, Ed., ed Berlin, Heidelberg: Springer Berlin Heidelberg, 2001, pp. 25-38.
- [59] M. Hill and E. Haering, *Flow visualization of aircraft in flight by means of Background Oriented Schlieren using Celestial Objects*, 2017.
- [60] P. K. Panigrahi and K. Muralidhar, "*Laser Schlieren and Shadowgraph*," in *Schlieren and Shadowgraph Methods in Heat and Mass Transfer*, P. K. Panigrahi and K. Muralidhar, Eds., ed New York, NY: Springer New York, 2012, pp. 23-46.
- [61] G. Meier, "*Computerized background-oriented schlieren*," *Experiments in Fluids*, vol. 33, pp. 181-187, 2002/07/01 2002.

- [62] M. Raffel, "*Background-oriented schlieren (BOS) techniques*," Experiments in Fluids, vol. 56, p. 60, 2015/03/06 2015.
- [63] G. S. Settles and M. J. Hargather, "*A review of recent developments in schlieren and shadowgraph techniques*," Measurement Science and Technology, vol. 28, p. 042001, 2017/02/15 2017.
- [64] T. York, "*Fundamentals of Image Sensor Performance*," 2011.
- [65] P. C. Miles, *The history and evolution of optically accessible research engines and their impact on our understanding of engine combustion*; Sandia National Lab. (SNL-CA), Livermore, CA (United States), 2015.
- [66] F. W. Bowditch, "*A New Tool for Combustion Research A Quartz Piston Engine*," 1961.
- [67] M. S. Chris Harris, "*A combined corner and edge detector*," In Proc. of Fourth Alvey Vision Conference, pp. p.147-151, 1988.
- [68] A. Chatterjee, "*An introduction to the proper orthogonal decomposition*," Current Science, vol. 78, pp. 808-817, 2000.
- [69] J. Weiss, "*A Tutorial on the Proper Orthogonal Decomposition*," in *AIAA Aviation 2019 Forum*, ed.
- [70] K. Taira, S. L. Brunton, S. T. M. Dawson, C. W. Rowley, T. Colonius, B. J. McKeon, et al., "*Modal Analysis of Fluid Flows: An Overview*," AIAA Journal, vol. 55, pp. 4013-4041, 2017.
- [71] S. Leask and V. McDonnell, *On the Physical Interpretation of Proper Orthogonal Decomposition and Dynamic Mode Decomposition for Liquid Injection*, 2019.
- [72] H. Dembinski and H.-E. Ångström, "*Optical Study of Swirl during Combustion in a CI Engine with Different Injection Pressures and Swirl Ratios Compared with Calculations*," SAE Technical Papers, 04/16 2012.
- [73] H. Dembinski, H.-E. Ångström, and H. Razzaq, "*In-Cylinder Flow Pattern Evaluated with Combustion Image Velocimetry, CIV, and CFD Calculations during Combustion and Post-Oxidation in a HD Diesel Engine*," SAE Technical Papers, vol. 6, 09/08 2013.
- [74] L. Rao and S. Kook, "*Optimisation of Image Processing Parameters for Flame Image Velocimetry (FIV) Measurement in a Single-Cylinder, Small-Bore Optical Diesel Engine*," 2019.
- [75] J. N. Kutz, X. Fu, and S. L. Brunton, "*Multiresolution Dynamic Mode Decomposition*," SIAM Journal on Applied Dynamical Systems, vol. 15, pp. 713-735, 2016/01/01 2016.
- [76] P. J. Schmid, "*Dynamic mode decomposition of numerical and experimental data*," Journal of Fluid Mechanics, vol. 656, pp. 5-28, 2010.
- [77] P. J. Schmid, L. Li, M. P. Juniper, and O. Pust, "*Applications of the dynamic mode decomposition*," Theoretical and Computational Fluid Dynamics, vol. 25, pp. 249-259, 2011/06/01 2011.
- [78] S. Asadi, A. S. Wexler, C. D. Cappa, S. Barraza, N. M. Bouvier, and W. D. Ristenpart, "*Aerosol emission and superemission during human speech increase with voice loudness*," Scientific Reports, vol. 9, p. 2348, 2019/02/20 2019.

- [79] C. Schulz and V. Sick, "*Tracer-LIF diagnostics: quantitative measurement of fuel concentration, temperature and fuel/air ratio in practical combustion systems,*" Progress in Energy and Combustion Science, vol. 31, pp. 75-121, 2005/01/01/ 2005.
- [80] Z. Wang, S. Lonn, A. Matamis, O. Andersson, M. Tuner, M. Alden, *et al.*, "*Transition from HCCI to PPC: Investigation of Fuel Distribution by Planar Laser Induced Fluorescence (PLIF),*" SAE International Journal of Engines, vol. 10, pp. 1465-1481, 2017.
- [81] Z. Wang, P. Stamatoglou, M. Lundgren, L. Luise, B. M. Vaglieco, A. Andersson, *et al.*, "*Simultaneous 36 kHz PLIF/chemiluminescence imaging of fuel, CH₂O and combustion in a PPC engine,*" Proceedings of the Combustion Institute, vol. 37, pp. 4751-4758, 2019/01/01/ 2019.
- [82] J. D. Naber and D. L. Siebers, "*Effects of Gas Density and Vaporization on Penetration and Dispersion of Diesel Sprays,*" 1996.
- [83] M. Pucilowski, M. Jangi, S. Shamun, M. Tuner, and X.-S. Bai, "*The Effect of Injection Pressure on the NO_x Emission Rates in a Heavy-Duty DIC_I Engine Running on Methanol,*" 2017.
- [84] S. Shamun, M. Shen, B. Johansson, M. Tuner, J. Pagels, A. Gudmundsson, *et al.*, "*Exhaust PM Emissions Analysis of Alcohol Fueled Heavy-Duty Engine Utilizing PPC,*" ed: SAE International, 2016.
- [85] M. Pucilowski, M. Jangi, S. Shamun, C. Li, M. Tuner, and X.-S. Bai, "*Effect of Start of Injection on the Combustion Characteristics in a Heavy-Duty DIC_I Engine Running on Methanol,*" 2017.
- [86] M. Denny, A. Matamis, H. Persson, M. Richter, and Ö. Andersson, "*Interaction between Fuel Jets and Prevailing Combustion During Closely-Coupled Injections in an Optical LD Diesel Engine,*" vol. 1, 2019.
- [87] M. Denny, A. Matamis, Z. Wang, H. Persson, P. Tunestal, M. Richter, *et al.*, "*Optical Investigation on the Combustion Process Differences between Double-Pilot and Closely-Coupled Triple-Pilot Injection Strategies in a LD Diesel Engine,*" vol. 1, 2019.
- [88] M. Denny, F. Holst, A. Helmantel, H. Persson, P. Tunestål, and Ö. Andersson, "*Impact of closely-coupled triple-pilot and conventional double-pilot injection strategies in a LD diesel engine,*" Fuel, vol. 246, pp. 141-148, 2019/06/15/ 2019.
- [89] M. Denny, L. van den Ende, H. Persson, and Ö. Andersson, "*Manipulating heat release features to minimize combustion noise,*" Fuel, vol. 263, p. 116613, 2020/03/01/ 2020.
- [90] A. Hultqvist, M. Christensen, B. Johansson, M. Richter, J. Nygren, J. Hult, *et al.*, "*The HCCI Combustion Process in a Single Cycle - Speed Fuel Tracer LIF and Chemiluminescence Imaging,*" 2002.
- [91] R. Schießl, A. Dreizler, U. Maas, A. J. Grant, and P. Ewart, "*Double-Pulse PLIF Imaging of Self-Ignition Centers in an SI Engine,*" 2001.
- [92] A. Hultqvist, M. Christensen, B. Johansson, A. Franke, M. Richter, and M. Aldén, "*A Study of the Homogeneous Charge Compression Ignition Combustion Process by Chemiluminescence Imaging,*" SAE Transactions, vol. 108, pp. 2114-2127, 1999.

- [93] Z. Zheng, X. Fang, H. Liu, C. Geng, Z. Yang, L. Feng, *et al.*, "Study on the flame development patterns and flame speeds from homogeneous charge to stratified charge by fueling n-heptane in an optical engine," *Combustion and Flame*, vol. 199, pp. 213-229, 2019/01/01/ 2019.
- [94] R. D. Matthews, "Fundamental Combustion Modes," in *Encyclopedia of Automotive Engineering*, ed, pp. 1-19.
- [95] C. Brackmann, J. Nygren, X. Bai, Z. Li, H. Bladh, B. Axelsson, *et al.*, "Laser-induced fluorescence of formaldehyde in combustion using third harmonic Nd:YAG laser excitation," *Spectrochimica Acta Part A: Molecular and Biomolecular Spectroscopy*, vol. 59, pp. 3347-3356, 2003/12/01/ 2003.
- [96] J. Olofsson, H. Seyfried, M. Richter, M. Aldén, A. Vressner, A. Hultqvist, *et al.*, "High-Speed LIF Imaging for Cycle-Resolved Formaldehyde Visualization in HCCI Combustion," 2005.
- [97] M. Richter, R. Collin, J. Nygren, Ald, Eacute, M. N, *et al.*, "Studies of the Combustion Process with Simultaneous Formaldehyde and OH PLIF in a Direct-Injected HCCI Engine," *JSME International Journal Series B Fluids and Thermal Engineering*, vol. 48, pp. 701-707, 2005.
- [98] P. C. Miles, R. Collin, L. Hildingsson, A. Hultqvist, and Ö. Andersson, "Combined measurements of flow structure, partially oxidized fuel, and soot in a high-speed, direct-injection diesel engine," *Proceedings of the Combustion Institute*, vol. 31, pp. 2963-2970, 2007/01/01/ 2007.
- [99] J. V. Pastor, J. J. López, J. Enrique Juliá, and J. V. Benajes, "Planar Laser-Induced Fluorescence fuel concentration measurements in isothermal Diesel sprays," *Optics Express*, vol. 10, pp. 309-323, 2002/04/08 2002.
- [100] R. Collin, J. Nygren, M. Richter, M. Aldén, L. Hildingsson, and B. Johansson, "Simultaneous OH- and Formaldehyde-LIF Measurements in an HCCI Engine," 2003.
- [101] L. Hildingsson, B. Johansson, A. Hultqvist, G. Särner, M. Richter, and M. Aldén, "Simultaneous Formaldehyde and Fuel-Tracer LIF Imaging in a High-Speed Diesel Engine With Optically Accessible Realistic Combustion Chamber," 2005.
- [102] P. C. Miles, L. Hildingsson, and A. Hultqvist, "The influence of fuel injection and heat release on bulk flow structures in a direct-injection, swirl-supported diesel engine," *Experiments in Fluids*, vol. 43, pp. 273-283, 2007/08/01 2007.
- [103] M. P. B. Musculus, P. C. Miles, and L. M. Pickett, "Conceptual models for partially premixed low-temperature diesel combustion," *Progress in Energy and Combustion Science*, vol. 39, pp. 246-283, 2013/04/01/ 2013.
- [104] C. A. Idicheria and L. M. Pickett, "Formaldehyde Visualization Near Lift-off Location in a Diesel Jet," 2006.
- [105] B. Horn and B. Schunck, "Determining Optical Flow," *Artificial Intelligence*, vol. 17, pp. 185-203, 08/01 1981.
- [106] A. H. Meier and T. Roesgen, "Improved background oriented schlieren imaging using laser speckle illumination," *Experiments in Fluids*, vol. 54, p. 1549, 2013/06/02 2013.

Summary of papers

Paper I.

Exhaled respiratory particles during singing and talking.

This article came in response to the global outbreak of the Coronavirus SARS-CoV-2. Among the first activities to get suspended during the outbreak of the virus was choir singing in many countries around the world, due to reports of increased transmission risk as this virus relies on the respiratory system and exhaled droplets for transmission. However, previous studies had focused on talking, sneezing and coughing, thus no scientific evidence existed on whether signing increased the number of droplets exhaled and which factors affect such droplet emission. In order to study the effect, twelve singers participated in the experiments with various degrees of singing experience and were asked to sing a simple verse in two tones and at different loudness levels as well as with exaggerated diction which is common practice in live performances. As benchmark cases, talking and talking loudly were also included in the experiment to see if the effect is due to forced air flow alone. The analysis was performed with two different techniques, one based on an aerodynamic particle sizer and one based on direct high-speed imaging of the exhaled particles. Results showed that the number of exhaled droplets increased with loudness, tonality and diction. The optical method, being a more direct and time-resolved method, showed that predominantly consonants produce droplets as no droplets were detected in vowel voicing. This was hypothesised to be due to the particle sizes being smaller as they are generated from pulsations of the vocal cords and the contribution of the mouth is minimal. The particle sizer method provided the particle number count and size by averaging 10 second intervals of a sample flow collected through a funnel, thus accurate size and count data was obtained, without being temporally resolved however. The two techniques provided different data that complimented each other and provided a complete look at what exhaled droplet emission can be expected while talking and singing.

I was responsible for the optical part of the experiment, the data processing of the optical results, presentation of the results and the derived conclusions. I also contributed to writing the paper and provided feedback for the full article. Jakob Löndahl and Malin Alsved wrote the majority of the article and other co-authors provided feedback either during the experiments or in the writing of the article.

Paper II.

Optical characterization of methanol compression-ignition combustion in a heavy-duty engine.

In this activity, the goal was to optically study how methanol combusts in compression ignition engines. Very little data existed previously on methanol autoignition combustion and the results showed that the process is very different compared to other fuels. Originally, the goal was to compare the fuel mixing process in comparison to other fuels and show where ignition was most likely to occur. An initially wide range of injection timings was narrowed to approximately 20° CA as it became apparent that methanol mixes rapidly, and no significant benefit comes from injecting earlier. CFD simulations had indicated that methanol ignites on lean mixtures due to the quick mixing and the cooling of the phase change of methanol from liquid to gaseous. A shallow combustion chamber allowed for a single laser sheet to properly probe the fuel distribution before the onset of combustion and a sensitivity analysis included in the article showed that it can represent quite well the fuel distribution within the whole volume. Natural luminosity of the flame was recorded with a high-speed camera and the effect of cyclic variations on the image sequences was addressed in order to correctly investigate the ignition process. Additionally, elastic scattering of laser light was used to visualise the liquid fuel droplets and study the interaction with combustion. The high heat of vaporization of methanol is hypothesised to extinguish ignition kernels as they are seen to develop only when the spray tip retracts due to fluctuations or when the injection process ends.

I was responsible for the optical setup and design of experiment with guidance from the co-authors and senior researchers from the Division of Combustion Engines at Lund University. Sara Lönn was responsible for the operation of the optical engine. I performed all data processing, data presentation and wrote the article with feedback from Mattias Richter.

Paper III.

Optical Characterization of Methanol Sprays and Mixture Formation in a Compression-Ignition Heavy-Duty Engine.

Similar to **Paper II**, few studies exist on direct-injected methanol sprays. The focus in this study was to investigate how common engine operating parameters affect the fuel distribution and the spray process. The same optical engine was used and a few start-of-injection (SOI) timing were tested that were decided in conjunction with the department of Fluid Dynamics of Lund University in order to be used for model validation. Three different injection pressures were tested as well as two intake pressures and finally, a comparison is shown with another fuel typically used for PPC combustion. The dependence on SOI and thus the pressure and temperature dependence was documented, providing valuable data to our colleagues for CFD

simulations. The effect of injection pressure was shown to be minimal in terms of liquid penetration length, the fuel distribution however was significantly different with the higher injection pressures showing a more homogeneous mixture. This more homogeneous mixture has been shown to be responsible for higher NOX emissions in CFD simulations, thus the article concluded that there are no benefits in using high injection pressures as that only increases emissions and engine parasitic losses. Comparing methanol to PRF81 showed that they behave quite differently as methanol appears more sensitive to temperature, since liquid length varied significantly with SOI variations. On the contrary, while PRF81 was not affected greatly by SOI, its liquid length varied greatly when intake pressure was increased. Meanwhile, methanol's liquid length was unaffected by intake pressure, thus revealing the higher dependence on temperature.

I was responsible for the optical setup and design of experiment with guidance from the co-authors and senior researchers from the Division of Combustion Engines at Lund University. Sara Lönn was responsible for the operation of the optical engine. I performed all data processing, data presentation and wrote the article with feedback from Mattias Richter.

Paper IV.

Optical Investigation on the Combustion Process Differences between Double-Pilot and Closely-Coupled Triple-Pilot Injection Strategies in a LD Diesel Engine.

Here, the interaction between individual injections of a split injection strategy are investigated via natural flame luminosity in a light-duty optical engine. Three injection strategies are tested typical of what is found in a commercial light duty diesel engine. A high-speed camera is used to temporally resolve the effects taking place and two light sensitivity settings are used; one highly sensitive to detect weak chemiluminescence from early pilot injections and one less sensitive to capture high intensity soot luminosity from subsequent injections. The weak chemiluminescence signal is then analysed to determine the flame speed of these regions and classify the combustion process as chemically-controlled autoignition or flame propagation from an ignition site. Some combustion extinction is observed between intermediate injections and the effect is demonstrated and studied across the three strategies. This extinction is hypothesised to be responsible for dips in the heat release which lead to increased noise produced from the engine. Features on the sooty flames are additionally used to visualise in detail the flow field around a transient spray jet.

I and Zhenkan Wang were responsible for the optical part of the experiment, Michael Denny was responsible for the operation of the engine and the design of experiment. I performed the data analysis, presentation of the optical data and contributed to writing parts of the article with feedback from Mattias Richter.

Paper V.

Interaction between Fuel Jets and Prevailing Combustion During Closely-Coupled Injections in an Optical LD Diesel Engine.

Following the findings in **Paper IV**, the same injection strategies were studied with the addition of a 355 nm 10Hz laser system in order to visualise partially oxidised fuel (POF) that would indicate flame extinction and heating of the freshly introduced fuel mixture. The laser beam is formed to a small sheet that is guided inside the engine along the spray axis of one of the spray jets, thus providing a cross-section of the spray plume and the spray-driven combustion. The high-speed camera was used to record flame luminosity and the images from both cameras are overlaid to see if the extinction captured previously on the flame luminosity images coincides with the appearance of POF. In most cases it was obvious that POF signal increased, however in longer injection durations the cooling effect of the freshly injected fuel leads to little fuel oxidation close to the tip of the injector and the POF signal is pushed downstream making the evaluation more difficult.

I was responsible for the optical part of the experiment; Michael Denny was responsible for operating the engine and the design of experiment. I performed the data analysis, presentation of the optical data and contributed to writing parts of the article with feedback from Mattias Richter.

Paper VI.

Transition from HCCI to PPC: Investigation of Fuel Distribution by Planar Laser Induced Fluorescence (PLIF).

In this study, a wide range of SOI points are tested that result in different types of combustion. The motivation was to explain the shape of combustion sensitivity to intake temperature for low octane fuels. The goal was to investigate the mixture formation and where fuel is delivered in order to see if there is a coupling to ignition sensitivity. Fuel tracer Laser Induced Fluorescence (LIF) was used to visualise the fuel distribution. The laser sheet was guided in the engine as a vertical sheet providing a side-view cross-section of the combustion chamber. The findings from such studies depends heavily on the geometry of the combustion chamber so a simplified version of a piston typical of a heavy-duty engine was used. The results showed that the cases with the lowest required intake temperature were the ones with the majority of the fuel at the centre of the piston bowl. Later injections lead to high concentration of fuel on the bowl wall due to limited mixing time before the onset of combustion, while with earlier injections fuel will inevitably escape the bowl and be delivered in crevice volumes of the combustion chamber.

I and Zhenkan Wang were responsible for the optical setup and Sara Lönn was responsible for the operation of the engine. I assisted Zhenkan in discussing the results and writing the article, with feedback from Mattias Richter.